Rijksuniversiteit Groningen

Polarized Angle Resolved Infrared Spectroscopy of high Temperature Superconductors.

Proefschrift

ter verkrijging van het doctoraat in de
Wiskunde en Natuurwetenschappen
aan de Rijksuniversiteit Groningen
op gezag van de
Rector Magnificus, dr. F. van der Woude,
in het openbaar te verdedigen op
maandag 6 april 1998
des namiddags te 4,15 uur

door

Dr. Herpertap S. Somal

Geboren op 5 augustus 1951
Te Sultanpure, India

Contents

1

Introduction

1.1 Basic Properties of the Insulating Parent Compound

In 1986 superconductivity above 30K was discovered in the material lanthanum barium copper oxide by Bednorz and Müller [1]. Since then the condensed matter physics community has indulged in an unprecedented worldwide effort in materials processing, characterization of physical properties, and theoretical modelling of this new class of superconductors. These materials are commonly referred to as the 'cuprates'. All cuprates have one or more copper oxygen planes (CuO_2) per unit cell, separated by insulating layers which have the rocksalt structure. In Fig. 1.1 we display the crystal structure of the high temperature phase of $La_{2-x}Sr_xCuO_4$ in the body-centred tetragonal structure, which contains a single CuO_2 layer per unit cell. Within the CuO_2 layers Cu^{2+} ions are arranged in a square array, and are bridged by O^{2-} ions. This arrangement is found in all high T_c cuprates, and has important implications for the electronic structure, which we will now briefly discuss.

From the very beginning it has been clear that the Cu^{2+} ions in these materials have an incomplete 3d-shell with a d^9 configuration [2, 3]. With this configuration the Cu-ions behave effectively as transition metal atoms. The free Cu^{2+} has the $^2D_{3/2}$ ground state. As one can see in Fig. 1.1, the Cu-ions have a 6-fold coordination to the surrounding oxygen ions. As a crude approximation to the actual C_4 site symmetry we first consider the levels in octahedral site symmetry. The crystal field lifts the 5-fold degeneracy of the 3d level, and splits it in the

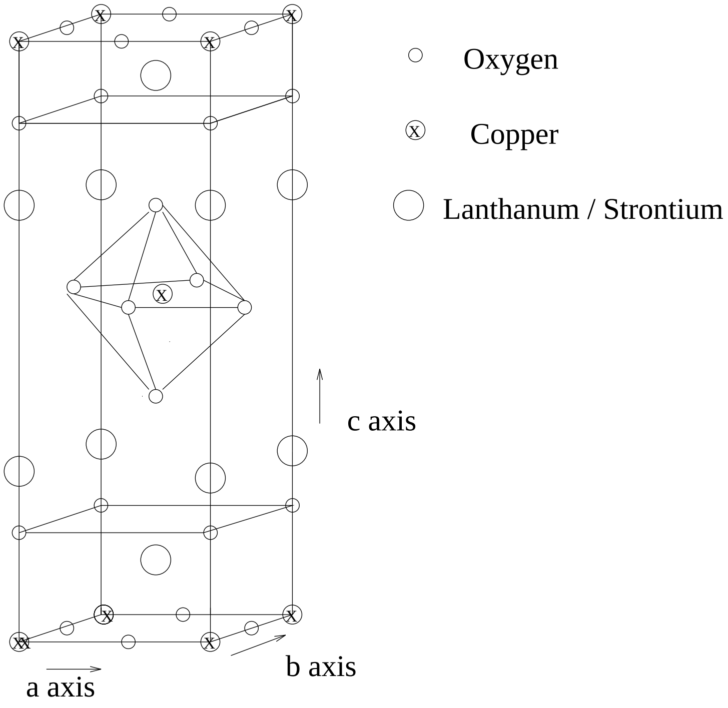

Figure 1.1: *Lattice structure of $La_{2-x}Sr_xCuO_4$.*

3-fold degenerate t_{2g} manifold (d_{xy},d_{xz},d_{yz}) and the 2-fold degenerate e_g manifold ($d_{z^2-x^2}$,$d_{x^2-y^2}$). Due to the fact that the lobes of the e_g orbitals point towards the negatively charged O^{2-} ions, these have the highest energy in this compound. The actual site symmetry corresponds to the C_4 group, which lifts the degeneracy within the e_g manifold, and splits the t_{2g} manifold into e_g (d_{xz},d_{yz}) and a separate d_{xy} state. As a result $d_{x^2-y^2}$ becomes the highest d-level. The Cu^{2+} ions have a d^9 configuration, where the only hole is located in the $d_{x^2-y^2}$ orbital.

Ignoring for the moment the effects of the strong on-site electron-electron interactions on the Cu-ions, the bandstructure of the CuO_2 planes becomes a particularly simple one: The only relevant tight binding orbitals close to the Fermi energy are the two oxygen $2p_x$ and $2p_y$ orbitals oriented along the Cu-O-Cu bond directions, and the Cu $3d_{x^2-y^2}$ orbital [4]. The valence band is then (besides a non-bonding and a bonding band more than half an eV below the Fermi energy) a band of antibonding 3d-2p character with an energy-momentum dispersion relation:

$$\epsilon_k = -2t\left(\cos(k_x a) + \cos(k_y a)\right) - 4t'\cos(k_x a)\cdot\cos(k_y a). \tag{1.1}$$

Where t is the nearest neighbour hopping energy and t' is the next nearest neighbour hopping energy. With nominally one hole per CuO_2 in pure La_2CuO_4 the latter band is precisely half filled, and the material should be a metal. This is in contrast to the experimental fact that La_2CuO_4 is an insulator at all temperatures and has an anti-ferromagnetic structure.

This brings us to the strong electron-electron correlation energy in the Cu 3d shell. Let us consider the reaction

$$2Cu^{2+} \rightarrow Cu^{+} + Cu^{3+} \tag{1.2}$$

and let us restrict this discussion to the $3d_{x^2-y^2}$ state for the sake of clarity. Without electron-electron interactions no energy is needed to make this transition, because it does not involve a change of the total number of electrons in the $3d_{x^2-y^2}$ states. If this level is half-filled, i.e. if it contains only one electron per ion, this implies that it is located at the Fermi-level.

Let us now consider the effect of electron-electron interactions: on the right hand side of the above reaction two electrons occupy the same atom. We define the potential energy of the two electrons in the vicinity of each other as U, which is of the order e^2/r_d, where r_d is the radius of the 3d level. This raises the energy of the two electron-state by an amount U. For the free Cu^{2+} ion $U = 26$eV, which is reduced to about 7 eV in the cuprates due to screening [5]. As the above reaction corresponds to making an electron-hole excitation with the electron and hole separated far from each other, this proves that the $3d_{x^2-y^2}$ level pinned to E_F is now split into a pair of states: One occupied (hole excitation), one empty (electron excitation) and separated by a gap of $U = 7$ eV. This gap is known as the Mott-Hubbard gap. The occurrence thereof explains why for instance La_2CuO_4 is an insulator. Within the picture of non-interacting electrons, a fully occupied state would accommodate two electrons of opposite spin per site. In contrast, within the Hubbard model the upper and lower band correspond to *singlet* states. The states below (above) the Fermi level correspond to a single hole (electron) excitation.

In the cuprates the empty level is located about 2 eV above the Fermi level [3], which implies that the occupied $3d$ states are located 5 eV below E_F. Interestingly the Mott-Hubbard splitting turns out to be smaller than the 7 eV expected between the highest occupied and unoccupied Cu 3d level. The gap observed in the optical spectra is therefore not the Hubbard gap of 7 eV, but the much smaller charge transfer gap of only 2.2 eV [6, 7]. This means that the highest occupied level is an O 2p state which is at a higher energy than the occupied Cu 3d level, as shown in Fig. 1.2 This generic property of the transition metal oxides at the right hand side of the 3d series was first pointed out by Zaanen, Sawatzky and Allen [8]. The fact that the simplest tight binding model of the insulating state of the CuO_2 planes gives rise to a correlation gap where the lowest unoccupied states have Cu 3d character while the highest occupied states have O 2p character, highlights an aspect of the electronic structure which at first glance is of perplexing complexity. However, it turns out to be of crucial importance to take into account the hybridization between the O 2p states and the Cu 3d states. The highest occupied hybrid state is of predominantly O 2p character. Interestingly it shares in common with the upper Hubbard band the fact that it is a singlet state which can be occupied by only one electron per site [9, 10]. Another property shared with the upper Hubbard band is it's symmetry which transforms as $x^2 - y^2$ centred at Cu. Taken together the occupied Zhang-Rice singlet band and the upper Hubbard band mimic the symmetries and spectral properties of a single Hubbard-split band of $3d_{x^2-y^2}$ character. In detail many properties are different. For example the resulting exchange interactions between spins on nearest neighbour and next nearest neighbour Cu sites are different [11]. Nevertheless the similarities have motivated many theoreticians to consider the simpler Hubbard U model instead of the richer 3-band extended Hubbard model as a starting point for the investigation of the problem of high T$_c$ superconductivity.

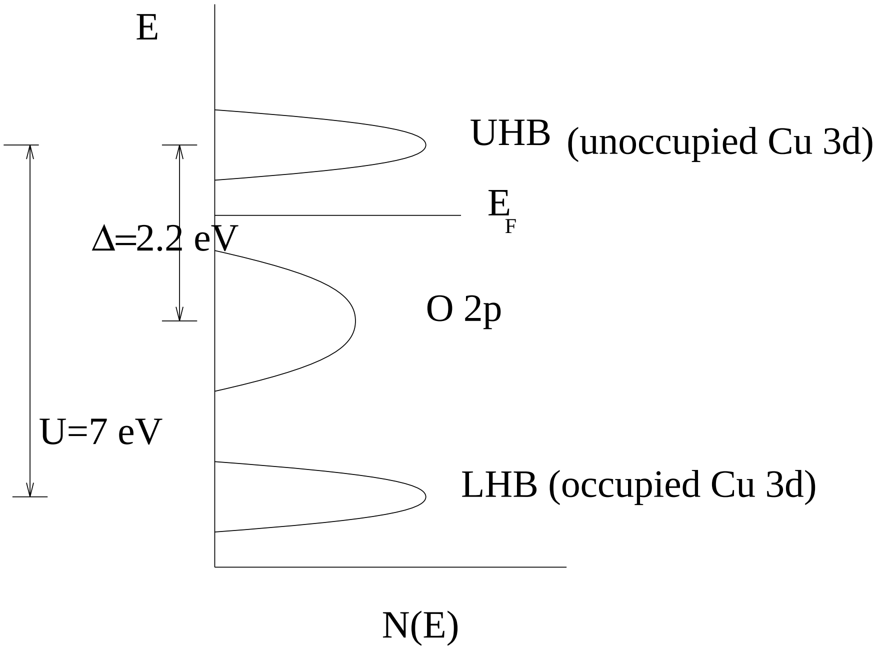

Figure 1.2: *An energy E versus density of states (DOS) N(E) sketch showing the charge transfer energy Δ and the Mott-Hubbard gap U*

1.2 Properties as a Function of Doping

The whole family of HTSCs is both large and varied, but principally centred on the thallium, yttrium, bismuth, mercury and lanthanum compounds. It is not feasible in this short introduction to comment upon the anomalies of each compound. A large part of this thesis involves the investigation of $La_{2-x}Sr_xCuO_4$, therefore this cuprate will be taken as an example. Figure 1.3 shows the phase diagram for this material [12, 13]. It is quite complex and shows a high sensitivity to small changes in Sr substitution. The anti-ferromagnetic state exists only for very small values of x, after which long range order disappears and only short range order remains, as shown by neutron scattering measurements.

The main effect of substituting divalent Sr for trivalent La, is to introduce one hole per Sr^{2+} ion in the CuO_2 layers. Beyond a doping level of about 5 percent Sr the material becomes a conductor which is superconducting at low temperatures. The highest T_c is reached for a Sr concentration of 15 percent (usually called 'optimal' doping concentration). In other cuprate materials hole-doping is realized by incorporating interstitial O^{2-} ions in the rocksalt layers.

Also indicated in this phase diagram is a transition of the crystal structure from the tetragonal phase at high temperatures to an orthorhombic phase at low temperatures. The corresponding change of the atomic positions is small. In the orthorhombic phase the octahedra distort, which results in the buckling of the CuO_2 plane and a tilting of the apical oxygen axis. This distortion of the CuO_2 octahedra may be increased by substituting neodymium for lanthanum which results in a suppression of T_c [14]. However Nd has a net spin and it is possible that the reduction in T_c is linked to the change in magnetic coupling. It has often been speculated that the small changes in the crystal structure are responsible for the suppression of superconductivity at higher Sr concentrations. On the other hand in all high T_c cuprates, T_c starts to decrease when the doping exceeds 0.15 holes per CuO_2 formula unit, while many of these compounds ($Tl_2Ba_2CuO_6$ and) appear to be purely tetragonal compounds. Hence the correlation between crystal structure and the suppression of superconductivity in $La_{2-x}Sr_xCuO_4$ may not be relevant.

The pairing symmetry of the high T_c superconductors has been subject of intensive investigations. Based upon angle resolved photoelectron spectroscopy(ARPES) of $Bi_2Sr_2CaCu_2O_8$, a consensus has now been reached about the strong anisotropy of the gap with minima, possibly nodes, for k in the $(0,0)-(\pi,\pi)$ direction [15, 16]. With Raman and far-infrared spectroscopy, good progress has been made in the observation of low-energy excitations in the superconducting state, and even a substantial convergence in the interpretation has been achieved. Comparison with various models favours scenarios with nodes in the gap, at least for $Bi_2Sr_2CaCu_2O_8$(ARPES measurement), $Tl_2Ba_2CuO_{6-y}$ (Raman measurements)

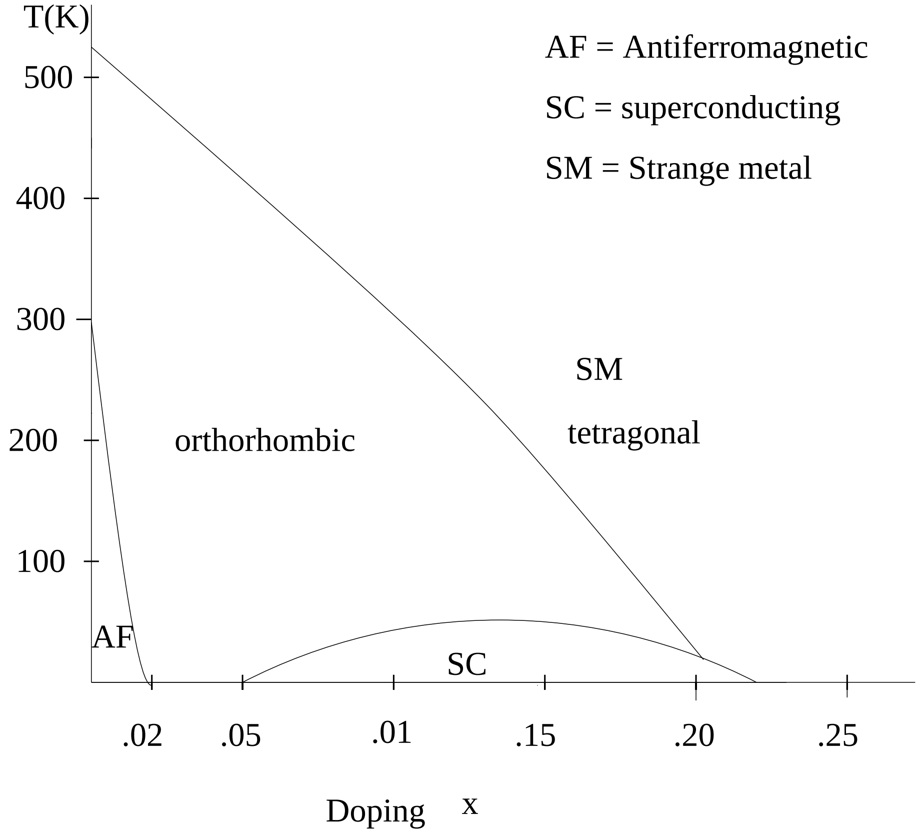

Figure 1.3: *Phase diagram of* $La_{2-x}Sr_xCuO_4$.

and for $La_{2-x}Sr_xCuO_4$ (IR spectroscopy). Direct evidence for a sign-reversal of the order parameter as a function of $\vec{k}$ around the Fermi surface comes from two different types of experiment. The first involves a SQUID(Superconducting Quantum Interference Device), made out of a loop containing a YBCO single crystal and a s-wave superconductor which shows that a half integer of flux quantum is trapped inside the loop [17, 18]. The second experiment is by connecting three thin crystal films of a HTSC with different orientations on the same epitaxial base. Again half a quantum of flux is trapped in the ring [19]. The two materials tested were $Tl_2Ba_2CuO_6$ and $YBa_2Cu_3O_7$.
Recent far infrared measurements of underdoped $Bi_2Sr_2CaCu_2O_{8+\delta}$ suggest the existence of a pseudo-gap in the ab-plane conductivity [20]. These results are similar to those reported several years ago for $YBa_2Cu_3O_{7-\delta}$ by a number of groups [21, 22, 23]. This pseudo-gap has approximately the same temperature and doping dependence as the suppression of the spin susceptibility measured

by nuclear magnetic resonance (NMR) and by inelastic neutron scattering (INS) [24]. Particularly noteworthy in this context is the observation of a normal state gap at the Fermi surface centred around the $k = (\pm\pi, 0)$ and $k = (0, \pm\pi)$ points in underdoped $\mathrm{Bi_2Sr_2CaCu2O_8}$ [25]. Taken together these observations hint that the pseudo-gap phenomenon might be of a primarily magnetic nature. The fact that magnetic and superconducting correlations occur in these materials at a comparable energy scale implies the need for theoretical frameworks that go beyond the classical models of superconductivity. For $\mathrm{La}_{2-x}\mathrm{Sr}_x\mathrm{CuO}_4$ there are conflicting reports based on transport measurements [26, 27] regarding the existence of a universal energy scale, which could correspond to a pseudo-gap. Recent NMR measurements [28] of the spin-lattice relaxation rate ($1/\mathrm{TT}_1$) for underdoped $\mathrm{La}_{1.89}\mathrm{Sr}_{0.11}\mathrm{CuO}_4$ showed a peak at 10K above T_c. However, the same effect was observed for the overdoped sample $\mathrm{La}_{1.82}\mathrm{Sr}_{0.18}\mathrm{CuO}_4$, which is unexpected given the fact that a pseudo-gap is generally believed to be a characteristic property of the underdoped materials. In the same set of measurements there was no suppression of the Knight shift above T_c. In this thesis we concentrate on optimally doped and overdoped materials. No clear evidence for a pseudo-gap was obtained in these crystals (see chapter 3).

In the underdoped high T_c materials the ab-plane resistivity ρ close to T_c shows $d\rho/dT < 0$ whilst for optimally doped samples $d\rho/dT > 0$ and $\rho \propto T$. As in conventional Fermi liquids $\rho \propto T^2$ at sufficiently low temperatures (*i.e.* where electron-electron interactions dominate over electron-phonon interactions), the resistivity data of the high T_c cuprates suggest that these materials do not behave according to the Fermi liquid theory. The normal state conductivity $\sigma_1(\omega)$ (obtained from FIR measurements) for the ab-plane cannot be fitted with only a Drude model, which is normally used for a metal. It requires several oscillators to represent the Mid Infrared (MIR) region. An alternative approach to analyze the conductivity is to adopt a frequency dependent scattering rate $\gamma(\omega)$ and effective mass $\mathrm{m}^*(\omega)$ in the expression for the frequency dependent conductivity. This approach is based on the assumption that the low frequency dynamical properties can be described by a single band of charge carriers, which interact both among themselves, and which are coupled to some kind of bosons. These bosons may be either phonons, or collective modes of the charge carriers such as paramagnons or plasmons. For a Fermi liquid the scattering rate is proportional to the frequency squared i.e. $\gamma(\omega) \propto \omega^2$ (close to $\omega = 0$). In contrast for the optimally doped high T_c cuprates it was shown by Schlesinger that $\gamma(\omega) \propto \max(\omega, T)$. Historically this observation has been a key argument for non-Fermi liquid approaches by a number of groups, notably Varma [29] and Anderson [30].

1.3 Theoretical Situation

Undoubtedly the most poignant question in the field of superconductivity concerns the mechanism responsible for the stabilization of the superconducting state in the cuprates up to temperatures as high as 164 K [31], i.e. one-sixth of their melting point temperature, and over halfway up to the melting point of ice. Indeed, many theoretical models for 'the' mechanism of superconductivity in the cuprates have been proposed so far, but a complete microscopic theory still seems far from being universally accepted. However, substantial progress has been made over the years in several directions. First and foremost, thanks to the gradual improvement in the preparation of single crystals and epitaxial thin films of many different superconducting compounds, as well as the improvement in experimental techniques, reproducibility of the results has improved considerably; in many cases, similar experimental data are acquired in different laboratories on the same materials.

In this thesis we will concentrate mainly on experiments motivated by those theoretical schools which attribute the superconductivity to electronic mechanisms. In chapter 3 we concentrate on the in-plane low energy electrodynamical properties of the high T_c cuprate $La_{2-x}Sr_xCuO_4$. Our observed low temperature and low frequency spectra support the d-wave pairing hypothesis. The conventional mechanisms, based on electron-phonon mediated pairing give rise to s-wave pairing with an isotropic (or at best a weakly anisotropic) order parameter. Order parameters which change sign as a function of momentum, such as d-wave pairing, are usually associated with an electronic mechanism. One of these mechanisms, the coupling of electrons to paramagnons, has been strongly advocated by Pines and collaborators, but many earlier reports exist in the literature where d-wave pairing was derived from the t-J model and related models [32, 33]. Quite generally, if electrons attract each other while occupying neighbouring sites, while experiencing a repulsion if they occupy the same site, this leads to superconductivity with an anisotropic order parameter (mixed s+id, p-wave, or d-wave) [34, 35].

The structure of the cuprates can be pictured as a stack of metallic planes separated by an insulating material, this stacking resembles a Josephson junction. On the one hand this leads to a strong anisotropy of the electronic transport in the normal state. The cuprate's anisotropy ratio for the resistivity, ρ^{ab}/ρ^{c}, varies from 10^5 (in $Bi_2Sr_2CaCu_2O_8$) to 30 - 70 (in fully oxygenated $YBa_2Cu_3O_7$) [36]. This is a variation of 3 orders of magnitude. In addition the c-axis conductivity (for single layer compouds) even for an optimally doped sample is below the Mott-Ioffe minimum for a metal.

A second consequence of the anisotropy is that in the superconducting state the critical current should be strongly anisotropic, and the current-voltage measurements should reveal the non-linear characteristics of a Josephson coupled device. In the context of classical superconductivity, Josephson predicted that a zero-voltage supercurrent $J_J \sin(\phi)$ flows between two superconducting reservoirs of Cooper-pairs separated by a tunnelling barrier. Here ϕ is the phase difference between the two superconductors and J_J is the (Josephson) critical current density. This is called the Josephson effect and has been widely studied in devices based on conventional superconductors during the 60's and 70's, in particular because it was hoped that a new generation of ultra-fast micro-electronic devices could be based on the Josephson effect. This technology has received renewed interest now that superconducting devices can be produced which operate at liquid nitrogen temperature. In principle the Josephson effect could arise in the high T_c superconductors due to tunnelling between adjacent copper-oxygen planes. This is called the intrinsic Josephson effect and was indeed observed by Kleiner *et al.* [37]. In the context of BCS theory the Josephson effect arises as a natural consequence of two superconducting reservoirs of Cooper-pairs separated by a tunnelling barrier. On a microscopic level the charge transport between the two reservoirs is by tunnelling of single (unpaired) charge carriers. In the normal state this leads to a tunnelling conductance proportional to $N(0)e^2/\tau$ where $1/\tau$ is the tunnelling rate and $N(0)$ is the density of states at the Fermi energy per CuO_2. Based on the microscopic theory of Bardeen Cooper and Schrieffer, Ambegaokar and Baratoff have shown that in the superconducting state the critical current through the barrier is proportional to $\Delta a^2\sigma_n/ed$. Where Δ is the superconducting gap, σ_n the tunnelling conductance and d the distance between the two superconductors. Hence the relation between J_J and the normal state conductivity σ_n is:

$$J_J = \frac{\pi a^2 \Delta \sigma_n}{2ed} \tag{1.3}$$

where d is the distance between the planes, a is the in-plane lattice constant and Δ is the superconducting gap in BCS theory.

The existence of a Josephson coupling between the copper-oxygen planes has been treated on a fundamentally different microscopic level by Chakravarty and Anderson [38]. In Anderson's theory of high T_c superconductivity [30] the charge transport between planes is mediated exclusively by tunnelling of pairs of charge carriers, whereas transport by single carriers is an incoherent process. The incoherence of single charge carrier transport is born out by the fact that for fields perpendicular to the planes the optical conductivity is spread over an anomalously broad frequency range. In chapter 4 of this thesis this is shown for the case of $La_{1.85}Sr_{0.15}CuO_4$. Also it is shown in this chapter that the conductivity increases considerably for the overdoped case $La_{1.80}Sr_{0.20}CuO_4$. This behaviour reflects a confinement of single charge carriers to the planes, and could be due to spin-charge separation as a result of the strong correlation effects discussed above. The Chakravarty-Anderson model then leads to a superconducting mechanism where T_c is found to be proportional to the rate of tunnelling of pairs of charge carriers between the planes. However, the Josephson critical current is just the pair-tunnelling rate. Hence a universal relation between J_J and T_c was predicted by Anderson [39], which is a unique consequence of his theory and has the following form

$$J_J = \frac{2e}{\hbar} E_{cond} \approx \frac{eN(0)k_B^2}{3\hbar} T_c^2 \tag{1.4}$$

where E_{cond} is the condensation energy per unit of CuO_2 and k_B is the Boltzmann constant. In Chapter 5 of this thesis the validity of the latter relation is tested experimentally. For this test we take advantage of a well-known relation between J_J and the Josephson plasma frequency: $\omega_J^2 = 8\pi^2 J_J \Phi_0^{-1} d^{-1}$ (where $\Phi_0 = hc/2e$ is the quantum of flux), and measure the plasma edge ω_J using optical techniques. The implication appears to be, that Eq. 1.4 is not observed experimentally. Thus one important implication of the confinement hypothesis(incoherent interlayer transport of normal carriers) is confirmed by the work presented in this thesis, but the second implication (the relation between T_c and J_J) is found to be contradicted by our experiments. The results described in chapter 5 were recently confirmed by the experimental group at Princeton university [40], who measured the interlayer Jopsephson penetration depth (λ_J) on the same samples using the scanning SQUID technique. The plasma frequency is directly related to λ_J through the relation $\lambda_J = c/\omega_J$.
Let us finally consider the value of J_J directly. Generally speaking we would expect that the larger the distance between the CuO_2 planes i.e. d, the weaker the Josephson coupling. Within the Anderson-Chakravarty model this should result in a lower value of T_c. This trend is not confirmed if we compare the experimental values for various single-layer cuprates: For example in $La_{1.85}Sr_{0.15}CuO_4$ d is 6.6 $\AA$ and T_c is 32K, while in $Tl_2Ba_2CuO_6$ d is 11.57 $\AA$ and T_c is 85K. We see that the distance (d) is larger for the thallium compound, yet T_c is also larger.

1.4 Infrared Spectroscopy

In the experiments described in this thesis we use infrared spectroscopy, and measure the reflected intensity on the vacuum/sample interface of single crystalline materials. The reference used to calibrate all reflectivity spectra is usually a gold mirror, which for the frequency range being considered has a reflectivity between 99.5 and 100 %. By using the Kramers-Kronig relations we determine the frequency dependent phase of the reflected light. By inverting the Fresnel expressions for the reflection coefficient we obtain the real and imaginary part of the complex frequency dependent dielectric function $\epsilon(\omega)$.

The imaginary part of the dielectric function corresponds to $4\pi\mathrm{Re}\sigma/\omega$ where σ is the optical conductivity. The real part of $\sigma(\omega)$ is precisely the rate of absorption of the energy flux of transverse electromagnetic waves propagating through the medium ($\sigma = d\ln(S)/dt$, where S is the Poynting vector). In the Kubo formalism $\sigma(\omega)$ corresponds to the current-current correlation function of the material, and has contributions both from electronic degrees of freedom, e.g. electron-hole excitations of 'dressed' electrons, and transverse optical phonons. Based upon the low energy excitations, one can determine whether the material is a metal, an insulator or a semiconductor. By comparing $\mathrm{Re}\sigma(\omega)$ above and below T_c we determine the transfer of spectral weight of the unpaired charge carrier response function to the δ-function at zero energy, which is a measure of the superfluid density. In chapter 3 we compare $\mathrm{Re}\sigma(\omega)$ to model calculations assuming different symmetries of the order parameter.

The FIR spectrometer used for all measurements described in this thesis has a measurement range of 10 cm^{-1} (1.2 meV) up to 8000 cm^{-1} (1 eV). To date, FIR measurements of HTSCs have been performed at near normal angle of incidence. However for materials whose normal state reflectivity is close to unity, the superconducting induced changes are small. This drawback may be overcome by increasing the angle of incidence, hereafter referred to as Polarised Angle Resolved Infrared Spectroscopy (PARIS) and is the main subject of this thesis. A second application of PARIS turned out to be crucial in studying the c-axis optical response of single crystals of many of the high T_c superconductors. More often than not these crystals have a dimension along the c-axis which is only a fraction of a millimetre, making them unsuitable for reflectivity measurements of the ac-face of the crystal. The dimensions along the a and b axis are often several square mm so that a mosaic must be made in order to obtain a reasonable reflected signal. In chapter 5 of this thesis we use the PARIS technique to extract the c-axis optical response of such crystals from grazing incidence measurements on the ab-plane.

References

[1] J. G.Bednorz and K. A. Müller, Z. Phys B **64**, 189 (1986).

[2] Z.-X. Shen, J. W. Allen, J. Jeh, J. S. Kang, W.Ellis, W. Spicer, I. Linda, M. B. Maple, Y. Dalichaoch, M. S. Torikachvili, J. Z. Sun, and T. H. Geballe, Phys. Rev. B **36**, 8414 (1987).

[3] D. van der Marel, J. van Elp, G. A. Sawatzky, and D. Heitmann, Phys. Rev. B **37**, 5136 (1988).

[4] L. F. Matheiss and D. R. Hamann, Phys. Rev. B **38**, 5012 (1988).

[5] H. Eskes, Ph.D. thesis, University of Groningen, 1992.

[6] S. Uchida, T. I. H.Takagi, T. Arima, Y. Tokura, and S. Tajima, Phys. Rev. B **43**, 7942 (1991).

[7] J. P. Falk, A. Levy, M. A. Kastner, and R. J. Birgenau, Phys. Rev. Lett. **69**, 1109 (1992).

[8] J. Zaanen, G. A. Sawatzky, and J. W. Allen, Phys. Rev. Lett. **55**, 418 (1985).

[9] H. Eskes and G. A. Sawatzky, Phys. Rev. Lett. **61**, 1415 (1988).

[10] F. C. Zhang and T. M. Rice, Phys. Rev. B **37**, 3759 (1988).

[11] L. F. Feiner, J. H. Jefferson, and R. Raimondi, Phys. Rev. B **53**, 8751 (1996).

[12] B. Keimer, Phy.Rev B. **46**, 14034 (1992).

[13] S. Uchida, K. Tamasaku, and S. Tajima, Phys. Rev. B **53**, 14558 (1996).

[14] B. Büchner, M. Breuer, A. Freimuth, and A. P. Kampf, Phy. Rev. Lett. **73**, 1841 (1994).

[15] Z.-X. Shen, W. E. Spicer, D. M. King, D. S. Dessau, and B. O. Wells, Science **267**, 343 (1995).

[16] H. Ding, T. Yokoya, J. C. Campuzano, T. Takahashi, M. Randeira, M. R. Norman, T. Mochiku, K. Kadawaki, and J. Giapintzakis, Nature **382**, 51 (1996).

[17] D. A. Wollman, D. J. Harlingen, D. M. Ginsburg, and A. J. Leggett, Phys. Rev. Lett. **71**, 2134 (1993).

[18] D. A. Brawner and H. R. Ott, Phys. Rev. B **50**, 6530 (1994).

[19] J. R. Kirtley, C. C. Tsuei, J. Z. Sun, C. C. Chi, L. S. Yu-Jahnes, A. Gupta, and M. R. M. B. ketchen, Nature **373**, 225 (1995).

[20] A. V. Puchkov, P. Fournier, D. N. Basov, T. Timusk, A. Kapitulnik, and N. N. Koleshnikov, Phys. Rev. Lett. **77**, 3212 (1996).

[21] J. Orenstein, G. A. Thomas, A. J. Millis, S. L. Cooper, D. H. Rapkine, T. Timusk, L. F. Schneemeyer, and J. V. Waszczak, Phys. Rev. B **42**, 6242 (1990).

[22] D. van der Marel, H.-U. Habermeier, D. Heitmann, W. König, and A. Wittlin, Physica C **176**, 1 (1991).

[23] Z. Schlesinger, R. T. Collins, F. Holtzberg, C. Feild, and A. Gupta, Phys. Rev. B **41**, 11237 (1990).

[24] J. Rossat-Mignod, L. P. Regnault, C. Vettier, P. Burlet, and J. Y. Henry, Physica **192**, 109 (1994).

[25] D. S. Marshall, D. S. Dessau, A. G. Loeser, C.-H. Park, A. Y. Matsuura, J. N. Eckstein, I. Bozovic, P. Fournier, A. Kapitulnik, W. E. Spicer, and Z.-X. Shen, Phys. Rev. Lett. **76**, 4841 (1996).

[26] H. Y. Hwang, B. Batlogg, H. Takagi, H. L. Kao, J. Kwo, R. J. Cava, J. J. Krajewski, and W. F. Peck, Phys. Rev. Lett. **72**, 2636 (1994).

[27] Y. Nakamura and S. Uchida, Phy. Rev. B. **47**, 8369 (1993).

[28] Y. Itoh, M. Matsumura, and H. Yamagata, Intl. Jnl. Low Temp. Phys. **105**, 365 (1996).

[29] C. M. Varma, Phys. Rev. B **55**, 14554 (1997).

[30] P. W. Anderson, *The Theory of Superconductivity in High-T_c Cuprates* (Princeton University Press, Princeton USA, 1997).

[31] L. Gao, Y. Y. Xue, F. Chen, Q. Xiong, R. L. Meng, D. Rameirez, C. W. Chu, J. H. Eggert, and H. K. Mao, Phys. Rev. B **50**, 4620 (1994).

[32] C. Gros, R. Joynt, and T. M. Rice, Z. Phys. B **68**, 425 (1987).

[33] G. Kotliar and J. Liu, Phys. Rev. B **38**, 5142 (1988).

[34] L. F. Feiner, J. H. Jefferson, and R. Raimondi, Phys. Rev. Lett. **76**, 4939 (1996).

[35] D. van der Marel, Phys. Rev. B **51**, 1147 (1995).

[36] Y. Iye, *Physical Properties of HTSC's volume 3 Ed. D. Ginsburg* (World Scientific, Singapore, 1992).

[37] R. Kleiner, F. Steinmeyer, G. Kunkel, and P. Müller, Phys. Rev. Lett. **68**, 2394 (1992).

[38] S. Chakravarty, A. Sudbo, P. W. Anderson, and S. Strong, Science **261**, 337 (1993).

[39] P. W. Anderson, Science **268**, 1154 (1995).

[40] K. A. Moler, J. R. Kirtley, R. Liang, D. Bonn, and W. Hardy, Phys. Rev. B **55**, 12753 (1997).

2

Optical Properties of Metals and Superconductors

In this chapter the fundamental equations used in optical spectroscopy will be presented. This chapter is meant as an aid to understanding the analysis of polarized angle dependent infrared reflectivity measurements of anisotropic materials.

2.1 Interaction of Light With a Medium

2.1.1 Maxwell's Equations

The propagation of electro-magnetic waves in a dielectric medium is given by the well known Maxwell equations [1], which relate the displacement field vector ($\mathbf{D}$), the electric field ($\mathbf{E}$), the magnetic flux density ($\mathbf{B}$), and the magnetic field ($\mathbf{H}$) to the charge (ρ) and current density ($\mathbf{J}$) [1]

$$\begin{array}{lcll} \nabla\cdot\mathbf{D} & = & 4\pi\rho & \text{(Coulomb)} \\ \nabla\cdot\mathbf{B} & = & 0 & \\ \nabla\times\mathbf{H}-c^{-1}\partial\mathbf{D}/\partial t & = & 4\pi\mathbf{J} & \text{(Ampère)} \\ \nabla\times\mathbf{E}+c^{-1}\partial\mathbf{B}/\partial t & = & 0 & \text{(Faraday)} \end{array} \tag{2.1}$$

The usual convention in optics is to treat the charge density ρ and the current density $\mathbf{J}$ (which together satisfy the continuity relation ($\nabla\cdot\mathbf{J}+\partial\rho/\partial t=0$) as strictly *external* charges. In other words, one adopts the convention that $\rho=0$ and $\mathbf{J}=0$ everywhere, except inside the external source where the electromagnetic waves are generated. This choice corresponds to defining all currents in the solid as bound charge currents. This can also be used for non-stationary fields and currents if the material contains free carriers. Inside the solid the ratio between the magnetic flux density $\mathbf{B}$ and the magnetic field $\mathbf{H}$ is given by the magnetic permeability tensor $\mu(k,\omega) = \mathbf{B}/\mathbf{H}$ which is a material property. In this thesis we will only discuss nonmagnetic materials for which μ is very close to unity. We therefore restrict the discussion to the case where $\mu = 1$.

In order to close the four Maxwell equations we need a constant which defines the relative strength of the displacement field vector $\mathbf{D}$ and the electric field $\mathbf{E}$. The ratio $\mathbf{D}/\mathbf{E} = \epsilon(\mathbf{k},\omega)$ is the dielectric tensor. This is a constant of the materials, which has a longitudinal ($\mathbf{E} \parallel \mathbf{k}$) and two transverse ($\mathbf{E} \perp \mathbf{k}$) components. In the limit $\mathbf{k} \to 0$ the dielectric tensor becomes independent of the direction of $\mathbf{k}$, and the distinction between transverse and longitudinal dielectric tensor elements disappears. The tensor ϵ has both a real and an imaginary part. The real part causes a dispersion of propagating electromagnetic waves in the medium (polaritons) as explained in the next subsection. The imaginary part describes the dissipation of these waves.

Above we described the first approach to close the Maxwell equations, where we have adopted the convention $\mathbf{J} = 0$ in Ampère's law. Often a second approach is used, where in Ampère's law we put $\mathbf{J} = \sigma(\omega)\mathbf{E}$ and $\mathbf{D} = \mathbf{E}$. Here σ is the optical conductivity. This corresponds to describing the macroscopic polarization inside the solid induced by the external current source as an internal current distribution. The constants of the material ϵ and σ can be used interchangeably, and they are linked by the expression

$$\epsilon = 1 + \frac{i4\pi\sigma}{\omega} \tag{2.2}$$

2.1.2 Solution of Maxwell's Equations in a Medium

In a vacuum the solutions of the Maxwell equations correspond to transverse polarized plane waves, or light. No solutions exist for which the polarization is longitudinal. This situation changes when considering solids. In a solid the general form of the Maxwell equations is:

$$\nabla \times \nabla \times \mathbf{E} = -\frac{\epsilon}{c^2}\frac{\partial^2 \mathbf{E}}{\partial t^2} \tag{2.3}$$

Both longitudinal and transverse solutions are now possible. The longitudinal solutions correspond to having $\mathbf{k} \times \mathbf{E} = 0$, which implies that

$$\epsilon(\mathbf{k},\omega) = 0 \tag{2.4}$$

The solutions of this equation are the longitudinal phonons if they correspond to vibrations, and plasmons if they correspond to collective oscillations of the free

charge carrier density. Often these modes occur in close proximity of each other, so that the modes are of strongly mixed phonon-plasmon character.
The second type of solution is of the form $\mathbf{k} \cdot \mathbf{E} = 0$, implying that they are transversely polarized electromagnetic waves, which satisfy

$$\epsilon(\mathbf{k}, \omega) = \frac{k^2 c^2}{\omega^2} \tag{2.5}$$

These so-called polaritons correspond to transverse electromagnetic travelling waves, coupled to propagating polarization waves of the medium. In optical spectroscopy in the infrared and visible range typical values of k are of the order of $10^{-3}/a$, where a is the lattice constant, or less. Typically dispersion of the material properties takes place for k of the order of a reciprocal lattice vector. Hence the k-dependance of $\epsilon(\mathbf{k}, \omega)$ can be neglected on this scale. This also implies that the difference between longitudinal and transverse dielectric tensor components of $\epsilon(\omega)$ becomes vanishingly small. Let us furthermore consider an electromagnetic wave with the electric field along one of the optical axis of the solid, travelling along the $\hat{\mathbf{z}}$ direction. In this case the solution of the above equation acquires a particularly simple form, namely

$$\mathbf{E}(z, t) = \mathbf{E}_0 \exp\left\{ i\omega(\hat{n}_z z/c - t)\right\} \tag{2.6}$$

where c is the velocity of light in vacuum, $c/\hat{n}_z$ the velocity of light in the medium. The index of refraction $\hat{n} = \sqrt{\epsilon(\omega)}$ is again a complex valued tensor, and $\hat{n}_z$ is the diagonal element along one of the optical axes. Below we will use the index of refraction to define the expressions for reflection and refraction at the interface between two media.

2.1.3 The Fresnel Equations

The Fresnel equations for an anisotropic medium relate the complex reflection at the interface between two media to the index of refraction of these media and the angle of incidence. The most general case considered in this thesis concerns the reflection coefficients on the vacuum/solid interface with light incident at a finite angle θ with the surface normal. We will consider anisotropic materials, with the sample surface cut at right angles with respect to one of the optical axes. The optical alignment is chosen such, that the plane formed by the incident and reflected wavevector of the light coincides with the plane formed by two of the optical axes of the crystal (see Fig. 2.1).
The reflection and transmission coefficients of light at the vacuum/solid interface can be calculated by considering the following boundary conditions, which result from the Maxwell equations. The components of $\mathbf{E}$ and $\mathbf{H}$ parallel to the interface, and the components of $\mathbf{D}$ and $\mathbf{B}$ perpendicular to the interface, should be

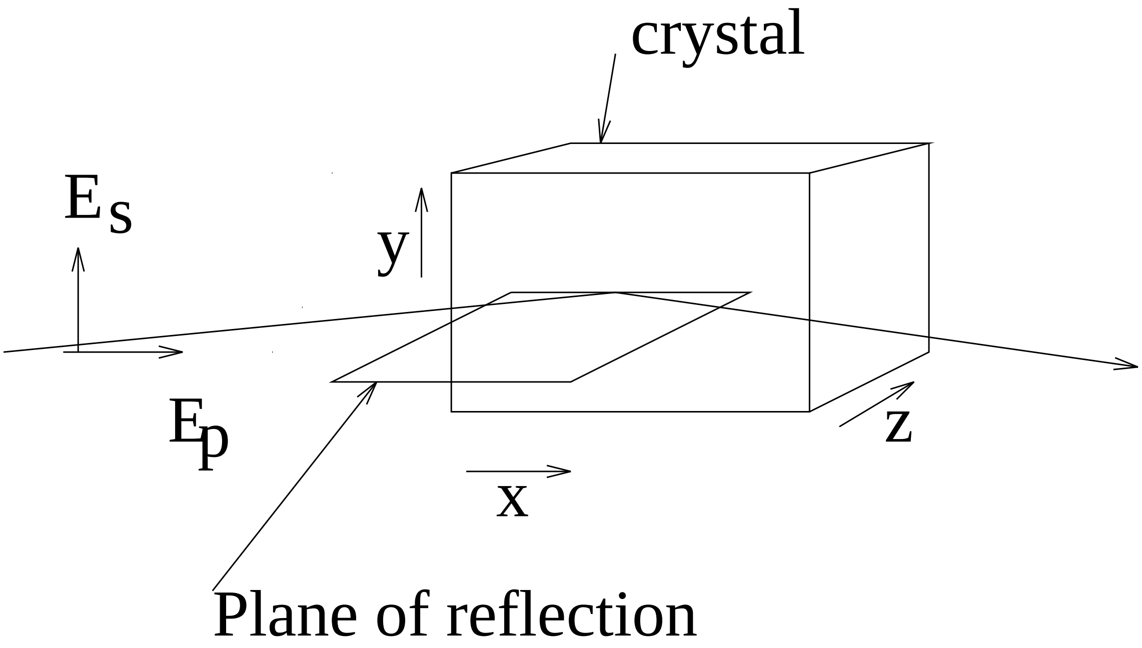

Figure 2.1: *Crystallographic directions used for the definition of the r_p and r_s. Note the plane of reflection is at an angle of 90° to the crystal surface xy*

continuous.

Let us define **z** as the surface normal, **y** as the direction parallel to the surface and perpendicular to the plane of reflection, and **x** as the intersection of the plane of reflection with the sample surface (see Fig. 2.1). We consider the case where these directions coincide with the optical axes of the solid. In this case we can define n_α, where $\alpha = x, y, z$, as the tensor components of the index of refraction along these three optical axes. For the polarization of the light we will consider two possibilities: either the light is polarized with $\mathbf{E} \parallel \mathbf{y}$ ('senkrecht', or s-polarization) or $\mathbf{E} \perp \mathbf{y}$ ('parallel', or p-polarization). The geometrical picture of this orientation is shown in Fig. 2.1. The corresponding expressions for the reflection coefficients are

$$r_p = \frac{\hat{n}_x \hat{n}_z \cos\theta - \sqrt{\hat{n}_z^2 - \sin^2\theta}}{\hat{n}_x \hat{n}_z \cos\theta + \sqrt{\hat{n}_z^2 - \sin^2\theta}} \tag{2.7}$$

$$r_s = \frac{\cos\theta - \sqrt{\hat{n}_y^2 - \sin^2\theta}}{\cos\theta + \sqrt{\hat{n}_y^2 - \sin^2\theta}} \tag{2.8}$$

These coefficients are the electric field amplitudes of the reflected waves relative to the incident waves. In our experiments we use detectors which are sensitive to the intensity of the reflected light, which is proportional to the absolute square of the electric field amplitudes. Unfortunately the information on the phase of the reflected light is lost this way. By calibrating this intensity to a reference material with close to 100 % reflectivity (for our particular frequency range, usually gold), we obtain the absolute square of the reflection coefficients. Since the primary aim of this kind of measurements is to obtain the complex dielectric function $\epsilon(\omega)$, an additional step is required to determine the phase of the reflected light. For this purpose one often uses Kramers Kronig relations, by taking advantage of the fact that $\ln r(\omega)$ has a real part which is calculated directly from the experiment, and an imaginary part which is the phase of the reflected light, $\phi(\omega)$. For reflection at a not too large angle of incidence the function $\ln r(\omega)$ has the analytical behaviour of a causal response function. We can then use Kramers-Kronig relations to calculate the phase spectrum starting from $\mathrm{Re}\ln r(\omega)$. After which we can invert Eqns. 2.7, 2.8 and obtain the complex refractive index $\hat{n}$. From this we can calculate the dielectric function ϵ ($\hat{n}^2 = \epsilon$).

$$r(\omega) = \sqrt{R(\omega)}e^{i\phi(\omega)} \tag{2.9}$$

$$\ln r(\omega) = \frac{1}{2}\ln R(\omega) + i\phi(\omega) \tag{2.10}$$

$$\phi(\omega) = -\frac{\omega}{\pi}\int_0^\infty \frac{\ln R(\omega') - \ln R(\omega)}{\omega'^2 - \omega^2}d\omega' \tag{2.11}$$

In Eqn. 2.11, the fact that the lower limit is 0 and the upper limit of integration is ∞ poses some practical limitations on the accuracy of this method to calculate the phase of the reflection coefficient. Of course measurements are limited to a finite frequency interval. Often one combines the optical data in the infrared and optical range with data measured with soft X-rays and far UV to extend the frequency range as far as possible. Sometimes the experimental data contain a large section without optical oscillators, resulting in a constant value of reflectivity over a large frequency interval. In this case it is justified to extrapolate this value of reflectity up to infinity. This corresponds to shifting the optical oscillator strength at higher frequencies than the measured range to infinity. At the low frequency side one extrapolates the reflectivity with a constant value if the material is an insulator, with a Hagen-Rubens extrapolation if it is a metal, and with a two-fluid form if it is a superconductor [2]. The implementation of Kramers-Kronig relations for reflectivity at grazing angle of incidence, relevant to this thesis, will be discussed in Chapter 3.

2.2 Dielectric Properties of Metals

2.2.1 The Drude Model

The most naive model for the dynamical conductivity of electrons in a free electron metal is the classical Drude model. It is based upon treating the charge carriers as a classical gas of free electrons. It ignores all interactions between electrons beyond the long range Coulomb forces, all effects due to the periodic potential imposed by the crystal structure and the Coulomb attraction of the positive ionic cores. The model does to a limited extent take into account the effect of scattering, but only in the form of a classical dissipative term in the Lagrangian. From this perspective its relative success for the description of the optical properties and transport properties of prototypical metallic materials such as aluminum is perhaps surprising.

As a matter of fact surprisingly little progress has been made in extending the microscopic theory of optical spectra of interacting electrons beyond the Drude model in a systematic way. The main result of Drude theory, which is more than 100 years old, can be summarized in the corresponding form for the optical conductivity:

$$\sigma(\omega) = \frac{\sigma_0}{1 - i\omega\tau} \tag{2.12}$$

where the DC conductivity is $\sigma_0 = ne^2m^{-1}\tau$, n is the charge carrier density, m is the mass, e is the charge and τ is the life-time of the charge carriers.

An important sum rule in the theory of optical spectra, which follows directly from the Kubo-formalism is the f-sum rule, which states that

$$\int_0^\infty \mathrm{Re}\sigma(\omega)d\omega = \frac{\pi ne^2}{2m} \tag{2.13}$$

This sum rule is of course satisfied by the Drude formula for the optical conductivity of a classical electron gas and is also valid for a liquid of interacting electrons if the upper limit of excitation frequency is sufficiently large. In the analysis of optical spectra we sometimes use weaker forms of the sumrule. For example if due to interactions the quasiparticles acquire an effective mass m^*, which is always larger than the mass of the non-interacting charge carriers, the optical conductivity spectrum will in principle consist of two parts. First a coherent low energy part, which has a Lorentzian lineshape with a width corresponding to the inverse quasiparticle lifetime. Second an incoherent part at higher energies. The appearance of the latter reflects the fact that the low energy quasiparticles are free electrons dressed with bosonic excitations. These bosons can be phonons, collective modes of the electron liquid, or both. The incoherent side bands of the quasiparticle Drude peak are indicated as Holstein peaks in the theory of strong electron-phonon coupling. In practice the coherent and incoherent parts of the spectrum may overlap. Let us suppose for the moment that they can be separated into a coherent part for frequencies below ω_c and an incoherent part above ω_c. In this case a weaker form of the sum rule exists

$$\int_0^{\omega_c} \mathrm{Re}\sigma(\omega) d\omega = \frac{\pi n e^2}{2m^*} \tag{2.14}$$

which can be used to calculate the effective mass m^* from the optical spectra. By combining the strong and weak form of the sumrule, we see that the spectral weight in the incoherent part must satisfy

$$\int_{\omega_c}^{\infty} \mathrm{Re}\sigma(\omega) d\omega = \frac{\pi n e^2}{2}\left(\frac{1}{m} - \frac{1}{m^*}\right) \tag{2.15}$$

It is common within the FIR optical community to use the partial form of the sum rule to determine the effective number of carriers per formula unit ($N_{eff} m/m^*$ see chapter 3). Actually for a strongly correlated electronic system, if one does not integrate the conductivity to a sufficiently high enough frequency the integral gives the effective kinetic energy i.e. how strongly the elctrons are correlated, rather than the effective number of carrier. A sufficiently high enough frequency is above the upper Hubbard band where the electrons have free electron like states.

2.2.2 Low Frequency Optical Response of Metals

Even in metals where the Drude model is no longer a valid approximation, it nevertheless remains a useful characterization, when analyzing optical data in the limit where $\omega \to 0$. In the Drude model, for very small frequencies where $\omega\tau \ll 1$

$$\begin{aligned} \mathrm{Re}\epsilon(\omega) &= 1 - 4\pi\sigma_0\tau \\ \mathrm{Im}\epsilon(\omega) &= 4\pi\sigma_0/\omega \end{aligned} \tag{2.16}$$

This is called the Hagen-Rubens region, where $\mathrm{Im}\ \epsilon \gg |\mathrm{Re}\ \epsilon|$. We furthermore observe, that in this limit

$$\mathrm{Im}\hat{n} = \mathrm{Re}\hat{n} = \sqrt{\frac{2\pi\sigma_0}{\omega}} \tag{2.17}$$

Therefore in the Hagen-Rubens range the optical properties of the material are determined solely by the DC conductivity. The penetration of electromagnetic waves inside the metal is an exponentially decaying function of the distance from the surface. The depth at which the electric field has fallen to $1/e$ of it's maximum value is called the skin depth δ.

$$\delta = \frac{c}{\omega \mathrm{Im}\hat{n}} = \frac{c}{\sqrt{2\pi\sigma_0\omega}} \tag{2.18}$$

and the reflection coefficient is

$$R = 1 - \sqrt{\frac{2\omega}{\pi\sigma_0}} \tag{2.19}$$

2.2.3 Generalized Drude Expression

There are two generalized expressions for the dielectric function ϵ which are currently used to interpret the optical spectra of HTSC's. The first uses a constant scattering rate γ (Ref. Eqn. 2.20) and the second uses a frequency dependent scattering rate $\gamma(\omega)$ and a renormalized effective mass m*/m (Ref. Eqn. 2.21)

$$\epsilon(\omega) = \epsilon_\infty - \frac{\omega_p^2}{\omega(\omega + i\gamma)} \tag{2.20}$$

$$\epsilon(\omega) = \epsilon_\infty - \frac{\omega_p^{*^2}}{\omega(\omega + i\gamma(\omega))} \tag{2.21}$$

where ω_p is the plasma frequency, given by $\omega_p = 4\pi ne^2/m$ and $\omega_p^{*^2} = \omega_p^2 m/m^*$. The latter approach is purely phenomenological and is based upon the treatment of mass enhancement in heavy Fermions and mixed valence compounds [3, 4]. The frequency dependence of the scattering rate is assumed to be due to free carriers interacting with a spectrum of optically inactive excitations. The strength of this interaction is expressed by the symbol λ where $m^*/m = 1 + \lambda$. For $YBa_2Cu_3O_7$ (T_c = 90K) λ is of the order of 3 [5] in the low frequency region and 1 in the high frequency region. The quasiparticles in a Fermi Liquid are only defined for energies close to the Fermi surface, namely as long as they fulfill the inequality $E_{qps} > \hbar\gamma(\omega)$. In other words the energy of the quasiparticles must be larger than the energy dependent scattering rate. For a Fermi liquid $\gamma(\omega) \propto \omega^2$ whilst for the cuprates $\gamma(\omega) \propto \omega$, thus again indicating the non-Fermi liquid behaviour of these materials.

Within the Luttinger liquid picture, with spin-charge separation, it has been demonstrated by P. W. Anderson [6] that the frequency dependence of the scattering rate $\gamma(\omega)$ is linear. However a Luttinger liquid solution has been demonstrated in one dimension, a solution for the two dimensional case has not been shown.

2.3 Optical Properties of a Superconductor

2.3.1 Electrodynamical properties of an Ideal Conductor

If a superconductor is first cooled down below some critical temperature and subsequently an external magnetic field is applied, surface currents will be generated to expel the magnetic field. In fact from this experiment one can not yet tell whether the material is an ideal conductor or a superconductor. This only becomes apparent if the external field is applied while the material is still above the critical temperature T$_c$, and subsequently the temperature reduced below T$_c$. An ideal conductor will trap the flux whilst a superconductor will expel it. The latter effect is called the Meissner effect. The Meissner effect and the zero resistance state together form the two properties which define the superconducting state. Unlike the experimental conditions necessary for the Meissner effect, in optical experiments the electric and magnetic fields have a time-dependence. As a result the optical response of a superconductor is identical to that of an ideal conductor. For an ideal conductor the scattering time $\tau \to \infty$, and $\mathrm{Re}\sigma = 0$ $(\omega \neq 0)$ so that

$$\epsilon(\omega) = \epsilon_\infty - \frac{c^2}{\lambda_L^2 \omega(\omega + i0^+)} \tag{2.22}$$

where λ_L is the London penetration depth and is defined by $\lambda_L = c/\omega_p$. It is perhaps useful to point out, that the imaginary part of this expression gives rise to a δ-function in the real part σ_1 of the optical conductivity,

$$\sigma_1(\omega) = \frac{c^2}{4\lambda_L^2}\delta(\omega) \tag{2.23}$$

This reflects the fact that in an ideal conductor static currents flow with vanishing resistivity. Unlike an ordinary metal, where the skin depth $\delta(\omega)$ diverges as $\omega^{-1/2}$ for low frequencies, in an ideal conductor the electromagnetic waves have a penetration depth

$$\delta = \frac{c}{\omega \mathrm{Im}\hat{n}} = \lambda_L \tag{2.24}$$

For a superconductor λ_L defines the penetration of the static magnetic fields into the solid. It also defines the screening length of vortices in a type II superconductor. Sometimes it is useful (e.g. see chapters 4 and 5 of this thesis) to define a superconducting plasma frequency $\omega_{ps}^2 = c^2/\lambda_L^2 = 4\pi q_C^2 n_s/m_C$, where $q_C = 2e$, m_C and n_s are the charge, the mass and the density of Cooper-pairs respectively. The upper panel of figure 2.2 shows the reflectivity of an ideal conductor, using the model parameters shown. The reflectivity is unity up to the screened plasma frequency ($\tilde{\omega}_p = \omega/\sqrt{\epsilon_\infty}$) of 3000 cm^{-1}, above this frequency the material becomes transparent. When a quantity has been normalized by a particular number

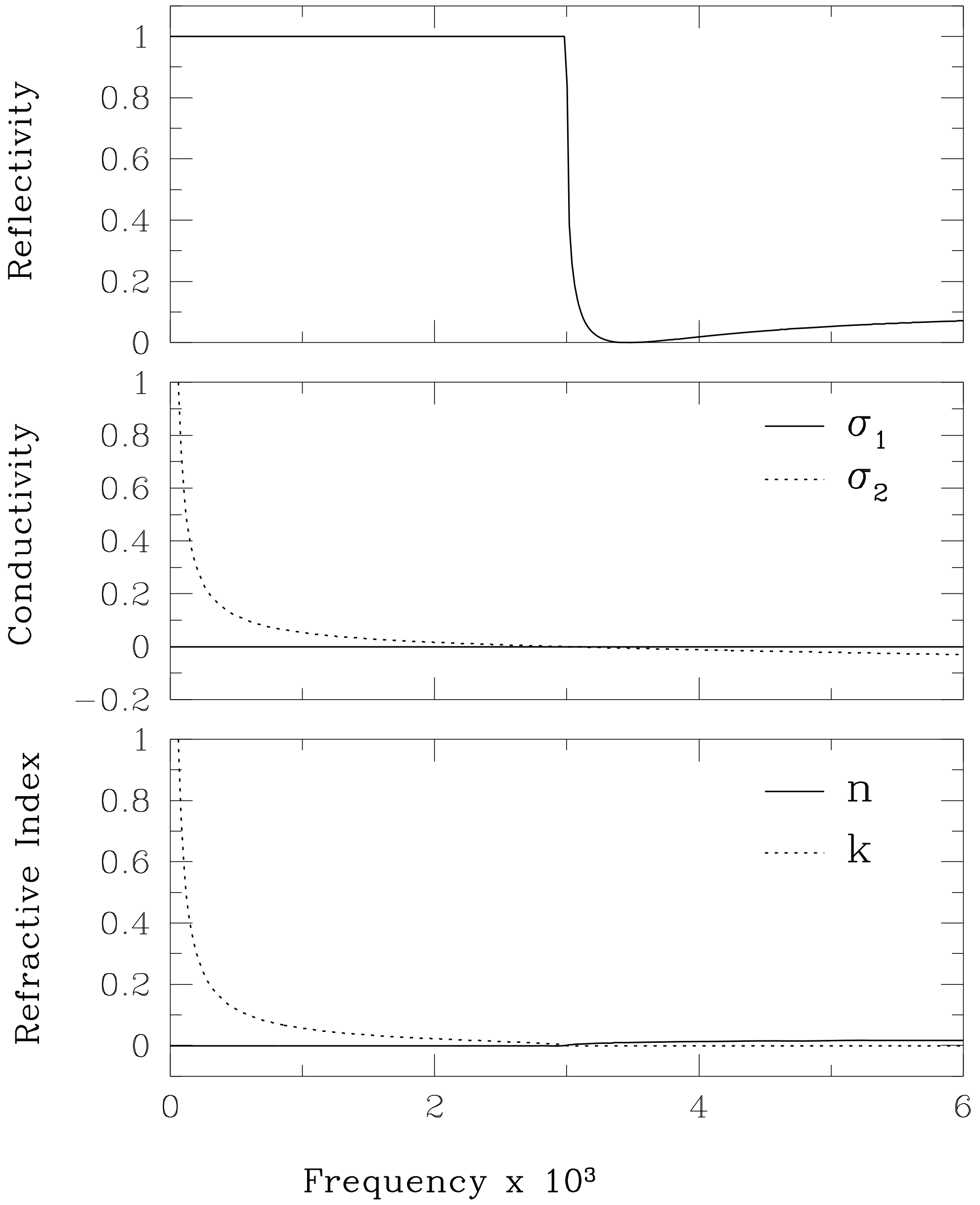

Figure 2.2: *Reflectivity, conductivity and refractive index of an ideal conductor. Parameters used were* $\omega_p = 6000$ *cm*$^{-1}$, $\epsilon_\infty = 4$ *and* $\gamma = 0$. $\sigma^{nml} = 10000$ *and* $\hat{n}^{nml} = 100$.

this is referred to by the superscript ^{nml}, see Fig. 2.2. The middle panel of Fig. 2.2 shows the complex conductivity, σ_1 is zero up to the screened plasma frequency. Both σ_1 and σ_2 have been normalized with $\sigma^{nml} = 10000$. The lower panel of Fig. 2.2 shows the complex refractive index.

2.3.2 Optical Properties in the BCS Theory of Superconductivity

The aspects of the microscopic theory of Bardeen Cooper and Schrieffer (BCS) of superconductivity, which are most prominent for the optical properties are: (1) The presence of a condensate of Cooper-pairs. A Cooper-pair behaves like a charged boson, with charge $2e$ and zero spin, and zero momentum, which is formed out of a pair of electrons or holes. (2) The presence of a gap Δ in the single particle excitation spectrum. The energy required to split a Cooper pair into two individual charge carriers corresponds to twice the value of the single particle gap i.e. 2Δ.

BCS theory is based on the concept of an effective attractive interaction between electrons which is mediated by phonons. This interaction is characterized by two parameters: (1) An attractive electron-electron interaction potential parametrized by the dimensionless constant λ, and (2) the energy range around the Fermi-level $\pm\hbar\omega_D$ where the attractive interaction is assumed to be non-zero. Originally ω_D was the Debye frequency of the phonon spectrum, but it can have a completely different physical interpretation for alternative microscopic models of the effective electron-electron interactions, not necessarily based on electron-phonon coupling.

Listed below are some important results of the BCS theory [7].

$$k_BT_c = 1.14\hbar\omega_D \exp\{-1/\lambda\} \tag{2.25}$$

$$2\Delta(0) = 3.52 k_BT_c \tag{2.26}$$

$$\frac{\Delta(T)}{\Delta(0)} \approx 1.74\left(1-\frac{T}{T_c}\right)^{\frac{1}{2}} \tag{2.27}$$

The following criterion is used to classify a superconductor as dirty or clean. The clean limit corresponds to having a mean free path of the electrons which is larger than the coherence length, which in BCS theory is roughly the Fermi velocity divided by the gap. The dirty limit then corresponds to having $2\Delta \ll \hbar/\tau$, where τ is the quasiparticle life time.

Mattis and Bardeen calculated the dynamical conductivity for a dirty superconductor, based upon the BCS theory. At $T = 0$ they obtained the following expressions for the real and imaginary parts of the conductivity, which are expressed in terms of the elliptic integrals K and E:

$$\begin{aligned}
\frac{\sigma_1(\omega)}{\sigma_0} &= 1+\tfrac{2\Delta}{\hbar\omega}E\left(\left|\tfrac{\hbar\omega-2\Delta}{\hbar\omega+2\Delta}\right|\right)-\tfrac{4\Delta}{\hbar\omega}K\left(\left|\tfrac{\hbar\omega-2\Delta}{\hbar\omega+2\Delta}\right|\right) && (\hbar\omega \geq 2\Delta)\\
&= 0 && (\hbar\omega < 2\Delta)\\
\frac{\sigma_2(\omega)}{\sigma_0} &= \tfrac{1}{2}\left(1+\tfrac{2\Delta}{\hbar\omega}\right)E\left(\left|\tfrac{\sqrt{8\hbar\omega\Delta}}{\hbar\omega+2\Delta}\right|\right)-\tfrac{1}{2}\left(1-\tfrac{2\Delta}{\hbar\omega}\right)K\left(\left|\tfrac{\sqrt{8\hbar\omega\Delta}}{\hbar\omega+2\Delta}\right|\right)
\end{aligned} \tag{2.28}$$

The penetration depth $\lambda(T)$ is calculated by considering the limiting behaviour of $\sigma_2(\omega)$ for small frequencies, and using the fact that $\lambda(T)^{-2} = \lim_{\omega\to 0} 4\pi\omega\sigma_2(T)/c^2$. The corresponding expressions in Mattis-Bardeen theory are for $\hbar\omega \ll 2\Delta$

$$\frac{\sigma_2(\omega)}{\sigma_0} = \frac{\pi\Delta}{\hbar\omega}\tanh\frac{\Delta}{2k_BT} \tag{2.29}$$

$$\frac{c^2}{\lambda(T)^2} = \frac{4\pi^2\Delta(T)}{\hbar}\sigma_0\tanh\frac{\Delta}{2k_BT} \tag{2.30}$$

An important consequence of Mattis-Bardeen theory is, that the difference in spectral weight between the superconducting and the normal state (the 'missing area') appears as a delta function at $\omega = 0$ [8]. This is a manifestation of the f-sum rule, and it serves as a consistency check on the Mattis-Bardeen theory. For an experimentalist it provides a way to estimate the penetration depth from

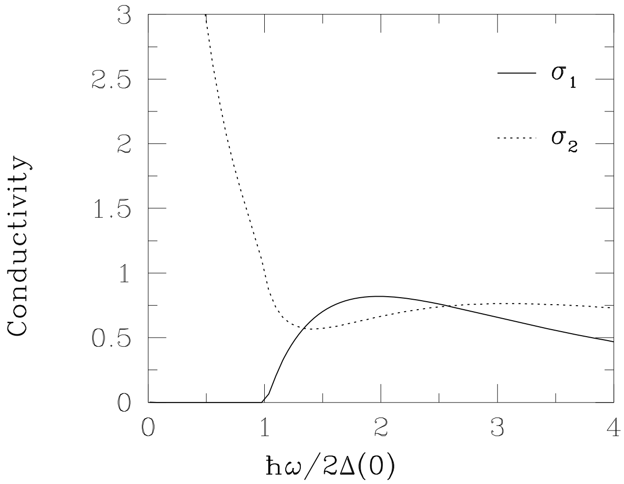

Figure 2.3: *Normalized conductivity versus frequency for a BCS superconductor for T<<T*$_c$*.* σ^{nml} *= 1700 and* 2Δ *= 83 cm*$^{-1}$*.*

the real part of the optical conductivity. This so-called Ferrel-Glover-Tinkham rule has the form

$$\frac{c^2}{\lambda(T)^2} = 8\int_{0^+}^{\infty}(\sigma_s(\omega,T) - \sigma_n(\omega,T))d\omega \tag{2.31}$$

where σ_s is the conductivity in the superconducting state, and σ_n is the conductivity in the normal state. Figure 2.3 shows the real and imaginary part of the conductivity for a dirty BCS superconductor. The model values used were $\mathrm{T}_c =$ 32K, $\omega_p = 6000$ cm^{-1}, $\gamma = 200$ cm^{-1} , T = 5 K , $2\Delta = 83$ cm^{-1} and $\epsilon_\infty = 4$. There are no electronic excitations below the gap value (σ_1 =0), but as soon as $\hbar\omega$ exceeds 2Δ, σ_1 rises steeply.

2.3.3 Local and Non-Local Electrodynamics

A metal is considered to be in the local regime of the electrodynamical response if the mean free path l is shorter than the penetration depth δ of the electromagnetic field. The non-local regime is defined by $l > \delta$. This means that the response of an electron to an externally applied field will depend upon it's history outside the layer of thickness $\simeq \delta$ below the surface.

Theoretically in a clean superconductor a local response to electromagnetic fields is expected when $\xi < \lambda_L$, where ξ is the coherence length. For a dirty superconductor the coherence length is modified according to the relation $1/\xi = 1/\xi_0 + 1/l$, where $\xi_0 = \hbar v_F/\pi\Delta$ is the coherence length in the clean limit. If $\xi > \lambda_L$ the dielectric response becomes non-local. This corresponds to the Pippard non-local regime. For a classical superconductor like aluminium $\lambda_L = 160\mathring{A}$, and $\xi_0 = 1.5\mu m$, which is clearly in the non-local regime. One of the consequences of a non-local dielectric response, is that the dielectric function has a significant dependence on the wave-vector k inside the solid, which complicates the analysis of the optical spectra.

For most HTSC $\lambda_L^{ab} > 1500\mathring{A}$, while $\xi_0 \approx 10\mathring{A}$, so they are in the extreme local regime. For electric fields along the c-axis this ratio is even larger. For example for $\mathrm{La}_{1.85}\mathrm{Sr}_{0.15}\mathrm{CuO}_4$ $\lambda_L^c \approx 5\mu m$, while $\xi_0 \approx 3\mathring{A}$. The fact that high T_c superconductors are well within the local regime of the electrodynamical response greatly facilitates the task of determining the optical parameters from reflectivity and/or transmittivity spectra.

2.3.4 Optical Conductivity of an s-wave Superconductor

Let us consider what happens in a superconductor for $T > 0$. As the temperature increases thermal fluctuations start gradually to break up Cooper pairs. This has three distinguishable effects on the optical conductivity: (1) The density of the superconducting condensate decreases leading to a larger value of the penetration depth. (2) The fragments of the broken Cooper-pairs correspond to unpaired quasiparticles, which become observable as a Drude-like peak centered at zero frequency. Note that this implies, that at a finite temperature, but still below T$_c$ *both* this quasi-Drude peak *and* the δ-function at zero frequency are present. (3) The presence of unpaired quasiparticles affects the self consistent gap equation of the BCS theory, and leads to a reduction of Δ, which eventually reaches $\Delta(T_c) = 0$ at the critical temperature.

Figure 2.4 shows the evolution of the conductivity σ_1 with temperature. The model parameters were given in section 2.3.2. As the temperature is increased from 5K, the gap begins to close and the peak centred at ω= 0 gains intensity and begins to broaden.

At T=30K (just below T$_c$) there is no longer a clear gap feature in σ_1, only a weak suppression of the conductivity.

The lower panel of Fig. 2.4 shows the evolution of the reflectivity with temperature. At T=5K there is a clear flat portion extending up to the gap energy where the reflectivity is one. Even at T=30K the reflectivity still shows a signature of superconductivity in that the low frequency behaviour is not Hagen-Rubens like, and shows a definite 'knee'. At T=5K and above the gap energy, the reflectivity undershoots the normal state reflectivity, again a mark of the material being in the superconducting state.

2.3.5 Optical Conductivity of a d-wave Superconductor

The mechanism engendering an attractive potential between two electrons and the symmetry of the pairing state may be investigated separately. This is fortunate as the pairing mechanism of the high T$_c$ superconductors has not been firmly established. All superconductors may be classified according to their symmetry properties. The order parameter Ψ transforms according to an irreducible representation of the symmetry group of the crystal [9]. A conventional superconductor has a pairing state with the full point group symmetry of the crystal. This is somewhat sloppily indicated as s-wave superconductivity (see fig. 2.5 (a, c)). By contrast in unconventional superconductors the pairing state has a lower symmetry than the point group symmetry of the crystal, *e.g.* d-wave symmetry (see fig. 2.5 (b, d)). The gap function Δ(k) for some of the possible pairing symmetries is shown in fig. 2.5 (b), (d). With optical spectroscopies the symmetry

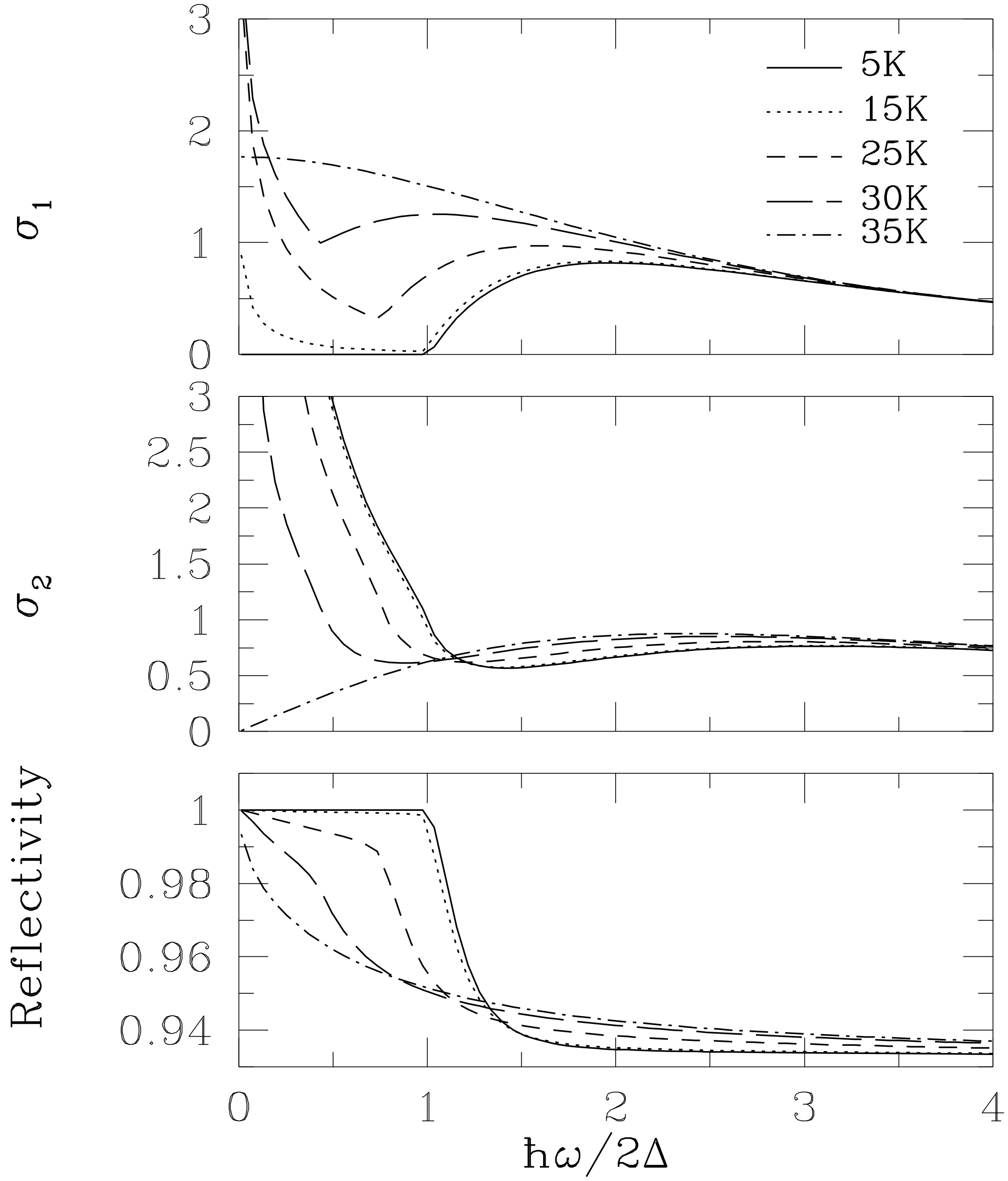

Figure 2.4: *Temperature dependence of the normalized conductivity and the reflectivity versus frequency for a BCS superconductor in the dirty limit. Model Parameters:* $T_c = 32$ *K*, $2\Delta = 83$ *cm*$^{-1}$, $\omega_p = 6000$ *cm*$^{-1}$ $\epsilon_\infty = 4$. *Normalizing value of the conductivity* $\sigma^{nml} = 1700$ $(\Omega cm)^{-1}$.

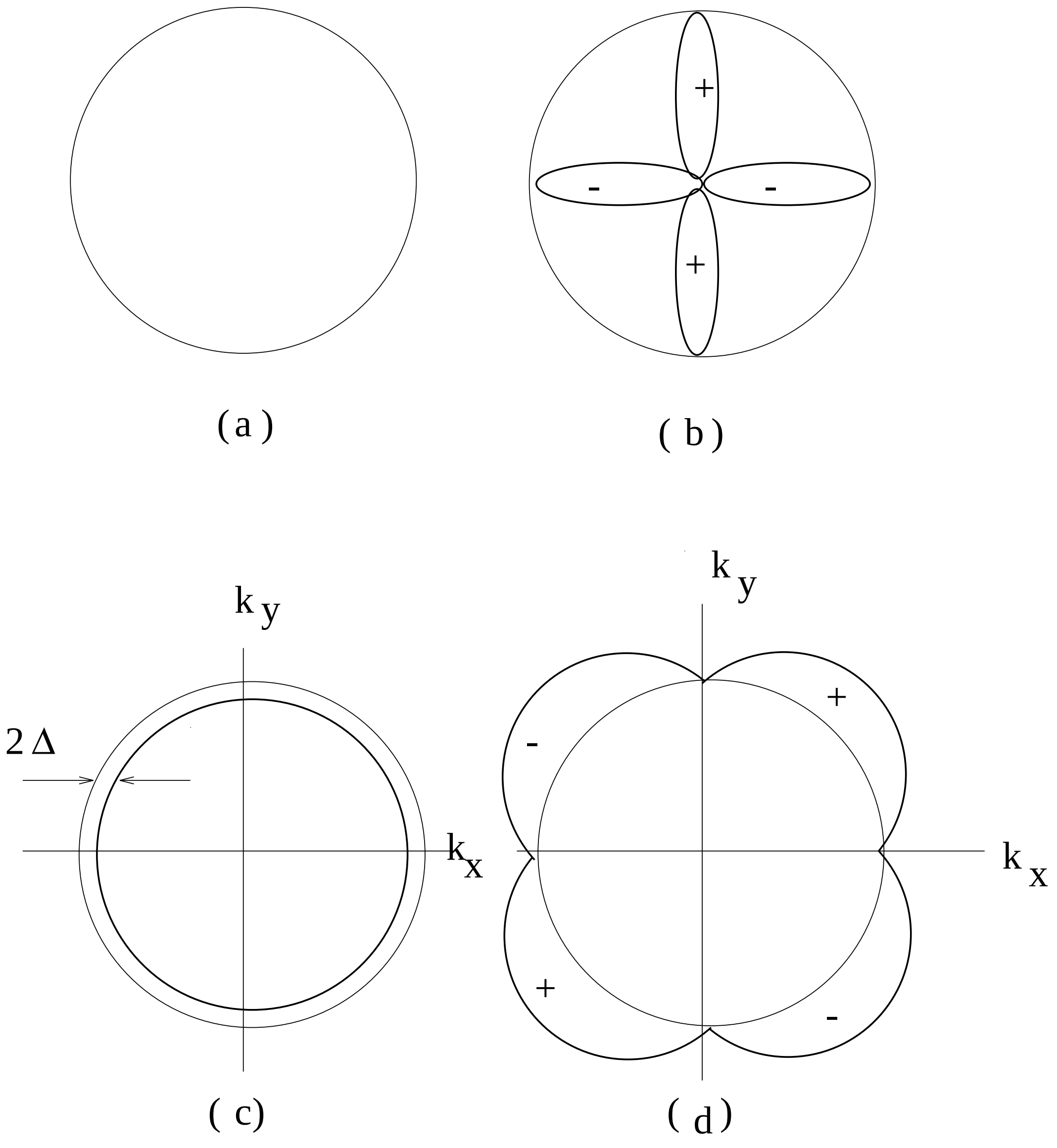

Figure 2.5: *Upper panel:Two singlet pairing states (a) s-wave (b) d-wave. Lower panel: k space plots of s-wave (a) and d-wave (b) order parameter /gap function.*

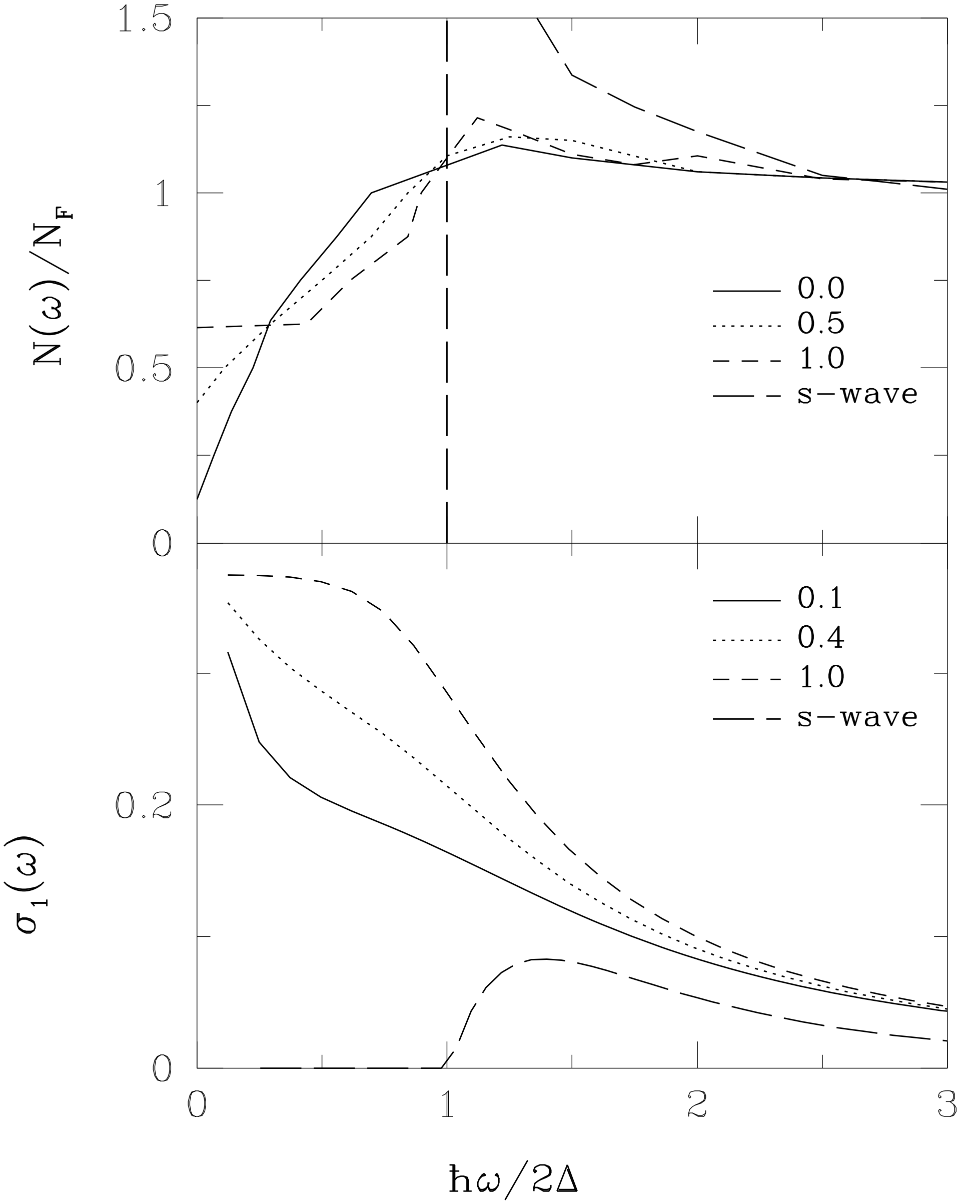

Figure 2.6: *Upper panel: normalized density of states N(ω) at T = 0K for a d-wave order parameter, as a function of frequency for various values of the impurity scattering cross section. Lower panel: Calculated optical conductivity for a s-wave and a d-wave superconductor as a function of frequency for various values of the impurity scattering cross section.*

properties of the pairing state can be accessed in two different ways: Either by investigating the frequency dependence of $\sigma_1(\omega)$ or by measuring the temperature dependence of the penetration depth $\lambda(T)$.

There is an accumulation of experimental evidence that the order parameter in the high T_c cuprates is unconventional, and has d-wave symmetry [10]. The upper panel of fig. 2.6 shows the density of states (DOS) for a d-wave superconductor as a function of frequency for various values of the scattering cross section σ. These spectra were calculated using the model of Graf *et al* [11]. For comparison we also display the calculation for an s-wave superconductor. Because there are nodes in the gap function, there is a finite DOS at ω=0, which increases as the scattering cross section increases. This translates into a finite conductivity at photon energies below the maximum gap value. As a result there is no real gap in the optical spectra, although there is still a suppression of the conductivity compared to the normal state. (see fig. 2.6 lower panel). The large difference in the optical conductivity for the two cases allows us to distinguish between a s-wave and a d-wave superconductor based upon infrared reflectivity measurements. This will be described in chapter 3 of this thesis. The apparent kinks in the DOS curves for a d-wave superconductor (see fig. 2.6 upper panel) is because only a few points were taken from the published article.

Units

Published FIR measurements usually use cm^{-1} as the unit of frequency. The unit of energy is either eV (electron-volt) or cm^{-1} ($E = \hbar\omega = hc/\ \lambda$). For practical convenience the same units are applied in this thesis. It is useful to note that
1 meV = 8.008 cm^{-1}, 1 cm^{-1} = 30 Ghz .

References

[1] J. D. Jackson, *Classical Electrodynamics* (J. Wiley, New York, 1975).

[2] D. van der Marel, H.-U. Habermeier, D. Heitmann, W. König, and A. Wittlin, Physica C **176**, 1 (1991).

[3] G. A. Thomas, J. Orenstein, D. H. Rapkine, M. Capizzi, A. J. Millis, R. N. Bhatt, L. F. Schneemeyer, and J. V. Waszczak, Phys. Rev. Lett. **61**, 1313 (1988).

[4] R. T. Collins, Z. Schlesinger, F. Holzberg, P. Chaudhari, and C. Feild, Phys. Rev. B **39**, 6571 (1989).

[5] Z. Schlesinger, R. T. Collins, F. Holzberg, c. Feild, G. Koren, and A. Gupta, Phys. Rev. B **41**, 11237 (1990).

[6] P. W. Anderson, Phys. Rev. B **55**, 11785 (1997).

[7] M. Tinkham, *Introduction to Superconductivity* (McGraw-Hill, New York, 1996).

[8] M. Tinkham and R. A. Ferrel, Phys. Rev. Lett. **2**, 33 (1959).

[9] J.Annett, N. Goldenfeld, and S. R. Renn, *Physical Properties of HTSC's, Volume 2 Ed. D. Ginsburg* (World Scientific, Singapore, 1990).

[10] J.Annett, N. Goldenfeld, and A. J. Leggett, *Physical Properties of HTSC's, Volume 5 Ed. D. Ginsburg* (World Scientific, Singapore, 1996).

[11] M. J. Graf, M. Palumbo, D. Rainer, and J. A. Sauls, Phys. Rev. B. **52**, 10588 (1995).

3

ab Plane Electrodynamics of $La_{2-x}Sr_xCuO_4$

In this chapter the first Polarized Angle Resolved Infrared Spectroscopy (PARIS) measurements are presented on a classical superconductor NbN (T_c = 16K) and on the HTSC $La_{1.85}Sr_{0.15}CuO_4$ (T_c = 32K). The optical conductivity for NbN showed a BCS gap of 6 meV which agrees with transmission measurements and published data. These results verified the technique. The ab-plane optical conductivity of $La_{1.85}Sr_{0.15}CuO_4$ showed a reduction in $\sigma_1(\omega)$ below 20 meV. The observed frequency dependence excludes an isotropic s-wave order parameter but agrees reasonably well with model calculations assuming a d-wave order parameter. This set of measurements is hereafter referred to as series 1.

The second set of measurements (hereafter referred to as series 2) using the PARIS technique were performed on $La_{1.8}Sr_{0.20}CuO_4$ (overdoped, T_c = 29K). The aim was to compare how the quasiparticle excitation spectrum evolved in the normal and superconducting state, in going from the optimally to the overdoped case. Results show that the optical conductivity $\sigma_1(\omega)$ for the overdoped sample has a sharper Drude peak and that there is a reduction in the spectral weight in the FIR region. The effective number of charge carriers N_{eff} is reduced when compared to the optimally doped sample. Close to T_c, the overdoped sample has a larger value of penetration depth λ_L and there is a reduction in the superfluid fraction. [1]

---

[1] Parts of this chapter have published in Phys. Rev. Lett. 76, 1525, 1996 and orally presented at the Low Energy Electrodynamics in Solids (LEES) Conference, Ascona, Switzerland, July 1997.

3.1 Series 1: PARIS of $La_{1.85}Sr_{0.15}CuO_4$ and NbN

An introduction to the reasoning behind and the advantages of the PARIS technique are given in the ensuing reprinted article. As explained in the article the results presented in this section were obtained using the absolute reflectivity of the sample at normal incidence which was then used to calculate the reflectivity at 80°. The reference used to obtain the absolute reflectivity was a gold mirror which had been evaporated on a silicon substrate. The method used to obtain the optical conductivity is described section 3.2.2. The measurements and results obtained using this methodology are referred to as series 1.

One year later an *in-situ* gold evaporator was installed which eliminated the need for a gold mirror and allowed the absolute reflectivity of the sample to be determined at each temperature. The sample holder was changed to a cone shape (see Fig. 3.4) which reduced the background noise. Furthermore the data analysis was improved. This is described in section 3.2.3. PARIS measurements were performed on a single crystal of $La_{1.85}Sr_{0.15}CuO_4$ (optimally doped, T_c = 32K) and $La_{1.8}Sr_{0.20}CuO_4$ (overdoped, T_c = 29K). These are referred to as series 2 measurements. Because of the difference in experimental technique and the calculation of the conductivity, series 1 and 2 have not been combined.

In order to use the PARIS technique and to probe the ab-plane properties, the crystal must be cut with the a-c axes in-plane, as shown in Fig. 3.1. Using p-polarized light only the ab-plane which is isotropic is probed. With s-polarized light the c-axis is probed and the results of these measurements for the overdoped sample are presented in chapter 4.

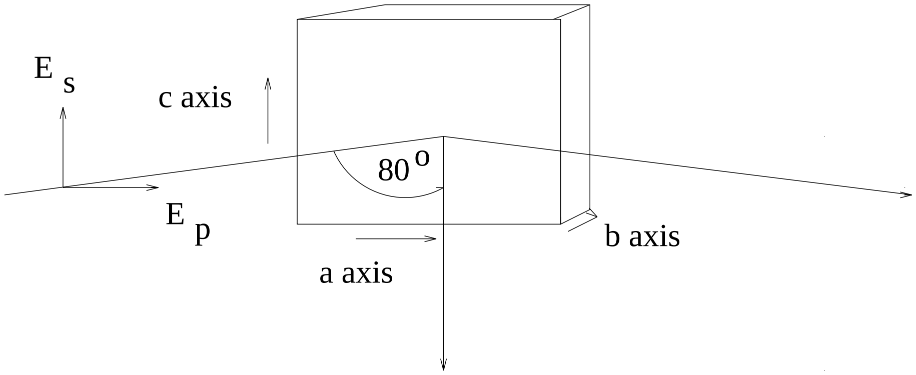

Figure 3.1: *Crystal geometry used for p- and s-polarized measurements. E denotes the electric field vector.*

3.2 Limitations of the Kramers-Kronig Relations

3.2.1 Reflectivity at Large Angles

The method for calculating the real and imaginary parts of the dielectric function $\epsilon(\omega)$ from the reflectivity measurements was described in chapter 2. Quite generally, the approach is to use the fact that $\ln r(\omega) = \ln(|r(\omega)|) + i\phi(\omega)$, where $|r(\omega)|$ is the square root of the absolute reflectivity, which is the experimentally measured quantity, while $\phi(\omega)$ is the phase of the reflection coefficient. Kramers-Kronig relations should exist between $ln|r(\omega)|$ and $\phi(\omega)$:

$$\phi(\omega) = \frac{-2\omega}{\pi} P \int_0^\infty \frac{\ln|r(\omega_1)| - \ln|r(\omega)|\, d\omega_1}{\omega_1^2 - \omega^2} \tag{3.1}$$

where P is the principal part of the integral. The above integral can be evaluated provided that $\ln r(\omega)$ is a causal response function. This requires that $\ln r(\omega)$ has all it's poles in the lower half of the complex frequency plane and it should converge sufficiently rapidly for $|\omega| \to \infty$. In order to check whether or not these conditions are fulfilled, let us examine the Fresnel equation for the reflectivity of p-polarized light

$$r_p = \frac{n^2 \cos\theta - \sqrt{n^2 - \sin^2\theta}}{n^2 \cos\theta + \sqrt{n^2 - \sin^2\theta}} \tag{3.2}$$

where n is the refractive index($n^2 = \epsilon$). n^2 Is a causal response function, it has it's poles confined to the lower half of the complex frequency plane, and $\mathrm{Im} n^2 > 0$. The logarithm of the reflectivity $\ln r(\omega)$ has singularities for $r(\omega) \to 0$, which occurs when :

$$n^4(\omega)\cos^2\theta = n^2(\omega) - \sin^2\theta \tag{3.3}$$

The roots of this equation are

$$\begin{array}{rcl} n^2(\omega) & = & 1 \\ n^2(\omega) & = & \tan\theta \end{array} \tag{3.4}$$

Substituting these conditions into the standard Drude equation for the dielectric function

$$\epsilon = \epsilon_\infty - \frac{\omega_p^2}{\omega(\omega + i\gamma)} \tag{3.5}$$

one obtains singularities of the function $\ln r(\omega)$ at the following set of frequencies in the complex frequency plane

$$\omega = -\frac{i\gamma}{2} \pm \sqrt{\frac{\omega_p^2}{\epsilon_\infty - \tan^2\theta} - \frac{\gamma^2}{4}} \tag{3.6}$$

$$\omega = -\frac{i\gamma}{2} \pm \sqrt{\frac{\omega_p^2}{\epsilon_\infty - 1} - \frac{\gamma^2}{4}} \tag{3.7}$$

If $\tan^2\theta < \epsilon_\infty$, all singularities are in the lower half of the complex frequency plane (see Fig. 3.2). However, if $\tan^2\theta > \epsilon_\infty$, singularities occur both in the upper and the lower half of the complex frequency plane (see Fig. 3.2). As a result no Kramers-Kronig relations exist between $ln|r(\omega)|$ and $\phi(\omega)$ in this case. The table below lists the maximum angle of incidence θ_{max} for a given value of ϵ_∞ below which Kramers-Kronig relations still exist.

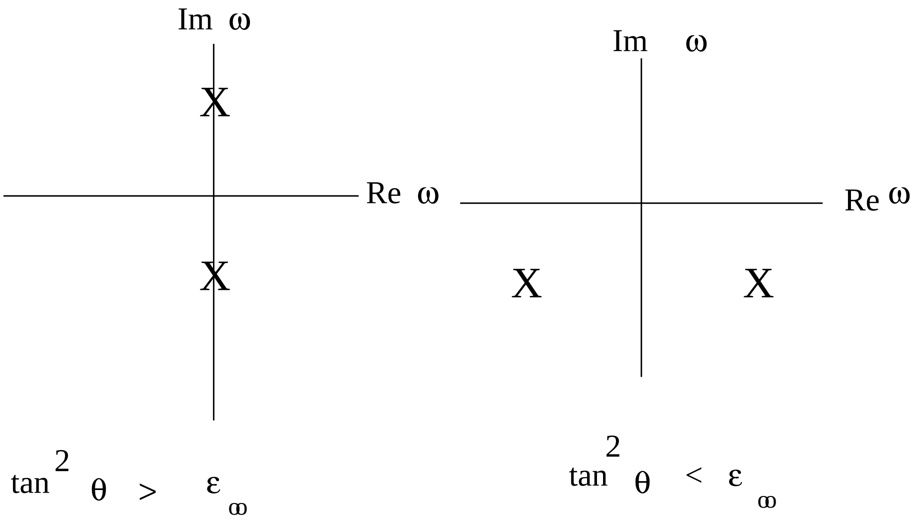

Figure 3.2: *Position of poles and their dependence upon θ and ϵ_∞.*

ϵ_∞	θ_{max}
1.0	45°
1.5	50°
4	63°
44	81°

Clearly, if $\epsilon_\infty = 1$ and $\theta > 45°$, the phase cannot be calculated from the reflectivity spectrum using conventional Kramers-Kronig relations. Of course the optical response expressed by the dielectric function is still a causal response function, and has poles only in the lower half of the complex frequency plane. Therefore one possible approach, which should provide physically sound results, is to make a a multi-oscillator least squares fit to the reflectivity spectrum. Such a fit provides the real and imaginary part of $\epsilon(\omega)$, and the method is in principle just as good as a Kramers-Kronig analysis. In practice it is a very time consuming task to obtain a good fit to all the fine details of a reflectivity spectrum. Also a fit procedure invariably results in an uncontrolled and undesirable smoothing of the data. The dielectric function ϵ was calculated according to the procedure described in section 3.2.2. A second numerical procedure was developed for calculating ϵ for series 2 measurements, this is described in section 3.2.3.

3.2.2 Data Analysis For Series 1 Measurements

The first approach for calculating the dielectric function was based on the observations that: (1) For an angle of incidence of $\theta = 80^\circ$ no poles occur in the upper half plane provided that $\epsilon_\infty > 44$. (2) In a metallic spectrum the reflectivity at low frequencies becomes insensitive to the value of ϵ_∞. Hence the reflectivity spectra, and the ratio's between spectra taken at different temperatures, should not change much if the actual dielectric function is incremented with a frequency independent constant $\Delta\epsilon \approx 40$.

As ϵ is not a directly measured number, we had to apply an indirect solution. The idea is that ϵ can be calculated directly from normal incidence spectra, but with limited accuracy compared to grazing incidence reflection. We combined the best of both techniques by using reflectivity *ratios* measured at grazing incidence, which is a highly accurate way to detect small changes in reflectivity of the sample. In addition we measure the reflectivity for $\theta = 0^\circ$ at one of these temperatures. This permits us to calculate $\epsilon(\omega)$ at this temperature using conventional Kramers-Kronig analysis. We first add a sufficiently large number to the dielectric constant, resulting in $\tilde{\epsilon} = \Delta\epsilon + \epsilon$ (where $\Delta\epsilon = 40$). Using $\tilde{\epsilon}(\omega)$ we calculate the absolute value of the reflectivity at grazing incidence for this particular temperature. For low frequencies ϵ diverges, hence $\Delta\epsilon \ll |\epsilon|$, and the procedure of adding $\Delta\epsilon$ to ϵ has a negligible effect on the reflectivity. Yet it removes the unwanted singularities of $\ln r(\omega)$ in the upper half of the frequency plane. Next we multiply this reflectivity function with the grazing incidence reflection ratios for each temperature. We then use standard Kramers-Kronig relations to calculate the phase of the grazing pseudo-reflectivity, thus providing the pseudo dielectric function $\tilde{\epsilon}$. The last step is to subtract $\Delta\epsilon$ from the pseudo dielectric function, to obtain ϵ.

The advantage of this method is that the experimental reflectivity ratios can be measured very accurately. Hence the numerical analysis explained above is an accurate measure of relative changes of $\sigma(\omega)$ as a function of temperature. The accuracy is a factor $1/\cos\theta$ higher than what could be obtained with normal incidence reflection measurements. On the other hand, the absolute values of $\sigma(\omega)$ are still limited by the accuracy of the normal incidence experiment at the reference temperature.

Our reflectivity measurements at $\theta = 80^\circ$ were performed within a temperature range of 4 to 60K. With a gold reference mirror we checked that the thermal expansion effects within this temperature range were negligible. The absolute normal incidence reflectivity was measured at T=40K (see reprinted PRL paper, Fig. 1, upper panel, inset), then the dielectric function was calculated using the Kramers-Kronig transformation. The procedure is summarized in the flow diagram 1. I^S denotes the intensity of the signal reflected from the sample. R denotes the absolute reflectivity using a gold mirror as a reference (I^S/I^{Au}). The superscript p denotes p-polarized light.

Measure I_T^p for 4K $<$ T $<$ 40K, $\theta = 80^\circ$

↓

Take Ratio's: I_T^p/I_{40K}^p

↓

Measure Absolute Reflectivity $\mathrm{R}_{40K}^{\theta=0}$

↓

Kramers-Kronig of $\mathrm{R}_{40K}^{\theta=0}$: Calculate $\epsilon(40K)$

↓

$\tilde{\epsilon} = \epsilon + 40$

↓

Calculate Reflectivity at T=40K for $\theta = 80^\circ$: $\tilde{R}_{40K}^{80^\circ}$

↓

Calculate $\tilde{R}_T^{80^\circ} = I_T^p/I_{40K}^p \times \tilde{R}_{40K}^{80^\circ}$

↓

Kramers-Kronig gives pseudo dielectric function at temperature T: $\tilde{\epsilon}(T)$

↓

Subtract Shift: $\epsilon(T) = \tilde{\epsilon}(T) - 40$

↓

Recalculate I_T^p/I_{40K}^p using $\epsilon(T)$ and compare with measured value

Flow diagram 1: Methodology for calculating the dielectric function for series 1 measurements.

3.2.3 Data Analysis For Series 2 Measurements

After completing the procedure outlined above, the recalculated reflectivity (last line in the flow diagram) was compared with the measured reflectivity ratios. As expected the spectra match very well at low frequencies. Differences become noticeable above 700 cm^{-1}. For the series 2 measurements on this particular crystal, another procedure was adopted which eliminated this error. The method is outlined in the following subsection. The result is displayed in Fig. 3.3, showing good agreement between the two methods for frequencies lower than 700cm^{-1}.

Fit Measured Reflectivity $|r^{exp}|^2$ at each Temperature: $|r^{fit}|^2$
↓
Fitted sum of Oscillators provides: $\epsilon = \epsilon_1 + i\epsilon_2$
↓
Shift ϵ: $\tilde{\epsilon} = \epsilon + \Delta\epsilon$
↓
Calculate Reflectivity at $\theta = 80^\circ$: $|r^{shifted}|$
↓
Use $b(\omega) \equiv \ln(r^{fit}/r^{shifted})$
To calculate: $\ln|\tilde{r}| = \ln|r^{exp}| - \text{Re}b(\omega)$
(Poles in the upper half plane are now compensated)
↓
Use Kramers-Kronig to calculate $\tilde{\phi}(\omega)$ from $\ln|\tilde{r}(\omega)|$
↓
Calculate dielectric function $\tilde{\epsilon}(\omega)$ from $\tilde{r}(\omega)$
↓
Subtract Shift: $\epsilon(\omega) = \tilde{\epsilon}(\omega) - \Delta\epsilon$
↓
Recalculate Reflectivity and compare with $|r^{exp}|^2$

Flow diagram 2 : Methodology for calculating dielectric function for series 2 measurements.

One year after the series 1 measurements were performed the experimental arrangement was improved by including an *in-situ* gold evaporator, so that the absolute reflectivity at each temperature could be obtained.

In the second approach we constructed a function $b(\omega)$ such that $\ln\tilde{r}(\omega) = \ln r(\omega) - b(\omega)$ has no singularities in the upper half of the complex frequency plane [1]. This requires knowledge of a function $b(\omega)$ which should precisely compensate the undesired poles of $r(\omega)$ in the upper half of the complex frequency plane. We can then perform a Kramers-Kronig transformation on $\ln|\tilde{r}(\omega)|$ to obtain the phase, and recalculate $\ln r(\omega)$ by adding $\ln\tilde{r}(\omega) + b(\omega)$, which completes the procedure. A simple check as to the accuracy of the procedure is to use the resulting complex dielectric function $\epsilon(\omega)$ to calculate the spectral function $|r(\omega)|$ and compare this to the experimental value used as the input of the numerical procedure.

This procedure has the advantage that it is accurate up to 6000 cm^{-1}. Referring to flow diagram 2, for each temperature the reflectivity is fitted using a series of Lorentzian oscillators. This fit does not yet contain the fine details of the spectrum, including experimental noise. The next step is to recalculate the reflectivity curve, after adding $\Delta\epsilon$ to ϵ ($\tilde{\epsilon} = \epsilon + \Delta\epsilon$ with $\Delta\epsilon = 40$). This is referred to as $|r^{shifted}|^2$ in the flow diagram. The curve $|r^{shifted}|^2$ has no poles in the upper half of the complex frequency plane, as explained in subsection 3.2.1. The next step is to calculate

$$\tilde{r}(\omega) = r^{shifted} \times \frac{r^{exp}}{r^{fit}} \tag{3.8}$$

This corresponds to the experimental reflectivity including all the fine details and

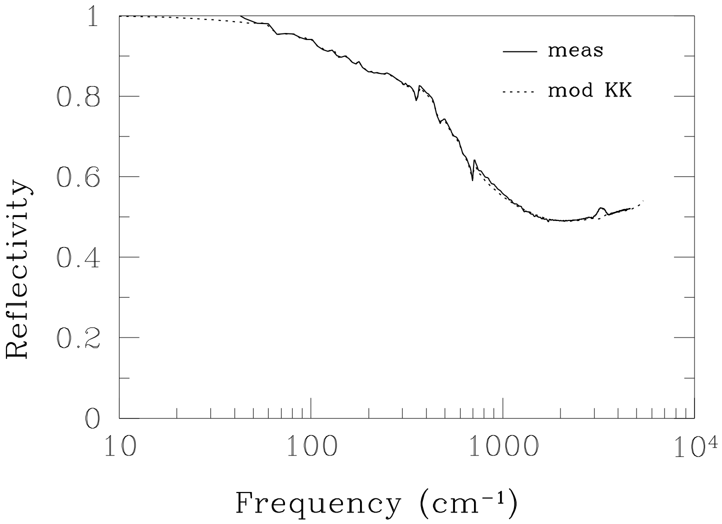

Figure 3.3: *Comparison of measured reflectivity with the result of modified Kramers-Kronig for* $La_{1.85}Sr_{0.15}CuO_4$ *at T=4K.*

the reflectivity curve with no poles in the upper half of the complex frequency plane. By performing a Kramers-Kronig transform on $\ln|\tilde{r}(\omega)|$, the phase $\tilde{\phi}(\omega)$ is obtained, and from these two we calculate $\tilde{\epsilon}$. To obtain the actual dielectric function $\Delta\epsilon$ must still be subtracted.

As an accuracy check the final values of ϵ_1 and ϵ_2 are then used to calculate the reflectivity, which is then compared to the measured reflectivity. The results are shown in Fig. 3.3. We see that the analysis is internally consistent for the complete frequency range measured.

3.3 Series 2: Comparison of Optimally and Overdoped Crystals

In this second series of measurements a comparison is made between the optical excitation spectrum $\sigma_1(\omega)$ of an optimally doped crystal of $La_{1.85}Sr_{0.15}CuO_4$ (T_c = 32K) and an overdoped crystal of $La_{1.8}Sr_{0.20}CuO_4$ (T_c = 29K). There have not been any published low temperature (below T_c) reflectivity measurements in the far infrared region for an overdoped crystal of the lanthanum compound. It is of interest to determine how the spectral weight evolves as the number of holes increases and to try and shed light as to why the critical temperature T_c decreases. Resistivity measurements show that for the overdoped sample (Sr=0.2), the resistivity ρ decreases [2] i.e., the material becomes more metallic. Therefore the changes in the reflectivity, caused by going from the normal to the superconducting state, are expected to be even smaller than in the optimally doped case. This is a severe test of the PARIS technique and the experimental arrangement.

3.3.1 Experimental Procedure

The previous measurements (series 1) described in section 3.1 were performed using a knife edge 500 μm above the sample to limit the distribution of angles of incidence of the incoming beam and to reduce the background black body radiation reaching the detector. In the following series of measurements the procedure was improved such that the sample was mounted on top of a copper cone. Consequently any light from the source not reflected from the sample does not reach the detector(see lower panel of Fig. 3.4). This arrangement made the knife edge unnecessary. The second improvement was the installation of an *in-situ* gold evaporator which meant that the absolute reflectivity at each temperature was obtained.

The cryostat was modified to include a tungsten coil for evaporating the gold. The measurement procedure was to measure the sample between 4 and 300K, evaporate an Au film at 300K and re-measure the Au coated sample at each temperature. This resulted in a measurement of the absolute reflectivity at each temperature. This approach has the advantage over the method used for series 1, in that errors in the reference spectra at 40K are not propagated to the spectra at other temperatures. The advantage of *in-situ* Au evaporation becomes self evident when the sample consists of small crystal platelets from which a mosaic is made (see chapter 5). Then, in order to obtain the absolute reflectivity there is no alternative to *in-situ* Au evaporation. The corners and the irregular shapes of the platelets produce a diffraction pattern, which will only cancel upon division by a reference, if the reference has exactly the same geometry. That is, the original mosaic, but Au coated. Fig. 3.4 shows the experimental arrangement within the cryostat and the sample holder. In the grazing incidence geometry the two windows used to isolate the cryostat from the Bruker FFT spectrometer are diametrically opposite. Therefore, the window directly opposite the sample is free and was used to mount the Au evaporator. This arrangement has the advantage that the sample does not need to be rotated or moved for Au evaporation, and so no errors are introduced. For normal incidence measurements, the sample would have to be rotated by 180° for Au coating and then returned to it's original position which may introduce errors.

Au Evaporation Procedure

The sample was measured between 4 and 300K, and then held at 300K by the cryostat heater. The tungsten coil was slowly heated in steps of 1 Amp up to 6 Amps to allow for degassing. All the degassed species adhered to the radiation shield which was at $\approx$ 100K. The spectrometer was in alignment storage mode and so showed the reflectivity of the sample. This was a means of monitoring when Au deposition began and when it should be stopped. After a lengthy degassing period, the Au was evaporated at about 7.5 Amps, the rate being kept deliberately low in order to obtain a mirror like surface deposition. During the sample measurements, Au evaporation, and subsequent Au coated sample measurements, the cryostat was continuously pumped by the turbo pump. Whilst below 77K this was not necessary (due to the cryo-pumping by the cold finger), above this temperature various species are degassed and would otherwise adhere to the sample surface. The Au film thickness was $\approx$ 300 nm which is much larger than the skin depth δ.

Correction of Au Reflectivity

Whilst the reflectivity of an Au film at normal incidence is 99.5%, at grazing incidence this small deviation from 100% is amplified. This effect was simulated using a simple Drude model for Au and the Fresnel equation. The nominal plasma frequency ω_p of gold is 66,000 cm^{-1} with γ =300 cm^{-1} at 300K [3]. However, due to d-band transitions, the reflectivity is drastically reduced above 2 eV (yellow has a wavelength of 0.57 μm) giving an effective plasma frequency of 16,000 cm^{-1}. The same process occurs in silver [4]. The dependence of the reflectivity on the angle of incidence was calculated. Resistivity measurements

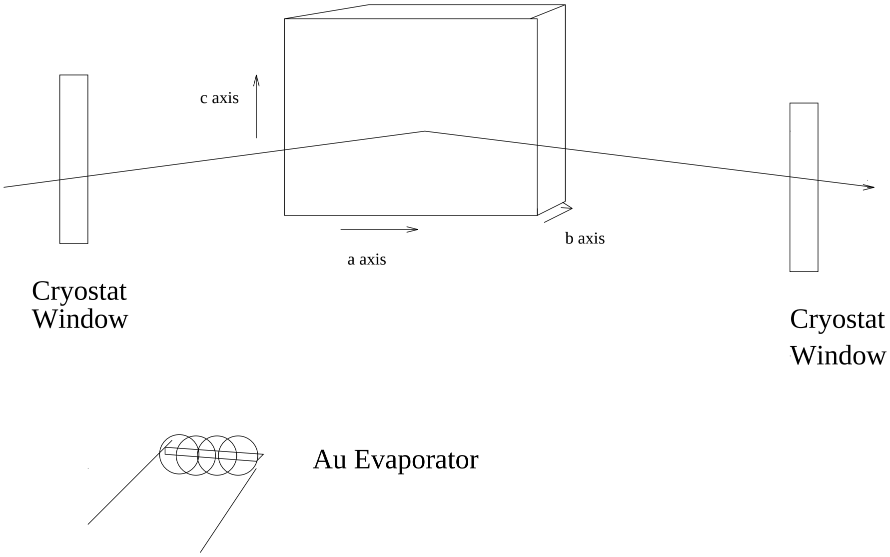

Experimental Arrangement using in-situ Au Evaporation

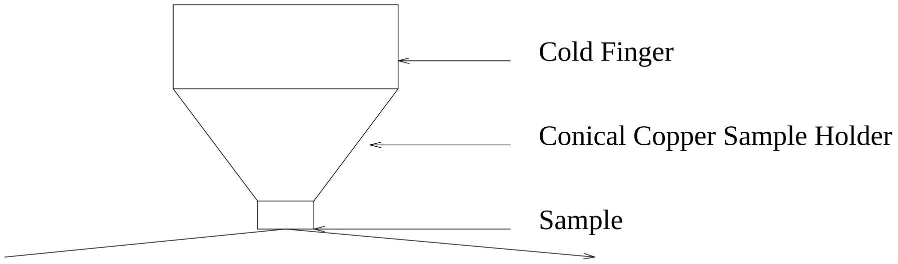

Sample Holder

Figure 3.4: *Experimental Arrangement using in-situ Au Evaporator and Sample Holder.*

of Au show a linear temperature dependence [3] down to 40K, below which the resistivity saturates. Therefore only measurements above 40K were corrected for the temperature dependent scattering rate.

The effect was also verified by comparing the reflectivity of an Au film with that of a polished single crystal of silver(Ag). When the Au film is deposited, because it is amorphous, voids are formed within the film which reduces the value of ϵ [5]. The relative strength of this effect depends on the concentration of voids which in turn depends upon the quality of the vacuum, rate of deposition, coil geometry, i.e. the spacing between the coils and the coil temperature. Typical void values are between 10 and 20 %.

3.3.2 Results and Discussion

Optical Conductivity

The measured reflectivity of $La_{1.85}Sr_{0.15}CuO_4$ (optimally doped) and $La_{1.8}Sr_{0.20}CuO_4$ (overdoped) is shown in Fig. 3.5. The overdoped sample shows less temperature dependence than the optimally doped crystal. For the overdoped sample, the changes in reflectivity in going from the superconducting to the normal state i.e. from 4K to 40K, in the frequency range of 50 - 200 cm^{-1}, are very small. Had these measurements been performed at a near normal angle of incidence, the changes would have fallen within the measurement noise. The optical conductivity for $La_{1.85}Sr_{0.15}CuO_4$ and $La_{1.8}Sr_{0.20}CuO_4$, calculated using the modified Kramers-Kronig analysis which was explained in section 3.2.3, is shown in Fig. 3.6 (up to 400 cm^{-1}) and in Fig. 3.7 (up to 6000 cm^{-1}). The conductivity for both samples falls off more slowly than the expected Drude model value of $1/\omega^2$. Considering the upper panel of Fig. 3.6, between the temperatures of 4K and 40K, one observes a gradual increase in the spectral weight as the temperature is increased. This increase is due to the increase in the density of quasiparticles. These quasiparticles are made up from the unpaired electrons. Depending upon the value of the gap, Cooper pairs can be broken up into quasiparticles by an excitation energy $\hbar\omega$. In an s-wave superconductor quasiparticles are created only if the excitation energy exceeds the gap value i.e., $\hbar\omega > 2\Delta$. In a d-wave superconductor quasiparticles are created for $\hbar\omega > 0$ because of the existence of nodes in the gap function.

Experimentally we observe no clearly defined gap, even at 4K, which is far below T_c. Also the superconducting induced changes are not limited to the weak coupling BCS gap value of 82 cm^{-1} ($2\Delta/k_BT_c$ =3.5), but extend up to 300 cm^{-1}. This implies either that the material is in the strong coupling limit or that the normal state and the superconducting state cannot be described by the Landau Fermi Liquid model which is the basis of the BCS theory. The lower panel of

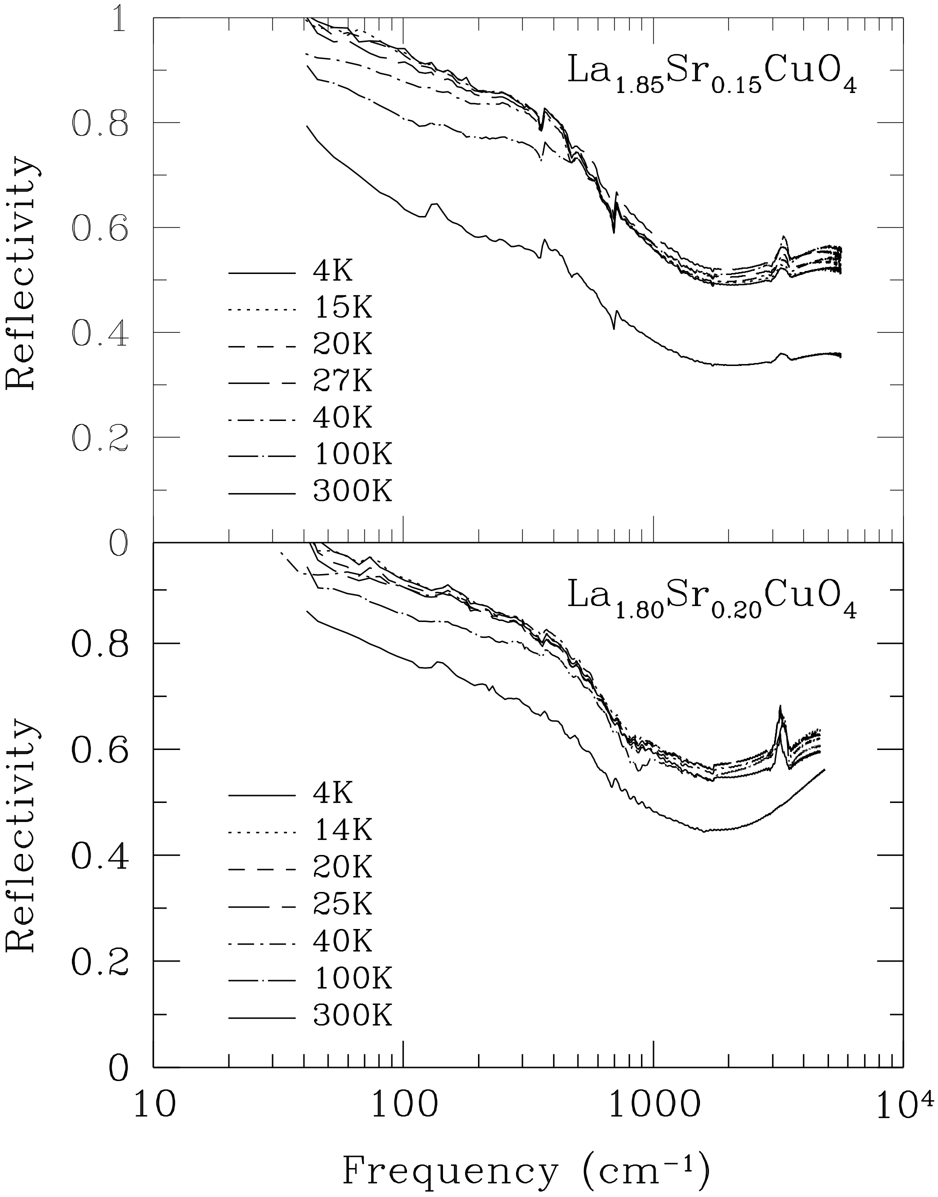

Figure 3.5: *Reflectivity of* $La_{1.85}Sr_{0.15}CuO_4$ *and* $La_{1.8}Sr_{0.20}CuO_4$ *using in-situ gold evaporation.*

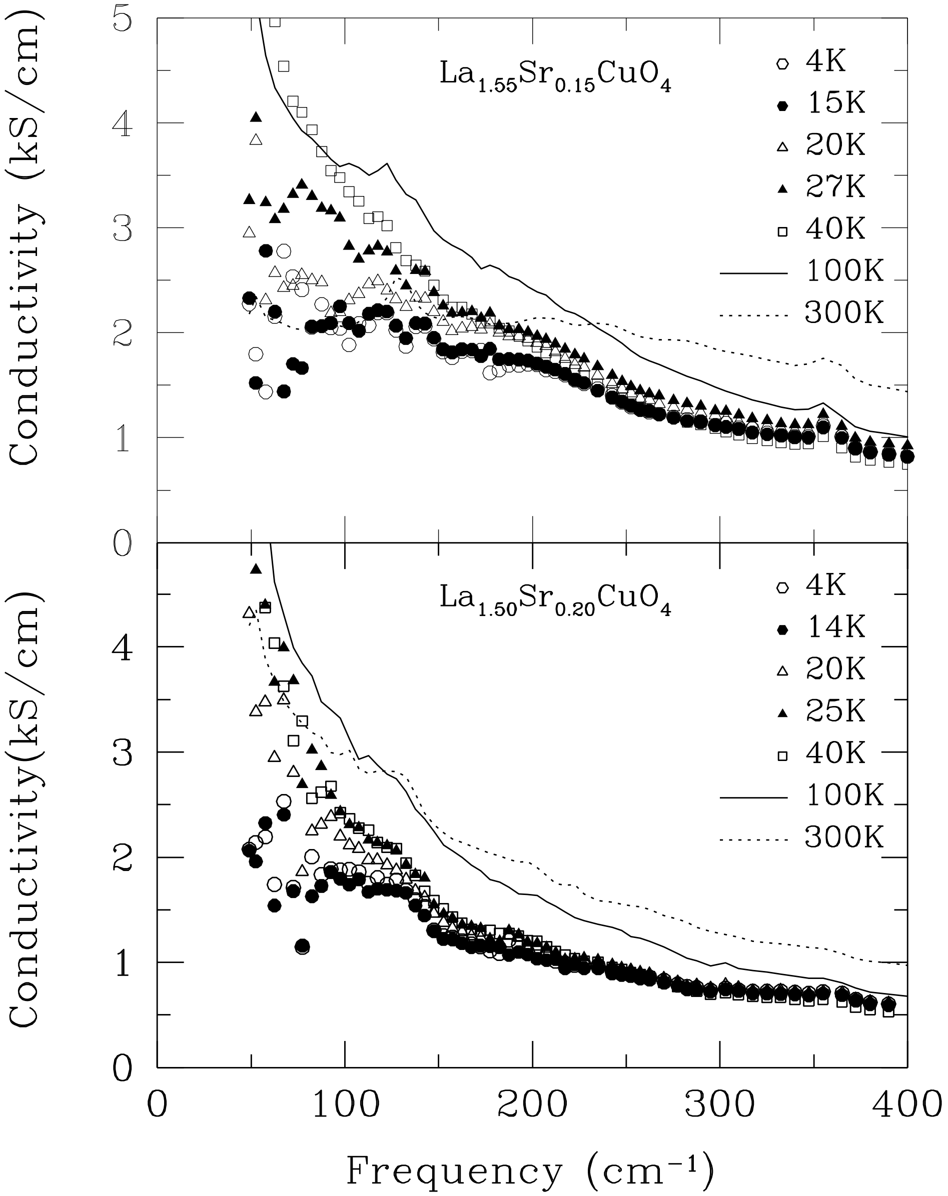

Figure 3.6: *Optical conductivity of* $La_{1.85}Sr_{0.15}CuO_4$ *and* $La_{1.8}Sr_{0.20}CuO_4$.

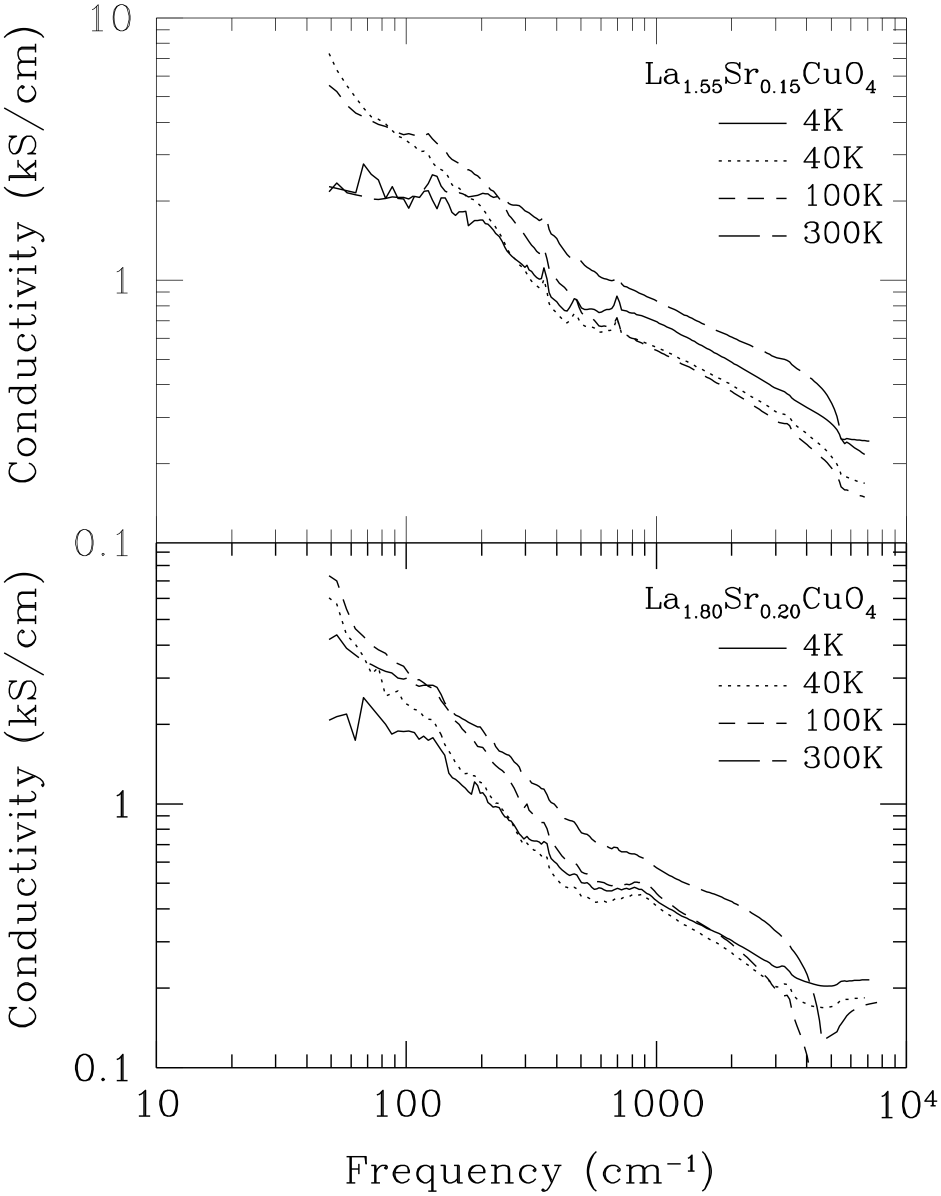

Figure 3.7: *Optical conductivity $\sigma_1(\omega)$ in MIR range.*

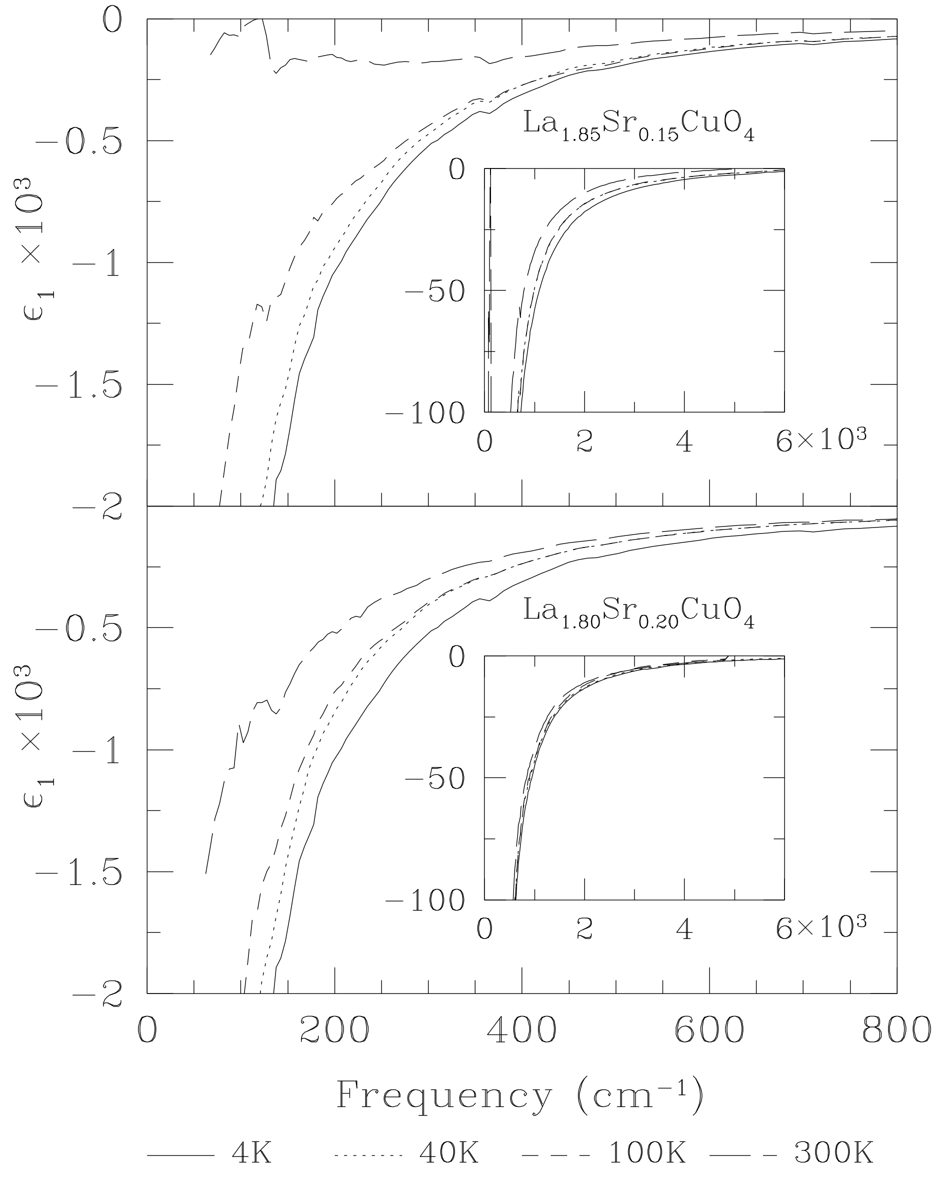

Figure 3.8: *Real part of the dielectric function* ϵ_1 *versus frequency for* $La_{1.85}Sr_{0.15}CuO_4$ *and* $La_{1.8}Sr_{0.20}CuO_4$.

Fig. 3.6 shows the optical conductivity for the overdoped sample $\mathrm{La_{1.8}Sr_{0.20}CuO_4}$. The range of superconducting induced changes extends up to 150 cm^{-1} which is a reduction by a factor of 2 when compared to the optimally doped sample. This is surprising as the critical temperature changes from 32K (optimally doped) to 29K (overdoped), which is a decrease of only 3K. The shift of spectral weight into the delta function at zero frequency is also smaller for the overdoped sample.
Fig. 3.8 shows the real part of the dielectric function $\epsilon_1(\omega)$, for both the optimally and the overdoped sample. $\epsilon_1(\omega)$ Corresponds to the imaginary(inductive) part of the conductivity i.e. $\epsilon_1 \propto \sigma_2/\omega$. The inset shows ϵ_1 over the full frequency range measured. The overdoped sample shows very little temperature dependence between 4 and 300K for frequencies greater than 800 cm^{-1}. The optimally doped sample shows a significant change at 300K in the FIR region. At a temperature of 4K, both samples show a $1/\omega^2$ behaviour as described in the two fluid model [6]:

$$\epsilon(\omega) = \epsilon_\infty\left(1 - \frac{\omega_{ps}^2}{\omega^2} - \frac{\omega_p^2 - \omega_{ps}^2}{\omega(\omega + i\gamma)}\right) \tag{3.9}$$

Table 3.1 shows the scattering rate $\gamma(0)$ obtained from the low frequency limiting behaviour of the measured reflectivity. The table shows the resulting values for $\mathrm{La_{1.85}Sr_{0.15}CuO_4}$ and $\mathrm{La_{1.8}Sr_{0.20}CuO_4}$. The scattering rate for the overdoped sample is slightly smaller than that for the optimally doped sample i.e., it is more 'like a metal'. The difference at a temperature of 300K is a factor of 2. This can be traced back to Fig. 3.6: the overdoped sample has a conductivity shape that is 'Drude like ' whilst that of the optimally doped sample is very broad and flat. This results in a larger scattering rate. This feature also shows itself in the value of the zero frequency conductivity $\sigma(0)$ shown in table 3.2: $\sigma(0) =$ 2.2 kS/cm ($\mathrm{La_{1.85}Sr_{0.15}CuO_4}$) whilst for the overdoped sample $\sigma(0) = 4.2$ kS/cm ($\mathrm{La_{1.8}Sr_{0.20}CuO_4}$). Table 3.1 also shows the frequency dependent scattering rate $\gamma(\omega)$ (see Fig. 3.10) taken around 90 cm^{-1}, which is close to the BCS gap value. Clearly $\gamma(90cm^{-1})$ is slightly larger than $\gamma(0)$.

	$\mathrm{La_{1.85}Sr_{0.15}CuO_4}$		$\mathrm{La_{1.80}Sr_{0.20}CuO_4}$	
T (K)	$\gamma(0)cm^{-1}$	$\gamma(90cm^{-1})cm^{-1}$	$\gamma(0)cm^{-1}$	$\gamma(90cm^{-1})cm^{-1}$
40	47	73	37	54
50	50	82		
100	82	150	77	90
300	308	550	146	166

Table 3.1: A comparison of $\gamma(0))$ and $\gamma(\omega)$.

The MIR Band

The conductivity of $La_{1.85}Sr_{0.15}CuO_4$ (Fig. 3.6 upper panel) at a temperature of 40K has a Drude form in that $\sigma_1(\omega)$ falls rapidly with frequency, but there is still a considerable amount of spectral weight between 400 and 6000 cm^{-1}. Using a scattering rate of 47 cm^{-1} (from table 3.1) and the Drude equation for $\sigma_1^{ab}(\omega)$:

$$\sigma_1(\omega) = \frac{\omega_p^2 \gamma}{4\pi(\gamma^2 + \omega^2)} \tag{3.10}$$

the predicted conductivity should be approximately 200 $(\Omega\ cm)^{-1}$ whereas the measured value is 900 $(\Omega\ cm)^{-1}$. A similar conclusion is reached for the overdoped sample. Fig. 3.7 shows that there is a significant conductivity in the MIR region. The normal state reflectivity curve of $La_{1.85}Sr_{0.15}CuO_4$ cannot be fitted with a simple Drude model, the mid-infrared band must be modelled using several Lorentzian oscillators. At present there are two ways of interpreting this and two ways of modelling it. The first is the two components approach in which the conductivity is considered to be the sum of free carriers (Drude like) and mid infrared carriers (bound). The Drude component is strongly temperature dependent whilst the MIR component is almost insensitive to temperature changes. Only the free carrier component condenses to form the superfluid, while the mid-infrared carriers which have a semiconductor like gap remain unaffected [7]. This is expressed in terms of the dielectric function:

$$\epsilon(\omega) = \epsilon_\infty - \frac{\omega_{pDrude}^2}{\omega(\omega + i\gamma)} + \sum_{i=1}^{n} \frac{S\omega_i^2}{\omega_i^2 - \omega^2 - i\omega\gamma} \tag{3.11}$$

Fig. 3.9 shows the real part of the optical conductivity $\sigma_1(\omega)$ decomposed into the Drude and MIR components, for both dopings. The MIR component shows a small gap $\approx$ 50 cm^{-1} but it's frequency range and effect extends from 50 to 6000 cm^{-1}. The Drude component scattering rate for the overdoped sample is slightly smaller than for the optimally doped sample. The main difference between the two samples occurs in their respective MIR contributions, the overdoped sample having a much smaller MIR component, especially in the 50 - 300 cm^{-1} range.
The second approach is the one component model in which there is only one type of carrier which interacts strongly with some type of optically inactive excitation [8, 9]. This results in a frequency dependent scattering rate $\gamma(\omega)$ and an enhanced effective mass at low frequencies.

$$\gamma(\omega) = \frac{\omega\epsilon_2}{\epsilon_\infty - \epsilon_1} \tag{3.12}$$

$$\omega_p^{*2}(\omega) = (\epsilon_\infty - \epsilon_1)(\omega^2 + \gamma^2(\omega)) \tag{3.13}$$

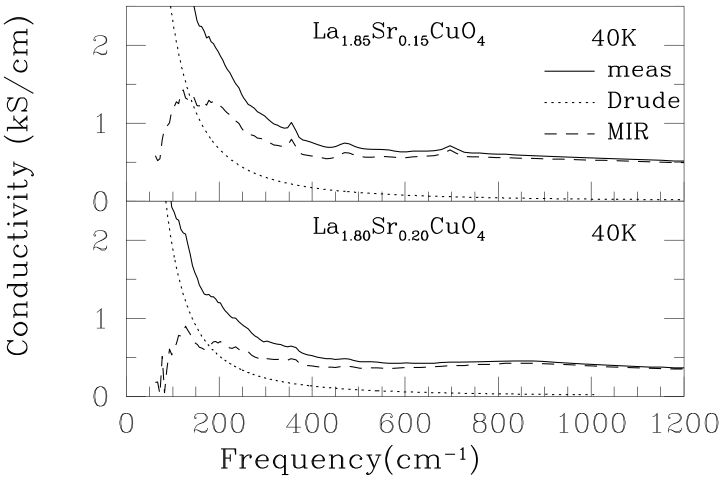

Figure 3.9: *Separate Drude and MIR components within the two component model for La$_{1.85}$Sr$_{0.15}$CuO$_4$ and La$_{1.8}$Sr$_{0.20}$CuO$_4$ at 40K.*

$$m^*(\omega) \;=\; \frac{4\pi n e^2}{\omega_p^{*2}(\omega)} \qquad (3.14)$$

The upper panel of Fig. 3.10 shows $\gamma(\omega)$ for La$_{1.85}$Sr$_{0.15}$CuO$_4$ and La$_{1.8}$Sr$_{0.20}$CuO$_4$ at T=4, 40, 100, and 300K. Considering La$_{1.85}$Sr$_{0.15}$CuO$_4$ in the FIR region, then the scattering rate $\gamma(\omega) \approx 70$ cm $^{-1}$ whilst at a frequency $\omega = 2000$ cm^{-1} $\gamma(\omega) \approx$ 1500 cm^{-1} i.e. a factor of 20 larger. Such a behaviour might be explicable within a strongly correlated electronic model or within a Luttinger Liquid model. For both samples the scattering rate is essentially linear with frequency, except below 500 cm^{-1}. There is no evidence for a pseudo gap at any of the temperatures.
The lower panel of Fig. 3.10 shows the frequency dependent effective mass m^*/m for both samples. The effective mass is large at low frequencies($\approx$ 3.5) and gradually decreases to 1 at 2000 cm^{-1}. There is no significant difference in the behaviour of m^*/m as a function of frequency for both samples.
The role of the MIR band in the transition to the superconducting state is still unresolved. Fig. 3.7 shows only a small change in $\sigma_1^{ab}(\omega)$ between 4 and 40K. It has been suggested that the phase transition is driven by a reduction in the Coulomb coupling energy between the CuO$_2$ planes and that this energy comes from the MIR band [10]. To test this hypothesis it is necessary to measure the loss function Im(-1/ϵ) for all k values up to the Brillouin zone boundary and to integrate this result for above and below T$_c$. This hypothesis cannot be tested using FIR spectroscopy as the resultant loss function is for $\Delta k \approx 0$. It will be

necessary to perform EELS(Electron Energy Loss Spectroscopy) measurements for all values of k. A second test would be to repeat these measurements with Zn substituted samples where T_c has been suppressed and verify that the reduction in Coulomb energy is smaller or zero. In order to compare the changes in the spectral weight more easily, the lower panel of Fig. 3.11 shows the integral of the conductivity (expressed as N_{eff}). The curves show the reduction in spectral weight for the overdoped sample at T=4 and 40K. The curves also show the considerable spectral weight that exists in the MIR band.

DC Conductivity $\sigma(0)$

The lower limit of the frequency measured by using the FIR spectrometer was 40 cm^{-1}, below this value a two fluid fit was performed down to $\omega = 0$. This approach gives $\sigma(0)$ the zero frequency conductivity for each temperature. By inverting the DC resistivity measurements we can also obtain $\sigma(0)$. A comparison of these two results is a useful check of the accuracy of the FIR measurements. Table 3.2 shows the extrapolated values of the DC conductivity $\sigma(0)$ obtained from the fitting procedure (Fit), from the Kramers-Kronig transformation (KK) and those obtained from resistivity measurements [2]. There is quite a good agreement between the three different methods.

	$\sigma(0)$ $(\Omega cm)^{-1}$ x=0.15			$\sigma(0)$ $(\Omega cm)^{-1}$ x=0.20		
Temp(K)	Ref. [2]	KK	Fit	Ref. [2]	KK	Fit
40	12.0	13.4	13.3	15.0	16.1	15.7
100	7	7.6	7.3	10	8.1	7.6
300	2.2	2.1	2.0	4.2	4.2	4.0

Table 3.2 Comparison of DC conductivity $\sigma(0)$ from resistivity measurements $\rho(0)$ and fitted values of $La_{2-x}Sr_xCuO_4$ for x=0.15 and x=0.20.

Phonons: Fig. 3.5 shows the measured absolute reflectivity and Fig. 3.6 shows the corresponding optical conductivity calculated using the Kramers-Kronig relationship, for both doping values. The optimally doped crystal shows three in-plane phonons at 128, 355 and 696 cm^{-1}. These phonons have not been detected before in room temperature, normal incidence measurements on single crystals [11]. The 128 cm^{-1} phonon appears due to the tetragonal ($T > 200K$) to orthorhombic ($T < 200K$) structural transition. Above the transition temperature this mode is degenerate, however below 200K, the degeneracey is gradually lifted with decreasing temperature. This mode then splits to 120 and 140 cm^{-1} in films

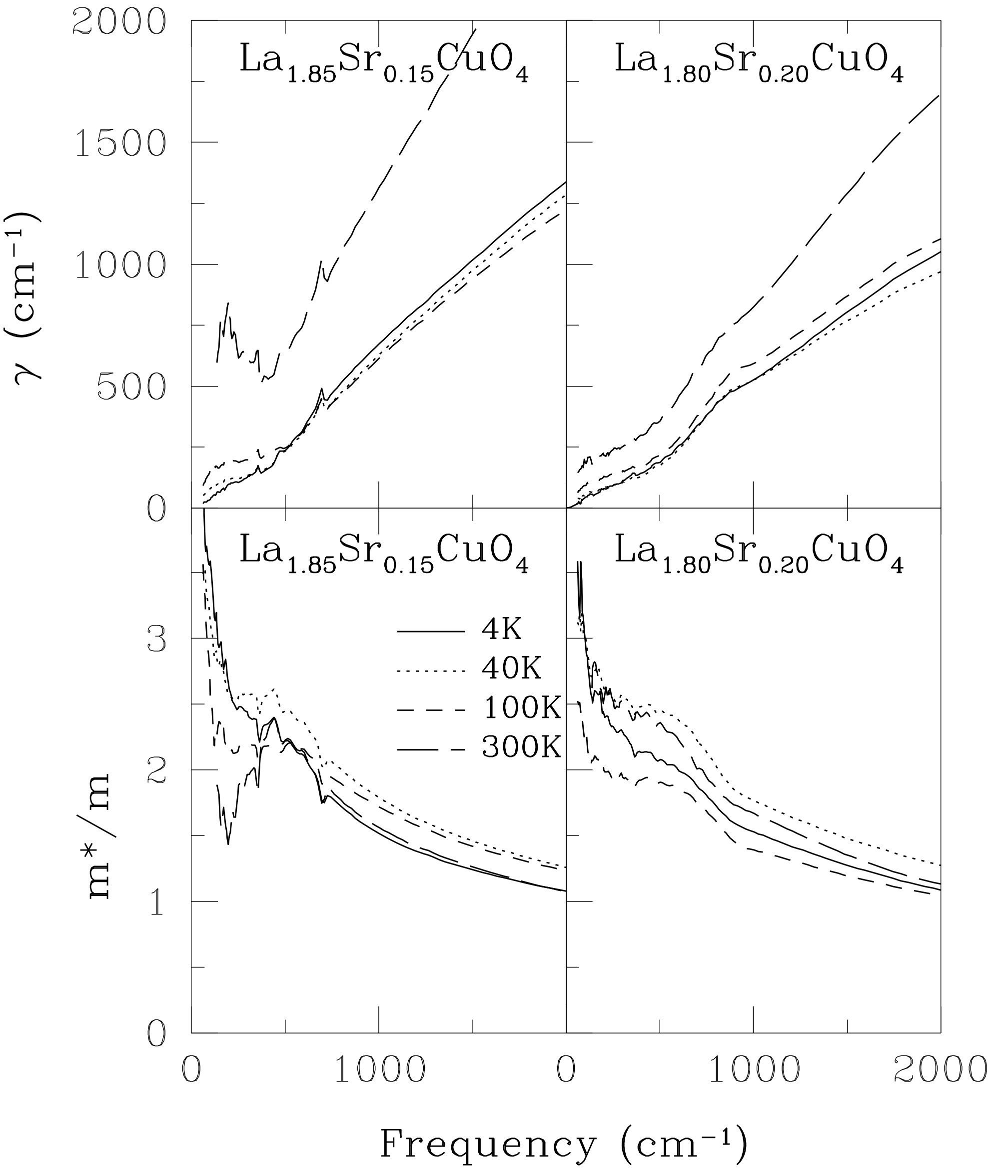

Figure 3.10: *Frequency dependence of the scattering rate* $\gamma(\omega)$ *and the effective mass* m^*/m.

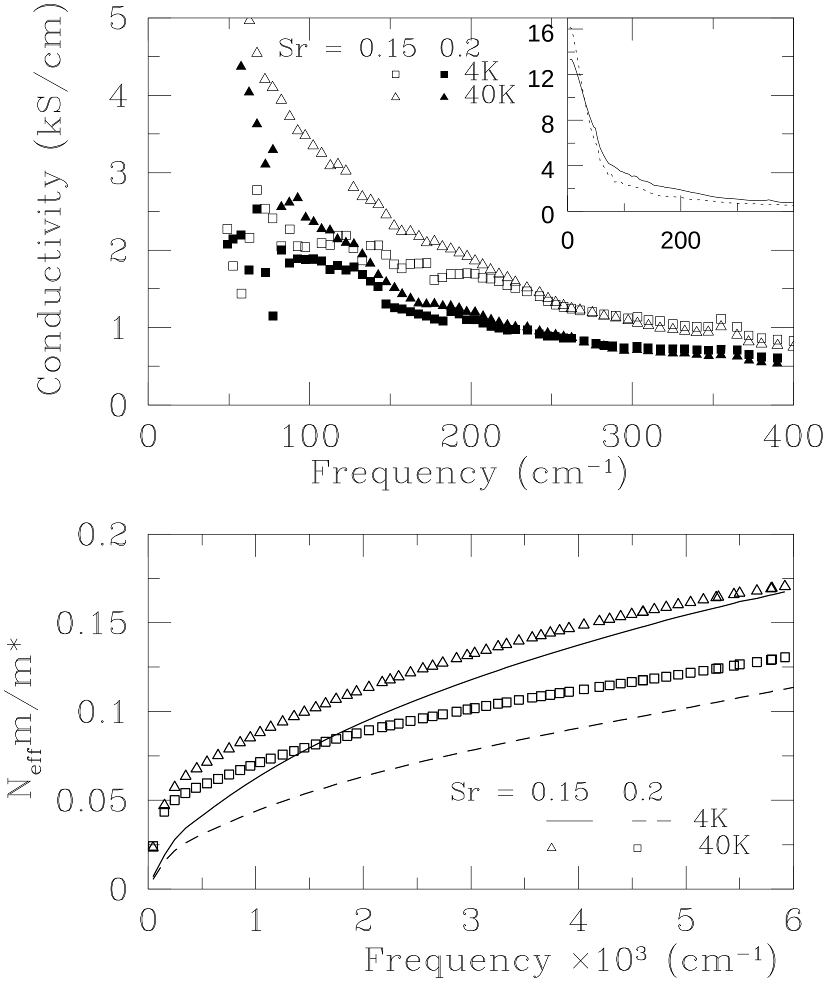

Figure 3.11: *Comparison of* $La_{1.85}Sr_{0.15}CuO_4$ *and* $La_{1.8}Sr_{0.20}CuO_4$ *for T=4 and 40K. Upper panel: Optical conductivity. Inset shows the extrapolated conductivity at zero frequency, solid line for Sr=0.15 and dotted line for Sr=0.20. The units of the x, y axes of the inset are the same as in the upper panel. Lower Panel: Effective charge* N_{eff} *for optimally and overdoped samples at* $T = 4, 40K$*.*

[12], however, due to the low oscillator strength of the two resulting modes, they are not clearly discernible.
All three phonons have a different mode of vibration [13]. The 128 cm^{-1} mode is classed as an external mode in which the La/Sr atom layer vibrates against the CuO_2 unit. The 355 cm^{-1} mode is a bending mode in which the Cu-O bond angle is modulated. The 696 cm^{-1} mode is a stretching mode in which the Cu-O bond distance is modulated. For the overdoped sample (Sr=0.2), both the 128 and the 696 cm^{-1} modes are no longer detectable. The mode at 355 cm^{-1} is detectable but has a reduced oscillator strength probably due to screening.

London Penetration Depth λ_L

On comparing the optical conductivity $\sigma_1(\omega)$ in the low energy range, above (40K) and below (4K) T_c, we observe a loss of spectral weight. This is transferred to the delta function at $\omega = 0$ and represents the superconducting condensate. The spectral weight transferred to $\omega = 0$ is related to the superconducting plasma frequency ω_{ps} and is given by the Ferrel-Glover-Tinkham sum rule :

$$\frac{\omega_{ps}^2}{8} = \int_{0^+}^{\omega_1} \left(\sigma_{40K}(\omega) - \sigma_T(\omega)\right) d\omega \tag{3.15}$$

where ω_1 is the upper frequency limit of the superconducting induced changes and T is the temperature below T_c. This transfer of spectral weight is related to the London penetration depth λ_L (see chapter 2.3.1):

$$\lambda_L = \frac{c}{\omega_{ps}} \tag{3.16}$$

The disadvantage of calculating the penetration depth by this method is that it is sensitive to the low frequency extrapolation used between 0 and 40 cm^{-1} and takes no account of the symmetry of the order parameter. At a temperature of 4K the superfluid fraction is approximately 0.7, the remainder of the spectral weight is made up of unpaired quasiparticles. The superfluid fraction (f_s) is calculated using the following formula:

$$f_s = \frac{\int_0^{\omega_1} \left(\sigma_{40K}(\omega) - \sigma_T(\omega)\right) d\omega}{\int_0^{\omega_1} \sigma_{40K}(\omega) d\omega} \tag{3.17}$$

where T is the temperature below T_c and 40K is the normal state temperature. If the order parameter has nodes on the Fermi surface then quasiparticles may be excited with extremely small energies. However these low energy excitations are not accounted for in the two fluid extrapolation procedure. Table 3.3 shows the

London penetration depth λ_L for both the optimally and overdoped samples. At 4K the penetration depth λ_{FGT} using the FGT sum rule, for the optimally and overdoped sample is found to be the same value of 360 nm. In order to reduce the low frequency range that must be extrapolated one needs to perform microwave and millimeter wave measurements below 40 cm^{-1} [14] which would reduce the region that had to be fitted and so the error in the conductivity.

	$La_{1.85}Sr_{0.15}CuO_4$			$La_{1.8}Sr_{0.20}CuO_4$		
T(K)	λ_{FGT} (nm)	$\delta(0)$ (nm)	f_s	λ_{FGT} (nm)	$\delta(0)$(nm)	f_s
4	360	300	0.680	360	330	0.70
15	360	300	0.680	360	330	0.7
20	400	360	0.550	450	420	0.45
27/25	464	360	0.42	780	700	0.153

Table 3.3: Comparison of λ_L for optimally and overdoped samples .

From table 3.3 the differences between the two samples becomes evident close to T_c where the superfluid fraction is small. The overdoped sample has a penetration depth of 780 nm, compared to 464 nm for the optimally doped sample. $La_{1.8}Sr_{0.20}CuO_4$ has a lower value of superfluid fraction. Table 3.3 also shows the classical skin depth $\delta(0) = c/\omega Im\sqrt{\epsilon}$ for $\omega \to 0$. The agreement between λ_{FGT} and $\delta(0)$ is reasonable for the overdoped sample where as for the optimally doped $\delta(0)$ seems to be insensitive to the changes in temperature. Figure 3.12 shows penetration depth plotted against the normalized temperature for both a s-wave model, a d-wave model and from Eqns. 4.5 3.16. The measurements do not agree with either model possibly due to the low frequency fitting procedure discussed earlier. Microwave surface impedance measurements performed on $La_{1.85}Sr_{0.15}CuO_4$ give $\lambda_L(0) = 400$ nm [15]. In the same reference $\lambda_L(0) = 250$ nm for $La_{1.8}Sr_{0.20}CuO_4$ was reported. This implies that the penetration depth continues to decrease with increasing doping beyond optimal doping. Muon spin relaxation measurements of $La_{2-x}Sr_xCuO_4$ show that the superfluid density n_s decreases (and so $\lambda_L(0)$ increases) in the overdoped region [16] which is also our conclusion.

Charge Carrier Density

When applying the f sum rule ($\int_0^W \sigma(\omega)d\omega = \omega_p^2/8$) to a doped Mott-Hubbard insulator it is necessary integrate to up to a sufficiently high frequency such that the electron behave as free electrons (see comment in 2.2.2). The undoped

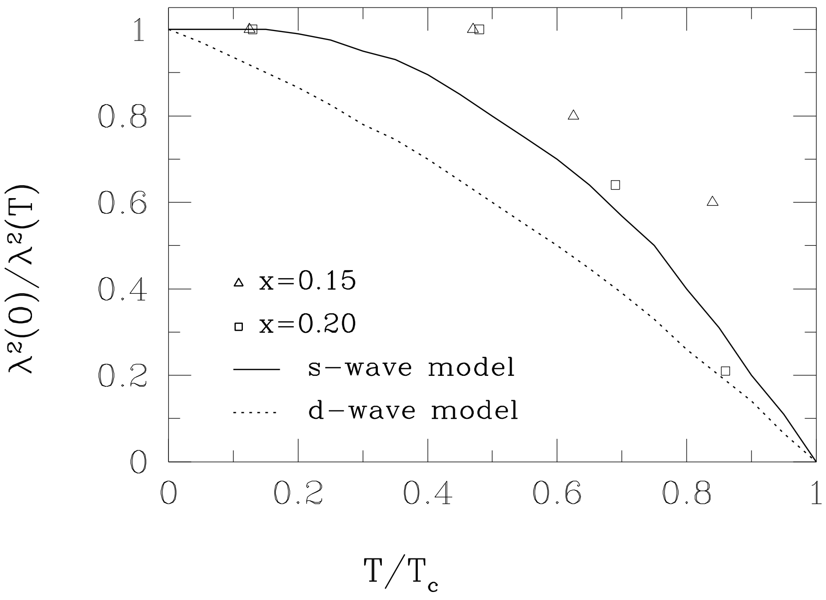

Figure 3.12: *Normalized penetration depth λ versus temperature for s and d wave models with calculated λ for $La_{2-x}Sr_xCuO_4$ x=0.15 and 0.2.*

parent compound La_4CuO_4 is a charge transfer insulator due to the oxygen p orbitals whose density of states lies between the upper and lower Hubbard bands. Reflectivity measurements up to 4 eV, on single crystals of $La_{2-x}Sr_xCuO_4$ for various values of x, show that as the doping is increased there is a transfer of spectral weight from the high energy side to the low energy side [11]. As the doping is increased, the spectral weight in the region 1 - 4 eV decreases whilst the spectral weight between 0 - 1 eV increases. The measurements outlined in this section were performed up to 0.76 eV. We can calculate the effective number of charge carriers per formula unit using the f sum rule provided we have determined the conductivity up to a sufficiently high energy. The effective number of charge carriers N_{eff} per formula unit(fu) is given by:

$$N_{eff}\frac{m}{m^*} = \frac{2mV_{cell}}{\pi e^2}\int_0^W \sigma(\omega)\, d\omega \tag{3.18}$$

where V_{cell} is the volume of a unit cell, m is the electron mass, m^* is the Fermi liquid quasiparticle effective mass and e is the electron charge.

By using Eqn. 3.18 and the fact that the overdoped sample has a smaller spectral weight in the high energy range than the optimally doped sample [11], we can calculate N_{eff} to gain an indication of the change in N_{eff} in the overdoped case. It is assumed that m*(the Fermi liquid quasiparticle effective mass) does not change very much between the optimally and overdoped sample. The lower panel of Fig. 3.11 shows $N_{eff}m/m^*$ for both doping concentrations at T = 4 and 40K and up to a frequency of 6000 cm^{-1}. In the normal state at 40K, N_{eff} for the overdoped crystal is smaller than for the optimally doped crystal. At a temperature of 4K and an excitation energy well above the BCS gap value of 82 cm^{-1}, the charge carriers are only quasiparticles as all the Cooper pairs have been broken, N_{eff} for the overdoped crystal is still the smaller of the two. Until recently it was understood that the effective number of free carriers increased with doping, and that beyond optimal doping, T_c was reduced due to pair breaking effects [17]. However, recent FIR reflectivity measurements on $Tl_2Ba_2CuO_6$ [18] show that beyond optimal doping, the density of mobile charge carriers does not continue to increase, but in fact decreases slightly. This also appears to be the case for overdoped $La_{1.8}Sr_{0.20}CuO_4$. This observation has important ramifications, namely whatever model/mechanism is proposed to explain HTSC in $La_{2-x}Sr_xCuO_4$, it must also naturally predict a decrease in N_{eff} beyond optimal doping.

Experimental Test of the Bipolaron-Polaron Model

The BCS theory of superconductivity assumes that the quasiparticles behave like a Landau Fermi Liquid (FL). However, the normal state properties of the cuprates are not like a Fermi Liquid. The difference is quite striking in the temperature dependence of the resistivity $\rho^{FL} \propto T^2$ whereas for optimally doped $La_{1.85}Sr_{0.15}CuO_4$ $\rho^{ab} \propto T$. The T^2 behaviour for a Fermi liquid is only valid at very low temperatures. Further, the NMR (Nuclear Magnetic Resonance) relaxation rate) $1/T_1T \sim$ constant (FL) whilst for the cuprates there is a temperature dependence. For some underdoped cuprates the relaxation rate begins to decrease well above T_c. This has since been attributed to the opening of a spin gap [19]. Finally, the specific heat for a metal is given by $C_v \sim T + T^3$ but the cuprates do not follow this relationship.

Several theories for HTSC propose a new ground state such as the marginal Fermi liquid proposed by Varma [20], the spin-charge separation model of Anderson [21] and the bipolaron-polaron model of Mott and Alexandrov. The nature of a polaron and bipolaron lend themselves to be probed by FIR spectroscopy and in a recent paper the bipolaron binding energy for $La_{2-x}Sr_xCuO_4$ was predicted [22]. Based upon the measurements described in this section this model will be tested. A polaron involves the self trapping of an electron which then may be excited out of it's well by absorption of a photon. A bipolaron is a singlet of two polarons which have a certain binding energy Δ_b. A bipolaron may be separated into two polarons by absorption of a photon i.e. $\hbar\omega \geq \Delta_b$. A polaron is formed when an electron polarizes it's surroundings and in so doing produces a potential well sufficient to localize it to a given site or to several lattice sites. The former situation is called a small polaron and the latter a large polaron. Polaron formation requires a relatively strong electron-phonon coupling and depends upon the elastic or deformability characteristics of the lattice. The electron associated with a small polaron spends most of it's time trapped close to a single atom. At low temperatures the electron moves by tunnelling (large enhancement of effective mass) and at high temperatures by thermally activated hopping (with enhancement of effective mass). The electron associated with a large polaron moves in a band with a small enhancement of mass [23]. Large polarons are formed when the long range electron-lattice interactions are dominant. Small polarons are formed when the short range electron-lattice interactions are dominant. The bipolaron-polaron model proposed by Alexandrov *et al* [24, 22] assumes the ab-plane normal state charge carriers to be a mixture of polarons and bipolarons. The ground state and the low energy excitation states are described by in-plane singlets (small bipolarons) and thermally excited polarons. The singlets tunnel along the ab-plane with an effective mass m^*_{ab} which is of the order of the polaron effective mass m^*_{ab} and $m^*_{ab} \approx 10\ m_e$ (rest mass of an electron). The electron-phonon coupling parameter $\lambda \geq 0.5$, which is not considered particularly strong, as for a classical BCS weak coupling superconductor $\lambda \approx 0.3$.

The ground state is considered to be a Bose-Einstein condensate of spin lattice bipolarons with charge $2e$. The bipolarons are therefore considered preformed pairs in the normal state and below T_c phase coherence is established between the pairs to form a superfluid condensate. The bipolaron model for $La_{2-x}Sr_xCuO_4$ predicts a binding energy Δ_b which is doping dependent as the bipolarons screen the electron-phonon coupling. For the optimally doped sample $La_{1.85}Sr_{0.15}CuO_4$, $\Delta_b = 200$ cm^{-1} (300K, 25 meV) and for the overdoped sample $La_{1.8}Sr_{0.20}CuO_4$ $\Delta_b = 70$ cm^{-1} (100K, 9 meV) [22]. Both binding energies are almost constant as a function of temperature above T_c and up to 500K. The binding energy for both optimal and the overdoped sample lies within the FIR range and should appear as a peak in the optical conductivity $\sigma_1(\omega)$. For the optimally doped sample this absorption peak should appear at a temperature of 40K and then gradually broaden as the the temperature is increased. The peak should disappear above 300K as this is the binding energy. For the overdoped case it is expected that at a temperature of 40K the absorption peak in the optical conductivity will be rather broad and it will gradually disappear as the temperature approached 100K.

Fig. 3.11 shows the optical conductivity for both doping values at 40K and in a frequency range up to 400 cm^{-1}. For the optimally doped sample there is no peak in the vicinity of 200 cm^{-1}. The phonon at 360 cm^{-1} is an example of what we would expect. Fig. 3.6 shows the optical conductivity as a function of temperature up to 300K, and here again there is no sign of an absorption peak. The same conclusion is reached for the overdoped sample. A serious drawback of the bipolaron theory is that ARPES (Angle Resolved Photo Electron Spectroscopy) measurements show a Fermi surface which should not be present. Secondly in the bipolaron theory the effective mass in the c direction is enhanced by a factor greater than 100. In the normal state, polaron transport in the c direction should be strongly dependent upon the c-axis distance between CuO planes as the transport is by tunnelling. The tunnelling probability has an exponential dependence. For $La_{1.85}Sr_{0.15}CuO_4$ $d^c = 6.6$ Å whilst for $Tl_2Ba_2CuO_6$ $d^c = 11.5$ Å. Therefore we would expect a large difference in the c-axis optical conductivity $\sigma_c(\omega)$ for these two materials in the normal state i.e. just above T_c. But this is not seen in measurements (see chapter 5). The bipolaron model predicts a s-wave order parameter but most experiments indicate an order parameter with nodes.

3.4 Conclusions

The technique of PARIS has shown to be able to amplify the small changes in the absorption of a highly reflecting superconductor. The technique was tested on NbN, where the exact value of the BCS gap ($2\Delta = 6$ meV) was measured. Photon excitation of $La_{1.85}Sr_{0.15}CuO_4$ and $La_{1.8}Sr_{0.20}CuO_4$ within the BCS gap region at T = 4K shows a residual conductivity. The form of the optical conductivity $\sigma_1(\omega)$ cannot be modelled using an isotropic s-wave order parameter, but can be using a d-wave order parameter. The use of *in-situ* Au evaporation allows the absolute reflectivity to be measured without introducing errors due to movement of the sample. A modified Kramers-Kronig approach to obtain the complex conductivity has shown that the recalculated reflectivity agrees with the measured reflectivity $R(\omega)$ for the the full frequency range measured.

The conductivity $\sigma_1(\omega)$ for the overdoped sample, at 40K, showed a reduction in the spectral weight of the quasiparticle excitations, particularly in the gap energy range. This reduction of spectral weight in the overdoped sample may also be interpreted as as reduction in the effective number of carriers N_{eff}. This reduction is contrary to what is found in going from the underdoped to the optimally doped regime (Sr = 0.10 to 0.15) where N_{eff} increases. A possible explanation for the reduction in the charge carrier density, in going from the optimally to the overdoped regime is due to a localization effect. However, one would expect an absorption peak in $\sigma_1(\omega)$ at the localization energy. Additionally, we would also expect this peak to be strongly temperature dependent. Neither of these effects have been observed in the energy range of 50 - 6000 cm^{-1}. Any microscopic model attempting to explain HTSC must naturally produce this effect of a reduction in N_{eff} and T_c, in the doping range Sr= 0.15 to 0.20. The bipolaron model was tested based upon the theoretical prediction of the binding energy and no absorption peak was found at the expected binding energy Δ_b.

References

[1] R. Kop, P. de Vries, R. Sprik, and A. Lagendijk (unpublished).

[2] Y. Nakmura and S. Uchida, Phys. Rev. B **47**, 8369 (1993).

[3] Burns, *An Introduction to HTSC* (Academic Press, London, 1979).

[4] F. Wooten, *Optical Properties of Solids* (Academic Press, New York, 1972).

[5] G. Junk and A. Roseler, Phys. Stat. Sol. **137**, 117 (1986).

[6] D. van der Marel, H. Habermeier, D. Heitmann, W. König, and A. Wittlin, Physica C **176**, 1 (1991).

[7] D. Tanner and T. Timusk, *Physical Properties of High Temperature Superconductors Volume 3 ed D. Ginsberg* (World Scientific, Singapore, 1993).

[8] G. A. Thomas, J. Orenstein, D. H. Rapkine, M. Capizzi, A. Millis, R. N. Bhat, L. F. Schneemeyer, and J. V. Waszak, Phys. Rev. Lett. **61**, 1313 (1988).

[9] R. T. Collins, Z. Sclesinger, F. Holtzberg, P. Chaudri, and C. Feild, Phys. Rev. B **39**, 6571 (1989).

[10] A. Leggett (unpublished).

[11] S. Uchida, T. Ido, H.Takagi, T. Arima, Y. Tokura, and S. Tajima, Phys. Rev. B **43**, 7942 (1991).

[12] F. Gao, D. B. Romero, D. B. Tanner, J. Talvacchio, and M. G. Forrester, Phys. Rev. B **47**, 1036 (1993).

[13] S. Tajima, T. Ido, S. Ishabashi, T.Itoh, H. Eisaki, Y. Mizuo, T. Arma, H. Takagi, and S. Uchida, Phys. Rev. B **43**, 10496 (1991).

[14] B. P. Gorshunov, A. V. Pronin, A. A. Volkov, H. S. Somal, D. V. der Marel, B. J. Feenstra, Y. Jaccard, and J.-P. Locquet (unpublished).

[15] T. Shibauchi, H. Kitano, and K. Uchinokura, Phys. Rev. Lett. **72**, 2263 (1994).

[16] Y. J. Uemura and et al, Phys. Rev. Lett. **62**, 2317 (1989).

[17] J.Tallon, Phys. Rev. Lett. **71**, 1764 (1993).

[18] A. Puchkov, P. Fournier, T. Timusk, and N. Koleshnikov, Phys. Rev. Lett. **77**, 1853 (1996).

[19] B. Bücher, P. Steiner, J. Karinski, E. Kaldis, and P. Wachter, Phy. Rev. Lett. **70**, 2012 (1993).

[20] C. M. Varma, P. R. Littlewood, S. Scmitt-Rink, E. Abrahams, and A. Ruckenstein, Phys. Rev. Lett. **63**, 1996 (1989).

[21] D. G. Clarke, S. P. Strong, and P. W. Anderson, Phys. Rev. Lett. **72**, 3218 (1994).

[22] A. S. Alexandrov, V. V. Kabanov, and N. F. Mott, Phys. Rev. Lett. **77**, 4796 (1996).

[23] D. Emin, Phys. Rev. B **48**, 13691 (1993).

[24] A. S. Alexandrov, Phys. Rev. B **53**, 2863 (1996).

4

c-Axis Electrodynamics of $La_{2-x}Sr_xCuO_4$

The infrared reflectivity of $La_{1.85}Sr_{0.15}CuO_4$ *single crystals with* $\vec{E}$ *parallel to the c-axis is analyzed. The plasma edge at around 6 meV (50* cm^{-1}*), which occurs only for* $T < T_c$*, is due to Cooper-pair tunneling. This low value of the plasma edge is shown to be consistent with the c-axis plasma frequency obtained from LDA band structure calculations (*> 0.1 *eV) if we take into account that the single-particle charge transport along the c axis is strongly incoherent in the normal state, and remains so in the superconducting state. From a comparison of the optical conductivity with model calculations based on s and d-wave weak coupling theory in the dirty limit, we find no evidence for a reduction of the c-axis quasi-particle scattering rate below* T_c*. The c-axis scattering rate, the normal-state c-axis plasma frequency, and* T_c *obey* $h\gamma > h\nu_p \gg 3.5k_BT_c$*, which is exactly opposite to the clean limit.*

PARIS measurements of $La_{1.80}Sr_{0.20}CuO_4$ *using s-polarized light with* $\vec{E}$ *parallel to the c-axis show an increase in the optical conductivity in the low frequency region, implying that the transport is becoming 'metallic'. A plasma edge occurs at 100* cm^{-1} *which is now well above the BCS gap value of* $3.5kT_c = 74$ cm^{-1}*.* [1]

---

[1] Part of this chapter has been published: J. H. Kim, H. S. Somal, M. T. Czyzyk, D. van der Marel, A. Wittlin, A. M. Gerrits, V. H. M. Duijn, N. T. Hien and A. A. Menovsky Physica C, 247, p297 (1995)

4.1 Introduction

In the early days of high temperature superconductivity the general view was that the mechanism responsible for the pairing of the electrons in the superconducting state was to be found in the CuO_2 planes. The intervening layers between the CuO_2 planes were considered to be charge reservoirs that determined the hole or electron density in the planes. In effect they were considered to be inert insulating layers in the phase transition to the superconducting state. However once single crystals were available, c-axis resistivity measurements $\rho^c(T)$ showed that the temperature dependence was semiconductor like i.e. as the temperature decreased, ρ^c increased [1]. The picture now was of metallic CuO_2 planes separated by, but also coupled by, insulating oxide layers. For $La_{2-x}Sr_xCuO_4$, as the hole doping in the CuO_2 planes is increased the c-axis resistivity decreases. As for the cuprates superconductivity is a bulk three dimensional state, there arose the question of how the paired electrons were able to move freely in the c direction when previously the transport was effectively blocked i.e. it was incoherent and non-metallic.

The role of coupling between planes along the c-axis was further highlighted by P. W. Anderson and collaborators, when it was proposed that the Josephson coupling energy (interlayer tunnelling) between the CuO_2 layers was proportional to T_c [2]. The picture was complicated by the diversity of materials, which had one, two or three CuO_2 planes per unit cell. $YBa_2Cu_3O_{6+\delta}$ has chains in the b direction, which further complicates the number of coupling combinations of $J_\perp$ (where $J_\perp$ is the exchange energy perpendicular to the CuO_2 planes) between two unit cells and within one unit cell. Infrared measurements of the c-axis optical reflectivity, on a single crystal of $La_{2-x}Sr_xCuO_4$ revealed the existence of a low energy plasma edge. This appeared only in the superconducting state [3] and below the BCS gap energy. This collective electronic excitation had been theoretically predicted by Inui [4] and Mishonov [5]. Far infrared reflectivity measurements of the c-axis on underdoped $YBa_2Cu_3O_{6+\delta}$ [6] revealed not only a low energy plasma edge (for $T < T_c$) but also a suppression of the optical conductivity $\sigma_1^c(\omega)$ for $T > T_c$, in the low energy region. This was attributed to the existence of a pseudo gap.

One of the striking aspects of the high T_c cuprate superconductors is the large anisotropy (ratio of c-axis to ab-plane) of their physical properties, related to their layered structure. The anisotropy ratio, following from a conventional Fermi-liquid approach based on LDA (local density approximation) band structure calculations, is of the order of 10 in most of these compounds, experimentally it is found to be much larger, as found from e.g. the optical conductivity σ_1^{ab}/σ^c and the normal-state resistivity ρ^{ab}/ρ^c. One can also compare the theoretical and experimental values of the ab-plane and the c-axis plasma frequencies in order to check further the reliability of LDA based band structure calculations.

In the superconducting state the anisotropy manifests itself strongly in the penetration depth measurements and in the far infrared reflectivity spectra. Although the normal state c-axis response looks like an insulator, in the superconducting state in some materials a plasmon-related zero crossing of the real part of the dielectric function (ϵ_1) is found. But at an energy far below the value expected from LDA band structure calculations. Soon after the discovery of high-T_c superconductivity, a reflectivity edge in the spectra of polycrystalline $La_{1.85}Sr_{0.15}CuO_4$ was observed below T_c near 50 cm^{-1} and it was eventually attributed to a plasmon along the c axis [7, 8, 9, 10, 11]. Subsequently, Sherwin *et al.* [12] proposed that this low plasma frequency and its temperature dependence could be explained by a strong damping of the c-axis plasmon or the opening of a gap below T_c. However, due to ambiguities in the interpretation of the optical data of the strongly anisotropic polycrystalline material, no firm conclusions were reached regarding this point.

Results obtained for single crystals of $La_{1.85}Sr_{0.15}CuO_4$ [3], $Bi_2Sr_2CaCu_2O_8$ [13, 14], $YBa_2Cu_3O_7$, [15, 6], and $YBa_2Cu_4O_8$ [16] suggest that the anisotropy of the low-frequency optical properties and the very low value of the c-axis plasmon may be a common feature of all of the high-T_c cuprate superconductors, and raises the question as to it's origin. In a number of papers [3, 17] a large effective mass along the c direction has been assumed to explain the far-infrared spectra and the penetration depth of single crystals of $La_{2-x}Sr_xCuO_4$. A mass enhancement could follow from e.g spin-charge separation [18, 19, 20, 21, 22]. Alternatively, in the context of a Fermi-liquid description, incoherent c-axis transport arising from elastic and inelastic scattering processes has been proposed by Graf *et al.* [23] and Rojo *et al.* [24] respectively. Such scenarios could lead to incoherent transport at energies larger than typically $\tilde{t}_\perp/8$, where $\tilde{t}_\perp$ is the effective interlayer hopping energy. Such approaches are still within the general paradigm of Fermi liquid theory, in contrast to other approaches based on the concept of spin-charge separation. The Fermi-liquid approaches to this problem have been criticized by P. W. Anderson e.g. in Ref. [21].

It should be noted that in this chapter the unit of frequency used is ν and ω where $\omega = 2\pi\nu$. The units of frequency remain cm^{-1} or eV.

4.2 Results

4.2.1 Experiment

A single crystal of $La_{2-x}Sr_xCuO_4$ with a nominal Sr content of 15% was grown by the traveling solvent floating zone method [25]. Electron-probe micro-analysis showed the correct phase with no contamination or inclusion of second phases, and a homogeneous distribution of Sr. The crystals have a sharp superconducting transition with the onset at 35 K at optimal doping and with 90 % of the transition within 3 K as determined from AC susceptibility measurements at 3 Gauss and 90 Hz. Neutron diffraction measurements demonstrated that the as-grown boule contain large single crystalline grains. Samples for reflectivity measurements were cut perpendicular to the b axis and were mechanically polished to optical quality. The surface in the ac plane was approximately 4 mm×7 mm. X-ray Laue backscattering showed a correct orientation with sharp, well-defined single diffraction spots. Polarized infrared reflectivity spectra were measured in the range 30 to 10000 cm^{-1} at temperatures between 8 and 300 K using a rapid scan Fourier transform infrared (FTIR) spectrometer equipped with a continuous flow liquid He cryostat. The same measurements were performed at two different laboratories. The data obtained in the two locations on crystals with the same nominal composition(Sr = 0.15) are in good agreement with each other, and with those of Tamasaku *et al.* [3].

4.2.2 Normal-State Reflectivity

Fig. 4.1 shows the reflectivity (R) of a $La_{1.85}Sr_{0.15}CuO_4$ single crystal with $\vec{E} \parallel \vec{c}$ at various temperatures. An expanded view of the low-frequency region is given in Fig. 4.2. The normal-state reflectivity is replotted in Fig. 4.3 (circles) for closer inspection. The shape is characteristic of an ionic insulator with strong infrared-active phonons dominating the far-infrared region. At low frequencies there is a Hagen-Rubens like upturn, in R indicative of a poor conductor: $R(\nu) = 1-2\sqrt{\nu/\sigma_0}$ where σ_0 is the DC conductivity. The real part of the conductivity σ_1 ($\sigma = \sigma_1 + i\sigma_2$) is nearly constant in the relevant frequency range ($\approx 7\ \Omega^{-1}\mathrm{cm}^{-1}$ see Fig. 4.5). Having no *á priori* knowledge about the frequency dependence of the electronic contribution to the conductivity, it was attempted to fit the experimental data assuming that the real part of the conductivity has the Drude-Lorentz line shape $\sigma_1(\nu) = \sigma_0(1+\nu^2/\gamma^2)^{-1}$ where γ is the damping rate. However as will be shown later, $\sigma_1(\nu)$ turns out to be very broad and featureless, and with this formula we are really testing the value of σ_1 at $\nu = 0$, and its departure thereof in leading orders of ν^2. This becomes evident if we expand the denominator in a power series with ν^2/γ^2 being less than one for the FIR range of frequencies. The electronic contribution is given by $\sigma_1(\nu) = \sigma_0(1+\nu^2/\gamma^2)^{-1}$, where σ_0, γ were determined by fitting this equation to the measured reflectivity.

The phonons were fitted using a Lorentzian oscillator of the form

$$\epsilon(\omega) = \frac{S\omega_{TO}^2}{(\omega_{TO}^2 - \omega^2) - i\gamma} \tag{4.1}$$

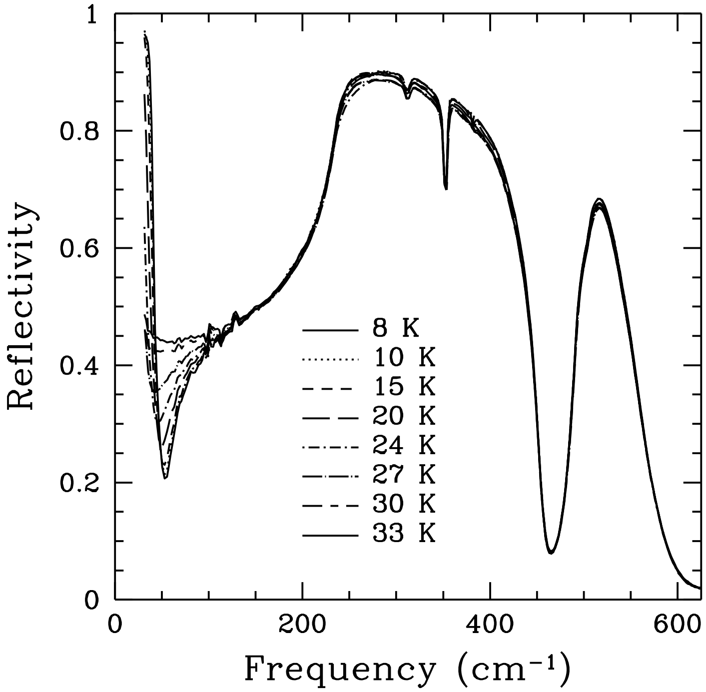

Figure 4.1: *The c-axis reflectivity of* $La_{1.85}Sr_{0.15}CuO_4$ *at 8, 10, 15, 20, 24, 27, 30, and 33 K.*

where ω_{TO} is the centre frequency, S is the oscillator strength, and γ is the damping rate. The parameters used for the transverse optical (TO) phonons, are shown in Fig. 4.3, the fit is shown by the solid line. There are two strong phonons at 242 and 494 cm^{-1} with two weak phonons at 312 and 351 cm^{-1}. A successful fit in the range of 20 to 650 cm^{-1} is obtained *only* by assuming $\gamma > 4500$ cm^{-1} in the above formula. To demonstrate the effect of assuming a smaller value for γ, Fig. 4.3 shows a curve corresponding to $\gamma = 292$ cm^{-1} with all the other parameters the same as before. Clearly there are now deviations in the frequency range between 200 and 800 cm^{-1}. Similar observations were made on another sample from the same batch of single crystals. This is also born out by the analysis of the spectra at temperatures above and below T_c, and from re-analyzing the experimental data published by Tamasaku *et al.* [3] (see also Fig. 4.4, and the corresponding discussion in subsection 4.2.3).

A second important observation to be deduced from Fig. 4.3 is that there is no noticeable influence of the value of σ_1 on the reflectivity spectrum for $\nu > 1000$ cm^{-1}: the theoretical spectra for $\gamma \approx 4700$ cm^{-1} and $\gamma \approx 290$ cm^{-1} coincide within the

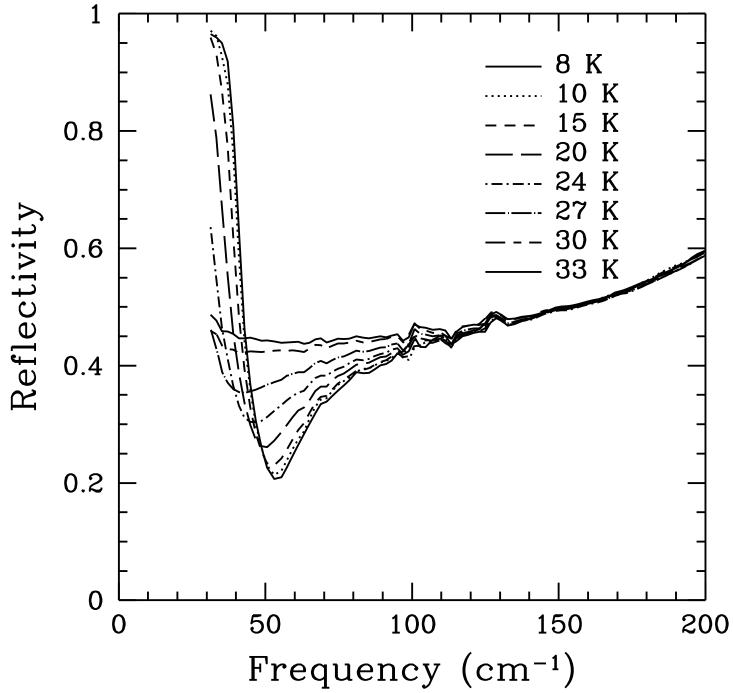

Figure 4.2: *The temperature dependent low-frequency c-axis reflectivity of* $La_{1.85}Sr_{0.15}CuO_4$.

plotting accuracy. This indicates that the reflectivity in this frequency range is independent of the low energy behaviour of $\sigma_1^c(\omega)$

Based upon the measurements it is not possible to support or oppose the $\omega^{-1/4}$ scaling law predicted by Clarke, Strong and Anderson [21], a hopping type of behaviour, or simple Drude behaviour.

On the other hand, none of these models, predicts an abrupt step in σ_1 at frequencies larger than 0.1 eV. One can exploit this fact to place an upper bound on the optical effective mass along the c direction by employing the f-sum rule ($\int_0^\infty \sigma_1(\nu)d\nu = ne^2/4m$) where n is the electron density, e the electronic charge, and m the electronic mass. By restricting the integration interval within the bounds of the bandwidth W, while staying below the first interband transitions, $1/m$ would in a single particle picture correspond to Fermi-surface average over the c-axis effective mass tensor element. This implies that $\int_0^W \sigma_1(\nu)d\nu = (\pi/4)\nu_p^2$ where ν_p is the plasma frequency in the c direction as would follow from an LDA band structure calculation. By integrating the corresponding expression for

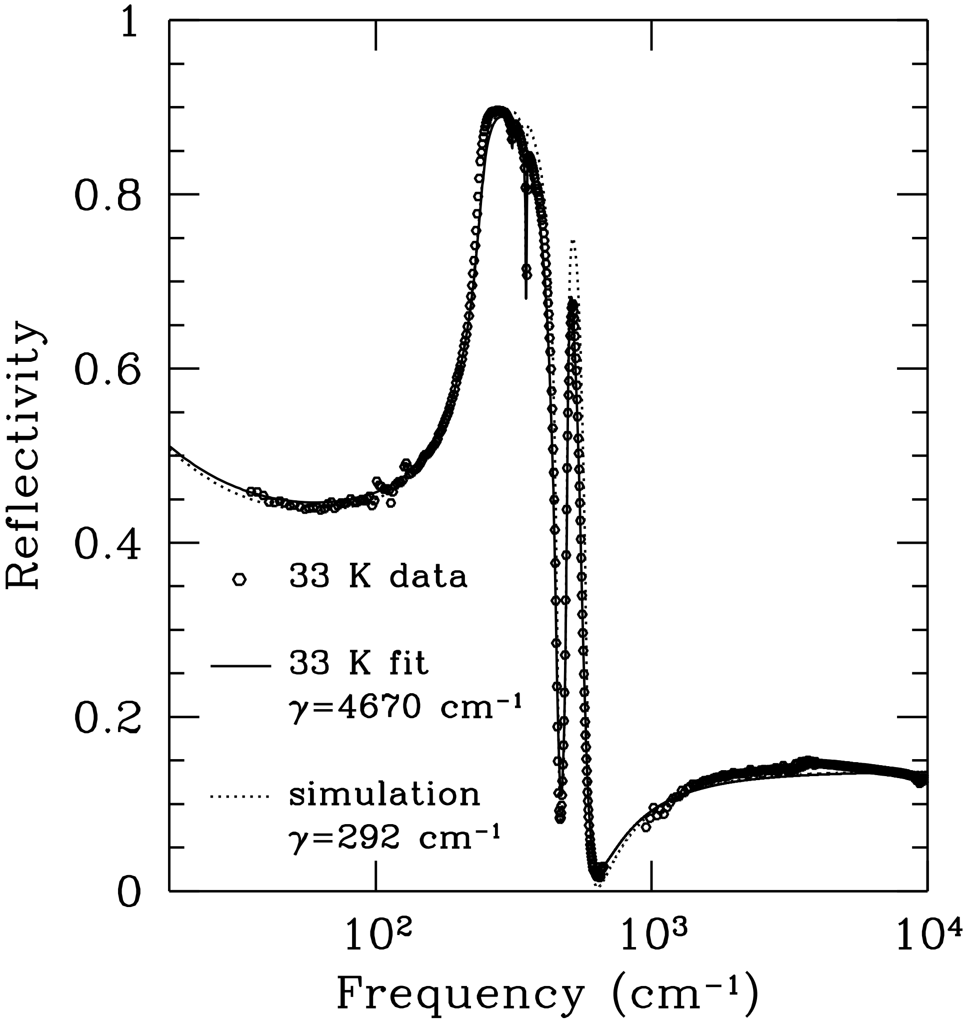

Figure 4.3: *The c-axis reflectivity of* $La_{1.85}Sr_{0.15}CuO_4$ *at 33 K (circles) along with the least-square-fitted curve (solid line). The best fitting parameters are* $\epsilon_\infty = 4.75$, $\sigma_0 = 7\ \Omega^{-1}\ cm^{-1}$, $\gamma = 4670\ cm^{-1}$, *and* $\nu_p = 1320\ cm^{-1}$. *The TO phonons were parameterized with* $\{\omega_i\ (cm^{-1}),\ \gamma_i\ (cm^{-1}),\ S_i\}$ $(i = 1 \cdots 4)$: $\{241.5,\ 24.8,\ 17.6\}$, $\{312.0,\ 3.0,\ 0.019\}$, $\{351.0,\ 3.0,\ 0.044\}$, $\{494.1,\ 12.8,\ 0.33\}$. *In order to test the reliability of the fit, we also plot a simulated reflectivity curve (dotted line) corresponding to* $\gamma = 292\ cm^{-1}$ *and* $\nu_p = 330\ cm^{-1}$ *with the phonon parameters of the best fit. Although the change in* γ *and* ν_p *will not affect the DC conductivity, the overall agreement with experiment is reduced. The electronic component of conductivity is indeed quite flat.*

$\sigma_1(\nu)$, one can put a lower bound on the plasma frequency $\nu_p = 0.15$ eV (note $\nu_p = \sqrt{2\sigma_0\gamma}$ in the Drude model).

Due to the broadening of σ_1 over a large frequency range, the energy ν_p no longer corresponds to the collective mode of the electron gas, i.e., the zero crossing of the real part of the dielectric function ($\epsilon = \epsilon_1 + i\epsilon_2$). In fact with these parameters the zero crossing of $\epsilon_1(\nu) = \tilde{\epsilon}_\infty - \nu_p^2/(\nu^2 + \gamma^2)$ (where $\tilde{\epsilon}_\infty$ is the high-frequency dielectric constant prevailing in the far-infrared spectral region) occurs for $\nu^2 < 0$, and the plasmon has a diffusive pole in the normal state. Hence, the c-axis plasmon is *overdamped in the normal state* (rather than extremely small in energy or completely absent) due to the broadening of σ_1, and the c-axis plasma frequency is of the same order of magnitude as that predicted by LDA band structure calculations. This point regarding the broadening will be discussed further in section 4.3.

4.2.3 Superconducting-State Reflectivity

As the temperature is decreased below T_c, a plasma edge develops, which moves to a higher frequency with decreasing temperature and reaches about $2k_BT_c$ (50 cm^{-1} or 6 meV) as $T \to 0$. At the same time, the changes in reflectivity for $\nu > 200$ cm^{-1} are quite small. The phonon at 241.5 cm^{-1} has a very large oscillator strength which masks the electronic contribution to the conductivity in this range. However, it is noticeable that the minima at 460 cm^{-1} and 630 cm^{-1}, and the maximum at 510 cm^{-1} have only very weak temperature dependence. This implies that the electronic contribution to the conductivity σ_1 at frequencies higher than approximately $4k_BT_c$ is not affected by the superconducting phase transition. In this respect the present behavior is not much different from what happens in a classical BCS superconductor.

The procedure outlined in Ref. [26] for the ab-plane response of $YBa_2Cu_3O_{7-\delta}$, for frequencies not too small compared to the scale of the gap energy was used. The reflectivity in the superconducting state can be analyzed in a phenomenological way using the two-fluid Gorter-Casimir model for the dielectric function ϵ:

$$\epsilon(\nu) = \tilde{\epsilon}_\infty \left(1 - \frac{\tilde{\nu}_{ps}^2}{\nu^2}\right) - \frac{\nu_p^2 - \tilde{\nu}_{ps}^2}{\nu(\nu + i\gamma)} \qquad (4.2)$$

As the phase ϕ and the electron density are conjugate variables we can use either interchangeably. As the plasma frequency in the superconducting state is an oscillation of the phase ϕ (ref. section 4.3.4) of the condensate, the term 'phason' was introduced [4]. The phason is a collective oscillation of the condensate. Therefore we can write the above equation as

$$\epsilon(\nu) = \tilde{\epsilon}_\infty \left(1 - \frac{\tilde{\nu}_\phi^2}{\nu^2}\right) + \frac{2i\sigma_n(T)}{\nu(1 - i\nu/\gamma)} \tag{4.3}$$

where $\tilde{\nu}_\phi^2$ is then the phason frequency, $\sigma_n(T)$ is the conductivity of the quasiparticles.

The second term represents the 'normal fluid'. Even in a conventional s-wave superconductor the conductivity is finite (except for $T = 0$) for frequencies below the gap due to the presence of a finite density of quasiparticles which are thermally excited across the gap. If the order parameter has nodes, this effect becomes even larger. A difficulty arises in employing Eqn. 4.3 at low frequencies(typically smaller than $0.5k_BT_c$) where coherence factors play an important role. As a result the conductivity line-shape becomes manifestly non-Drude like at low frequencies. The superconducting-state reflectivity data is fitted for frequencies about $2k_BT_c$(46 cm^{-1} up to 100 cm^{-1}). An important point to be noticed here is that by restricting the fitting range to the region around the plasma minimum, the value for σ_0 is mainly determined by the value of the reflectivity at the minimum, where

$$R = \frac{\sqrt{2} - (1 + \sqrt{1 - \epsilon_2})^{1/2}}{\sqrt{2} + (1 + \sqrt{1 - \epsilon_2})^{1/2}} \tag{4.4}$$

so that $\sigma_n(T)$ can be read directly from the reflectivity curves using $\sigma_n(T) \approx 2\nu\sqrt{R}$. The fitting results are summarized in Fig. 4.3.

The dotted curve in Fig. 4.4 corresponds to the fit parameters used by Tamasaku *et al.* for 8 K [3]. Note that with their fit parameters ($\tilde{\epsilon}_\infty = 25$, $\tilde{\nu}_\phi = 56$ cm^{-1}, $\tilde{\nu}_p = 60$ cm^{-1}, and $\gamma = 2$ cm^{-1} in the notation of Eqn. 4.5), nearly all the oscillator strength under the conductivity σ_1 collapses into the δ-function at the zero frequency. This essentially corresponds to the clean limit. But clearly, their fit parameters cannot reproduce the experimental results to a satisfactory degree (see Fig. 4.4). A much better fit is obtained by assuming a broad and featureless electronic part of the conductivity σ_1, as in the normal-state case. Initially it was attempted to vary all parameters. At all temperatures the best fits indicated that $\nu \ll \gamma$, and only small and unsystematic changes of $\tilde{\epsilon}_\infty$ with temperature were obtained. Therefore, we repeated the analysis with $\gamma \to \infty$, replacing $\tilde{\epsilon}_\infty$ by the sum of ϵ_∞ and the oscillator strengths of the four TO phonons (see Fig. 4.3). To estimate the influence of dispersion of the TO phonons, we also did this analysis using the full set of phonon parameters as given in Fig. 4.3. In both cases, it was possible to fit the reflectivity spectra at all temperatures without assuming drastic temperature dependence in the damping rate γ.

The temperature dependence of the reflectivity then depends mainly upon $\tilde{\nu}_\phi$ and σ_n. The temperature dependence of the two parameters $((\tilde{\nu}_\phi(T)/\tilde{\nu}_\phi(0))^2$ (proportional to the superfluid fraction) and $\sigma_n(T)/\sigma_n(T_c)$, with $\tilde{\nu}_\phi(0) = 38$ cm^{-1}

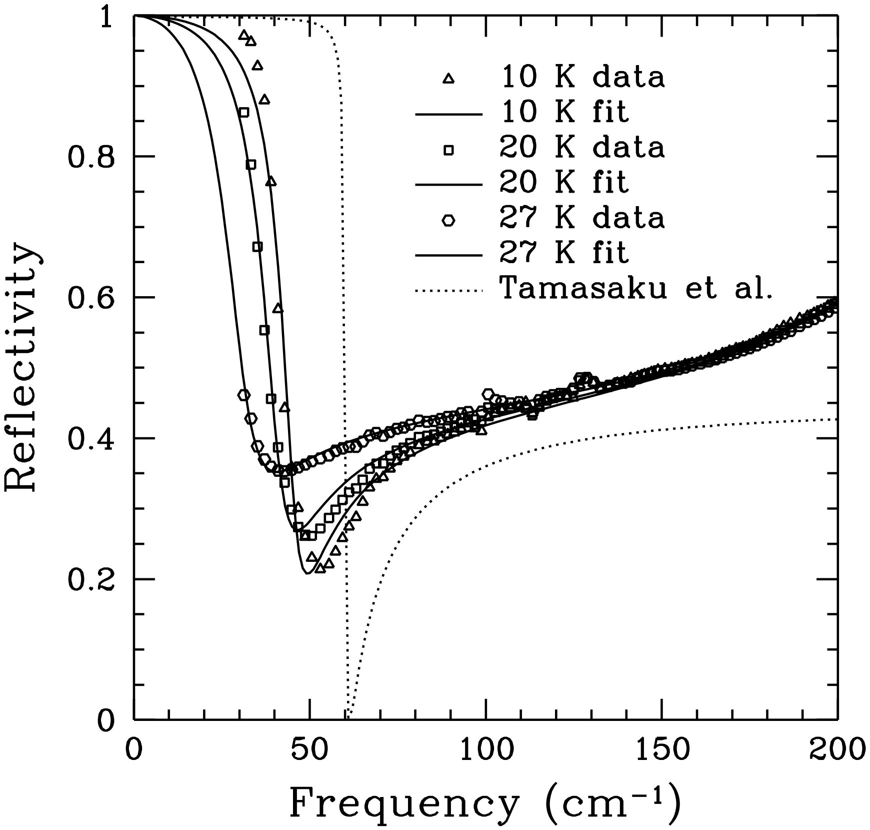

Figure 4.4: *The low-frequency c-axis reflectivity of* $La_{1.85}Sr_{0.15}CuO_4$ *at 10, 20, and 27 K along with the fitted curves at each temperature. The fitted curve of Tamasaku* et al. *for their 8 K data it also shown in dotted line.*

and $\sigma_n(31 \text{ K}) = 6.7\ \Omega^{-1}\text{cm}^{-1}$, will be discussed in section 4.3 (see Fig. 4.10).

4.2.4 Kramers-Kronig Analysis

Based on our fitting results for the reflectivity spectra, the low-frequency extrapolations for the reflectivity were made with the two-fluid model as explained in the previous section. The low-frequency behavior of $1 - R$ changes from ν^2 in the superconducting state to the Hagen-Rubens behavior $\sqrt{\nu}$ in the normal state. Therefore the following dielectric function was used for the extrapolation:

$$\epsilon(\nu) = \tilde{\epsilon}_\infty \left[1 - \frac{\tilde{\nu}_\phi^2}{\nu(\nu + i0^+)} - \frac{\tilde{\nu}_p^2 - \tilde{\nu}_\phi^2}{\nu(\nu + i\gamma)}\right] \tag{4.5}$$

where $\tilde{\nu}_p$ is the screened plasma frequency in the normal state. Fig. 4.5 shows the conductivity at various temperatures derived from the subsequent Kramers-Kronig analysis. The large value of γ in comparison with the pair-breaking energy scale $3.5k_BT_c$ implies that the c-axis infrared response of $La_{1.85}Sr_{0.15}CuO_4$ belongs to the dirty limit. However, from the conductivity spectra it is quite difficult to identify a clear BCS-like gap. It may be that the order parameter in high-T_c superconductors exhibit d-wave symmetry, in which case we would not expect a complete suppression of the conductivity. If the BCS theory is valid for $La_{1.85}Sr_{0.15}CuO_4$ and even if the material belongs to the dirty limit, the gap will be very difficult to identify because of the strong phonon oscillator strength(at 241 cm^{-1}) which extends to the expected gap energy, and also because the electronic contribution to the conductivity itself is rather small. Therefore whatever spectral feature may appear due to opening of the gap will be masked and quite weak.

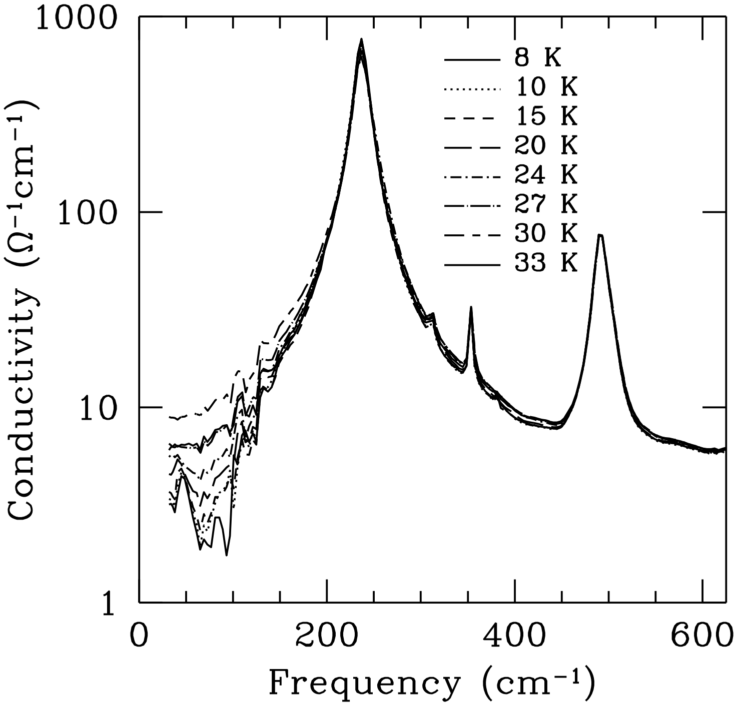

Figure 4.5: *The c-axis conductivity of* $La_{1.85}Sr_{0.15}CuO_4$.

In Fig. 4.6 and Fig. 4.7 we display the real part of the dielectric function ϵ_1 and the loss function Im(-1/ϵ) of $La_{1.85}Sr_{0.15}CuO_4$, respectively, for various temperatures. Notice that the real part of the dielectric function ϵ_1 only has a zero crossing (above T_c) for the TO phonon modes, not for the electronic contribution (overdamped plasmon in the normal state). But as soon as we go below T_c, a zero crossing occurs and it moves to higher energy with decreasing temperature (Fig. 4.6). The presence of the plasma edge is quite apparent in the loss function, the peaks of which correspond to the longitudinal excitation (Fig. 4.7).

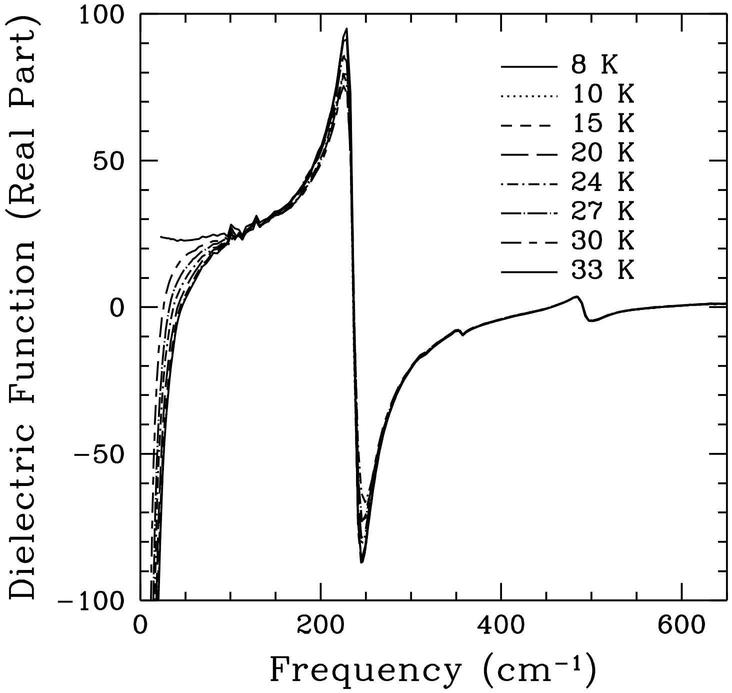

Figure 4.6: *The real part of the c-axis dielectric function of* $La_{1.85}Sr_{0.15}CuO_4$.

4.3 Discussion

4.3.1 Electron Transport: The Crossover Regime

We can treat the cuprate material as a stack of alternating layers consisting of a two dimensional electron gas (confined to the CuO_2 planes) and insulating layers. All the CuO_2 planes are weakly coupled in the normal state and in the superconducting state. The material anisotropy and the coupling between the CuO_2 planes is introduced via the effective mass m_c^* [27]. However this approach breaks down when $\xi^c(0) < d^c$. For $La_{1.85}Sr_{0.15}CuO_4$ $\xi^c(0) = 3$ Å and $d^c = 6.6$ Å and for $Tl_2Ba_2CuO_6$ $\xi^c(0) = 2$ Å $d^c = 11.5$ Å [28]. Therefore it is questionable as to whether this approach can be applied. The anisotropy not only varies

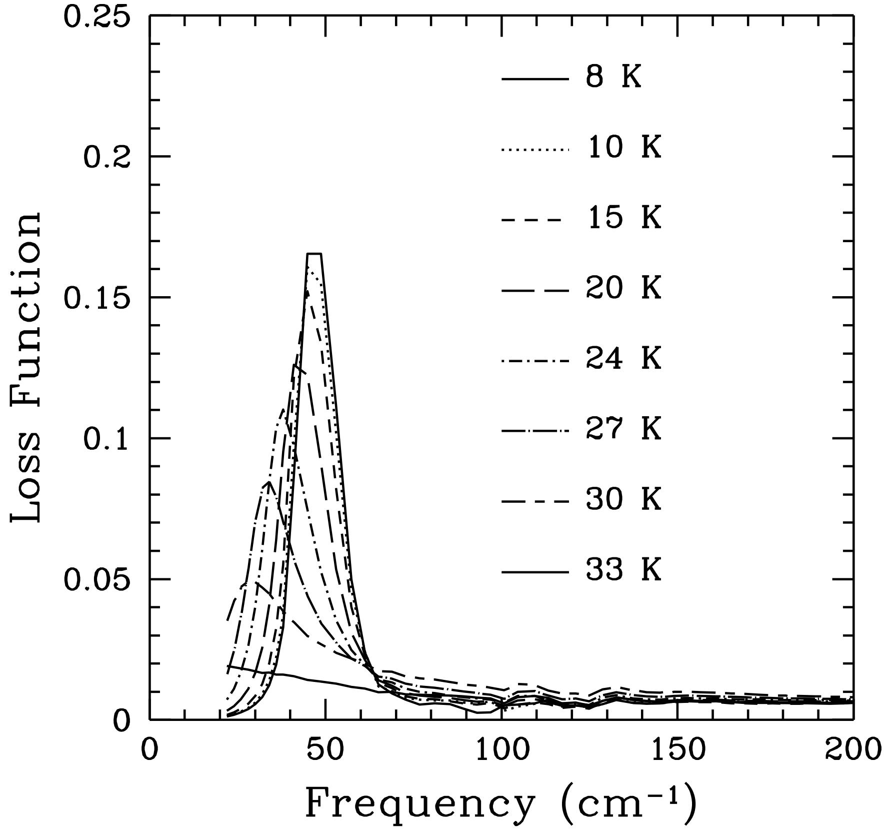

Figure 4.7: *The c-axis loss function of* $La_{1.85}Sr_{0.15}CuO_4$.

amongst the various cuprate materials but is also depends upon the doping concentration. Considering $\mathrm{La}_{2-x}\mathrm{Sr}_x\mathrm{CuO}_4$: The anisotropy ratio decreases as the doping x is increased. Based upon resistivity measurements of Ref. [1] ρ^c/ρ^{ab} = 1500 (x=0.1), 1000 (x = 0.15) and 500 (x = 0.20). The ab-plane resistivity of $\mathrm{La}_{1.85}\mathrm{Sr}_{0.15}\mathrm{CuO}_4$ consistently decreases with decreasing temperature, the gradient remains positive. In contrast the resistivity ρ^c shows a semiconductor like upturn as the temperature is decreased, with $d\rho^c/dT$ becoming negative. As the strontium doping is increased from 0.15 to 0.2 the upturn in ρ^c decreases, until for Sr= 0.25 the resistivity has a continuous positive gradient. This suggests that the charge dynamics in the c direction crosses over from incoherent to coherent. The minimum value of conductivity to satisfy the Mott-Ioffe limit for a material to be considered a metal, is σ^c_{MIL} = 100 $(\Omega\ \mathrm{cm})^{-1}$. At T = 40K this is satisfied for doping above Sr = 0.25 . This means that for underdoped and optimally doped samples, the normal state transport is incoherent and is due to electron hopping, phonon/impurity assisted hopping [29]. Below T_c, the c-axis transport consists of Cooper pairs tunnelling and single quasiparticles tunnelling or hopping between CuO_2 planes. This latter point is applicable when the symmetry of the order parameter is d-wave and so the value of the gap (and so the binding energy) depends upon the wavevector. It is interesting to note that the value of Sr doping

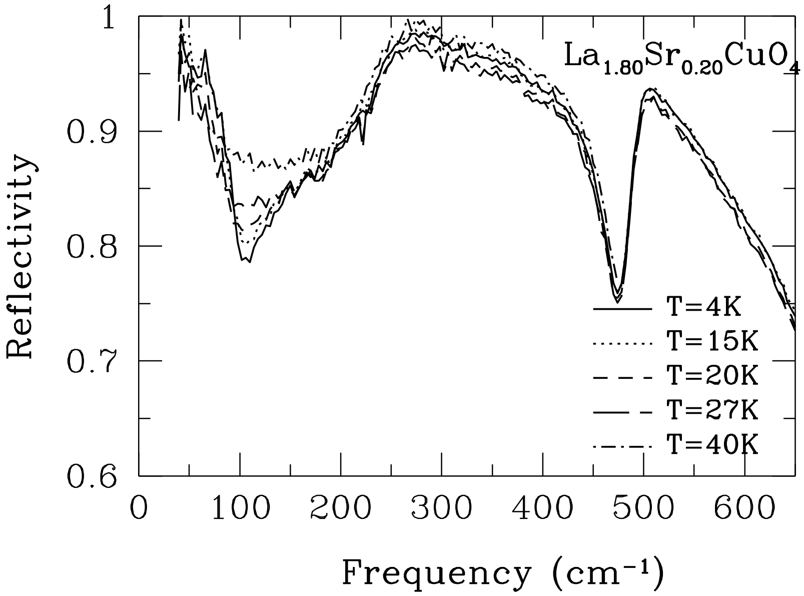

Figure 4.8: *Temperature dependent reflectivity of* $La_{1.80}Sr_{0.20}CuO_4$ *using s-polarized light and an angle of incidence of 80°.*

for $La_{2-x}Sr_xCuO_4$, at which σ_1^c satisfies the Mott-Ioffe condition, the material is no longer a superconductor as shown in the phase diagram in Ref. [30]. Considering only single layer HTSC compounds, T_c varies from 32K ($La_{1.85}Sr_{0.15}CuO_4$) to 85K ($Tl_2Ba_2CuO_6$). Both of these compounds have a single CuO_2 plane yet their critical temperatures T_c are different by almost a factor of three. It would therefore appear that the c-axis electronic properties determine T_c.

Fig. 4.8 shows the c-axis reflectivity of $La_{1.80}Sr_{0.20}CuO_4$ measured using s-polarized light at an angle of incidence of 80°. These measurements were performed immediately after the p-polarized measurements described in chapter 3, simply by

rotating the motorised polarizer. From the Fresnel equations, r_s increases with an increasing angle of incidence, which explains why the reflectivity is so high. However the plasma edge is clearly visible below T_c, it's frequency having increased to 100 cm^{-1} from 50 cm^{-1} for the optimally doped sample. Otherwise there are no dramatic changes in the reflectivity spectrum above and below T_c. The plasma edge at 100 cm^{-1} which occurs in the overdoped sample, is no longer a sub-gap collective excitation, if one would assume the BCS relationship giving $2\Delta = 82$ cm^{-1}. As the plasmon is a collective excitation of Cooper pairs, the superconducting gap must be larger than 100 cm^{-1}.
The lower panel of Fig. 4.9 shows the optical conductivty $\sigma_1(\omega)$ of $La_{1.80}Sr_{0.20}CuO_4$ obtained by fitting the reflectivity curves. The upper panel of Fig. 4.9 also shows $\sigma_1(\omega)$ for the optimally doped sample, replotted in order to make the comparison with the overdoped sample easier. For the optimally doped sample, at a temperature of 33K (normal state) and using the frequency ω =80 cm^{-1} as a reference value, σ_1^c is of the order of 8 $(\Omega cm)^{-1}$, well below the Mott-Ioffe limit. For the overdoped sample $\sigma_1^c = 40$ $(\Omega\ cm)^{-1}$, this is still below the limit. There is a small upturn in the resistivity curve $\rho^c(T)$ at low temperatures but the gradient $d\rho(T)/dT$ does not change sign, up to the point where superconductivity occurs. For the optimally doped sample, between 33 and 300K the conductivity barely changes. This is not the temperature behaviour we would expect for a metal. Considering the overdoped sample, the conductivity successively decreases as we would expect for a metal. Fig. 4.9 shows that the c-axis charge dynamics undergoes a considerable change in going from the optimally to the overdoped doped regime. However as $\sigma_1^c(\omega)$ becomes more like a metal, T_c decreases until at a doping of Sr=0.22 the material is no longer a superconductor. It appears that metallic conductivity in the c direction and a high critical temperature are mutually exclusive.

4.3.2 The c-Axis Plasma Frequency

In section 4.2.2 it was observed that the c-axis plasma frequency (ν_p), defined as $\sqrt{(4/\pi)\int_0^W \sigma_1(\nu)d\nu}$ with W a suitably chosen cut-off frequency, is at least 0.15 eV. Although the energy-momentum dispersion obtained from LDA band structure calculations do not correspond quantitatively (or in the present case not even qualitatively) to the single-particle excitation spectra, the value of the single-electron interlayer hopping matrix elements following from such a calculation is, as a rule, quite accurate (because it is a ground-state property). It is reasonable to assume that the lower limit of 0.15 eV for ν_p using the f-sum rule is a measure of the plasma frequency as would follow from a band structure calculation where many-body effects are ignored. As the integration should end

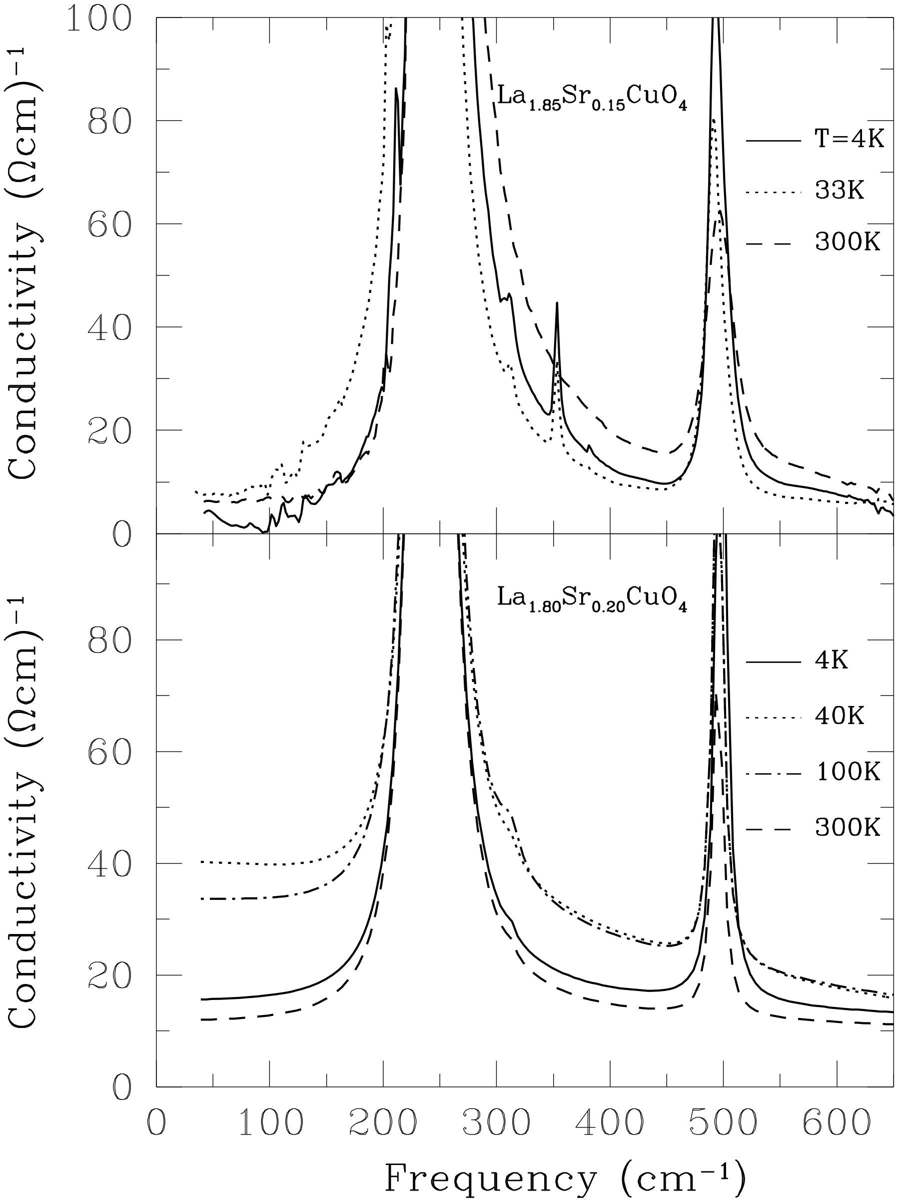

Figure 4.9: *c-Axis optical conductivity of* $La_{1.85}Sr_{0.15}CuO_4$ *and* $La_{1.80}Sr_{0.20}CuO_4$.

below the onset of interband transitions, but at an energy above the highest frequency of the intraband conductivity, an appropriate cut-off frequency W in the integration may not always be available.

To check the above result we calculated the plasma frequency as a function of momentum within the random phase approximation (RPA), using the $E(\vec{k})$ dispersion of La_2CuO_4 calculated within the self-consistent augmented-spherical-wave (ASW) approximation [31]. The Fermi-surface following from LDA band structure calculation is roughly a rectangular tube, oriented along the c direction, with the corners of the rectangle near the $(\pi, 0)$ saddle points. There is a clear corrugation of the tube in the c direction. Without such a corrugation the Fermi surface would be ideally two-dimensional, and the material would resemble a layered electron gas with a plasma dispersion obeying $\omega_p(\vec{k}) = \omega_{p\|} k_\| / \sqrt{k_\|^2 + k_\perp^2}$ for $|\vec{k}| \to 0$ [32] where $\omega_{p\|}$ is the in-plane plasma frequency and $k_\|$ and $k_\perp$ are, respectively, the in-plane and out of plane momenta. Note that in this case $\omega_{p\|}/\omega_{p\perp} \to \infty$. On the other hand, LDA/RPA calculations give a bare ab-plane plasma frequency of about 4 eV, and a bare c-axis plasma frequency of 0.7 eV. After correcting for the 'background' these correspond to 2 eV for the ab-plane plasmon (well above the onset of the interband electron-hole continuum at 0.5 eV), and 0.35 eV for the c-axis plasmon (below the interband electron-hole continuum). We then expect the ab-plane plasmon to be Landau-damped while the c-axis plasmon is not.

It is an important result that experimentally the situation *vis á vis* Landau damping is reversed. The ab-plane dielectric function shows a clear plasma pole that is observed near 1 eV [33], whereas the c-axis plasmon is completely overdamped in the normal state. If the plasma frequency in the ab plane is calculated using the f-sum rule, e.g by integrating the in-plane conductivity up to 1.5 eV, the result is approximately 4 eV , which is now in good agreement with the bare plasma frequency obtained from the LDA/RPA calculation. Therefore we can conclude that, although the f-sum rule provides us with in-plane and out-of-plane bare plasma frequencies reasonably close to estimates based on a simple band-structure approach, the plasma frequency and the frequency dependence of $\sigma_1(\nu)$ in both directions differ quantitatively and qualitatively from what is predicted by such a calculation. The question of damping remains, but the discrepancy could be due to ignoring the strong electron-electron correlations in high-T_c superconductors which is responsible for a metal-insulator transition at a relatively low doping level. Further theoretical considerations which address these issues will be given in subsection 4.3.5.

4.3.3 Conductivity and Superfluid Density

Let E_g^* be the *effective* value of the gap, or gap distribution. We will assume $E_g^* = 3.5k_BT_c$, which becomes exact in the limit of a weak coupling s-wave superconductor. In the superconducting state one should make a distinction between the high and low frequency parts of the spectrum, i.e., far above and below E_g^* ($\approx$ 80 cm^{-1} for $\mathrm{La_{1.85}Sr_{0.15}CuO_4}$). The former remains relatively unaffected by the superconducting transition, whereas for the latter range of frequencies we expect to find a temperature dependence in both the real and imaginary parts of the electronic contribution to the conductivity. For example, for an isotropic s-wave BCS superconductor we expect a decrease of $\sigma(\nu)$ for $\nu \approx E_g^*/2$ as indicated in Fig. 4.10 (lower panel: chained curve). In addition there may be strong decrease of γ for $T < T_c$ as has been reported for the in-plane infrared [34, 35] and microwave [36] response of high-T_c superconductors, and for the c-axis infrared response of $\mathrm{La_{2-x}Sr_xCuO_4}$ [3].

Also shown in Fig. 4.10 are the results of model calculations for the dirty limit of s-wave [37] and d-wave [38] superconductors, assuming standard ratios of E_g^*/T_c for these two models, and assuming a temperature independent scattering rate. The conductivity was calculated for $\nu = 50$ cm^{-1}. This frequency is close both to BCS gap energy $3.5k_BT_c = 82$ cm^{-1} and to the gap value deduced from neutron scattering measurements [39]. As a result, for the s-wave model a steep drop of σ_1 occurs for $T < T_c$, and a kink at the temperature where $E_g(T) = h\nu$. If we would assume that in addition there is a drop of the scattering rate γ below T_c then the conductivity would first increase, but, when γ reaches the gap energy, it would decrease rapidly. Depending on the rate of decrease in γ this peak can be extremely narrow. Therefore when we assume a sudden reduction of γ below T_c, as done by Tamasaku *et al.*, the theoretical conductivity curves would have an even steeper temperature dependence with a peak directly below T_c. For this reason we attribute the decrease of σ_s for $T < T_c$ exclusively to the opening of a gap, i.e. without assuming a change of the electronic scattering rate. For d-wave pairing the calculated temperature dependence of the conductivity σ_s is smooth and is quite close to the experimentally determined values.

For the ratio $\sigma_s(T)/\sigma_n(T)$ a reasonable agreement exists with the d-wave model, whereas there is poor agreement with the s-wave model. For the normalized superfluid fraction $f_s(T) = (\tilde{\nu}_\phi(T)/\tilde{\nu}_\phi(0))^2$ the situation is reversed: f_s follows roughly the $1-(T/T_c)^4$ law, which differs strongly from the d-wave pairing curve, and lies somewhat above the s-wave pairing curve. The inconsistency with the d-wave curve can be removed if the strongly incoherent nature of the transport in the c direction is taken into account [23]. Recently Graf *et al.* [23] calculated the dynamical properties of a stack of two-dimensional d-wave superconductors along the c direction assuming that the hopping between planes occurs only due

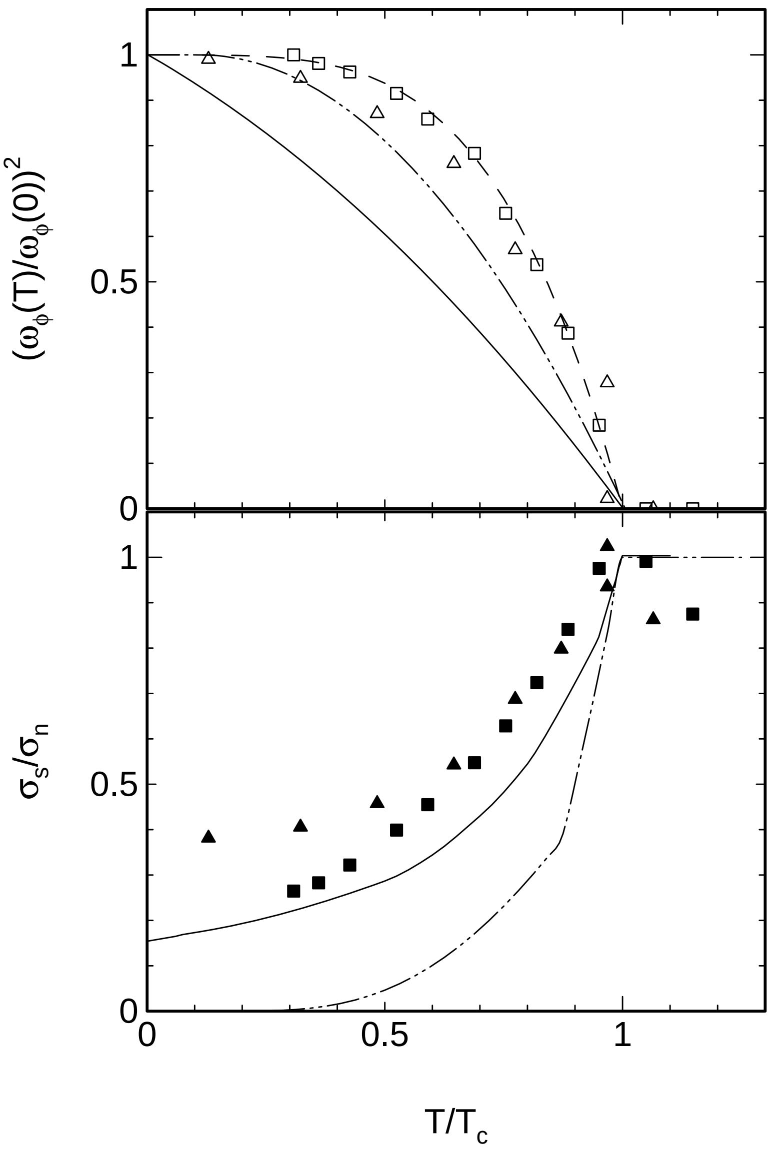

Figure 4.10: *The temperature dependence of* $\tilde{\nu}_\phi^2$ *(upper panel) and* σ_n *(lower panel) corresponding to the fits in Fig. 4.3. Squares: sample 1 with a constant* $\tilde{\epsilon}_\infty$*. Triangles: sample 2 with full frequency dependence of phonon oscillators included in* $\tilde{\epsilon}_\infty$*. Dashed curve:* $1-(T/T_c)^4$*. Chained curves: s-wave case simulations of superfluid fraction(upper panel) and the conductivity ratio* $(\sigma_s/\sigma_n$*(lower panel). Solid curves: d-wave case simulations of superfluid fraction(upper panel) and the conductivity ratio* (σ_s/σ_n)*(lower panel). The simulations of the conductivity ratios are at* $\nu = 50$ *cm*$^{-1}$*.*

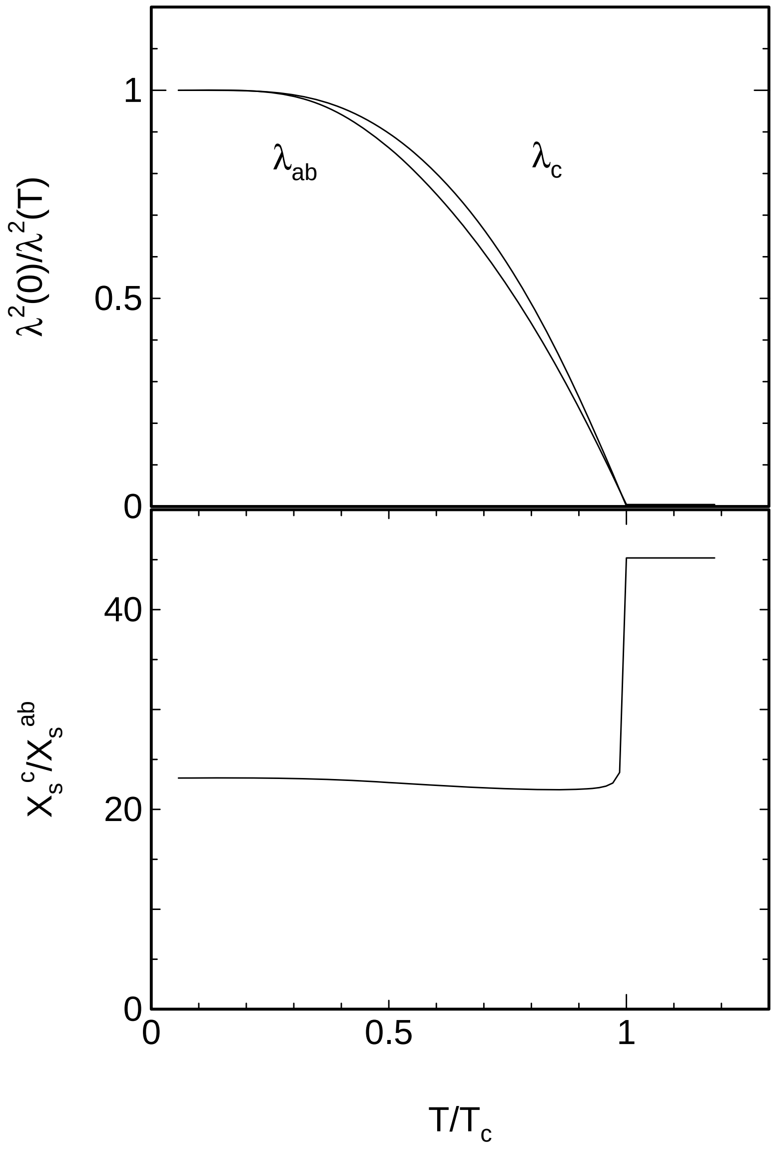

Figure 4.11: *Upper panel: The temperature dependence of* $\lambda_{ab}^2(0)/\lambda_{ab}^2(T)$ *and* $\lambda_c^2(0)/\lambda_c^2(T)$ *calculated using the BCS model. For* $\vec{E} \parallel \vec{c}$ *the following Drude parameters were used* $\epsilon_\infty = 25$, $\nu_p = 1200$ *cm*$^{-1}$, *and* $\gamma = 4500$ *cm*$^{-1}$. *For* $\vec{E} \perp \vec{c}$ *we used* $\epsilon_\infty = 5$, $\nu_p = 6000$ *cm*$^{-1}$, *and* $\gamma = 50$ *cm*$^{-1}$. *Lower panel: the temperature dependence of the anisotropy of the surface reactance* X_s^c/X_s^{ab}.

to scattering at impurity sites. The temperature dependence of f_s was found to be of the Ambegaokar-Baratoff type [40, 41], i.e., much closer to the experimental results.

Based on the clean-limit parameters of Ref. [3], Shibauchi *et al.* [17] could not explain their penetration depth data using a three-dimensional model. To illustrate how the anisotropy of $\sigma_1(\nu)$ influences the penetration depth, we calculated the *ab*-plane and the *c*-axis penetration depths, as well as the surface reactance assuming clean-limit parameters for the *ab*-plane and dirty limit parameters for the *c* axis. Since the symmetry of the order parameter is not expected to be critical for the illustration of this particular point, we assumed *s*-wave pairing. The difference in behavior for both directions arises from the fact that in the dirty limit the *c*-axis penetration depth follows the Ambegaokar-Baratoff expression. As can be seen in Fig. 4.11, the jump in the anisotropy of the surface reactance $X^c(T)/X^{ab}(T)$ [17] and the difference between λ_{ab} and λ_c follows naturally from this analysis with the anisotropy of $\sigma_1(\nu)$ properly taken into account.

4.3.4 Classification of Infrared Response of Superconductors

In recent years it has become clear that it is the c-axis structure and electronic transport properties that determine T_c [29]. The HTSC cuprates have one, two or three CuO_2 planes per unit cell. This makes for a bewildering number of combinations of $J_\perp$ (spin exchange coupling energy in the c direction) and $V_\perp^{coulomb}$ (Coulomb coupling energy between planes) within each unit cell and between two adjacent unit cells. In an attempt to classify and understand the large range of values of T_c, the ratio of the c-axis coherence length $\xi^c(0)$ at T = 0K to the c-axis distance between two CuO_2 planes d^c was considered as a criterion for determining whether a HTSC was an anisotropic three dimensional metal or a stack of weakly coupled Josephson junctions. The following criteria were used in the above reference:

- $\xi^c(0)/d^c < 0.17$: weakly coupled Josephson Junction (JJ)
- $0.17 < \xi^c(0)/ d^c < 0.38$: crossover regime
- $\xi^c(0)/ d^c > 0.38$: three dimensional anisotropic metal

The table 4.1 shows into which category the various HTSC's fit into according to the above criteria.

However the c-axis coherence length increases with temperature according to:

$$H_{c2}(T) = \frac{1}{\xi^2(T)}\frac{\Phi_0}{\pi} \tag{4.6}$$

Therefore at T= 0 K , if the material is considered a weakly coupled Josephson Junction, then near T_c the coherence length $\xi^c(T)$ will increase and it should become a three dimensional anisotropic metal. This would mean a shift or a disappearance of the Josephson plasma frequency ω_J (ϵ_1, ϵ_2 will change), at this temperature T^* which is below T_c. To date such an effect has not been reported. Applying the above criteria to $La_{1.85}Sr_{0.15}CuO_4$ we have a three dimensional anisotropic metal in the superconducting state at 0K and near T_c.

Material	T_c(K)	ξ^c (Å)	d^c (Å)	ξ^c/d^c
$Bi_2Sr_2CaCu_2O_8$	89	< 0.5	12.3	< 0.06
$Tl_2Ba_2CuO_6$	82	2	11.5	0.17
$Tl_2Ba_2CuO_{6+\delta}$	65	2	11.5	0.17
$La_{1.89}Sr_{0.11}CuO_4$	27	3	6.6	0.43
$YBa_2Cu_3O_7$	92	3.2	8.2	0.38
$NbSe_2$	7	30	6	5

Table 4.1: Coherence length ξ^c and c-axis distance d^c for various superconductors.

Impurities, Disorder and Defects

Due to the complexity of HTSC 's it is difficult to measure the exact dopant concentration. The Sr concentration in $La_{2-x}Sr_xCuO_4$ is measured by titration or microprobe analysis. Whilst these technique are the best available they still only give macroscopic results, not microscopic values. The crystallinity is determined by the X ray diffraction peak width. There is a certain threshold value of second phase material or inhomogeneities before this is registered in the spectra. The materials are thermodynamically unstable during the crystal growth phase, there will inevitably be non-uniformities in the chemical composition within the boule. For example in $La_{2-x}Sr_xCuO_4$, the CuO_2 plane consists of an octahedral structure with two apical oxygen atoms at the top and bottom apex. There are many combinations which constitute a defect/disorder such as one oxygen atom is missing from the apical oxygen site or in the base plane which will change the doping locally and the physical structure such as the tilting angle of the octahedra.

It is known that impurities depress T_c if the pairing symmetry is d-wave. If we compare the critical temperature and the resistivity ρ for $La_{2-x}Sr_xCuO_4$ crystals grown (by the same group) in 1991 to those grown in 1996 there is a difference in absolute values of ρ and of T_c, for the same doping. In 1991, the critical temperature T_c for optimally doped $La_{1.85}Sr_{0.15}CuO_4$ was 25K [42]. In 1996, this value was increased to 37K [43]. In 1991 the reported resistivity for $La_{1.80}Sr_{0.20}CuO_4$

was $\rho^{ab}(50K) = 2.13\ 10^{-4}$ (Ω cm) [44]. In 1996 $\rho^{ab}(50K)$ was reduced to 0.53 10^{-4} (Ω cm) [43] which is a reduction by a factor of four.

Comparison of Pb and the Cuprates

A classical superconductor such as Pb is usually described within the Mattis-Bardeen theory for a dirty superconductor. For Pb the pair breaking energy is $2\Delta = 16$ cm^{-1}, γ =28 cm^{-1}, T$_c$ =7K and the penetration depth λ_L=30 nm [45]. In this case $2\Delta < \gamma$, therefore Pb is in the dirty limit. The superconducting plasma frequency is about 10^5 cm $^{-1}$ which is far above the gap value of 16 cm^{-1}. Consequently we are unable to observe this as an oscillation of the Cooper pairs. At this photon excitation energy there are only single quasiparticles. There are three main energy scales which describe a classical isotropic superconductor: (1) The pair breaking energy 2Δ, (2) the plasma frequency $\tilde{\nu} = \nu/\sqrt{\epsilon_\infty}$ which is reduced in value due to screening and possibly due to phonon contribution and (3) the scattering rate γ. The previous example of Pb may be defined by the inequality $2\Delta < \gamma$. Considering $La_{1.85}Sr_{0.15}CuO_4$ this is no longer an isotropic material but an anisotropic material where the ab-plane is in the clean limit picture namely $\gamma < 2\Delta < \nu_p$. However the c-axis conductivity is strongly in the dirty limit picture in that $2\Delta << \gamma$ and ν_p is overdamped in the normal state. But in the superconducting state there is a plasma oscillation below the energy gap 2Δ. Three other HTSC's materials have shown a sub-gap plasma oscillation in the superconducting state. For $Bi_2Sr_2CaCu_2O_8$ (T$_c$ = 85K) ν_{pl}=5 cm^{-1} [14], for $Nd_{1.85}Ce_{0.15}CuO_4$ (T$_c$ = 23K ν_{pl} =7 cm^{-1} [46] and for under doped $YBa_2Cu_3O_{7-\delta}$ ν_{pl} = 80 - 200 cm^{-1} depending upon the doping [6].

$La_{1.8}Sr_{0.20}CuO_4$ has a superconducting plasma edge frequency (ν_{pl}) at 100 cm^{-1} , this is far larger than the measured value for any of the other single layer cuprate. For a doping value of Sr = 0.22, not only is T$_c$ = 0K but there is no superconducting plasma edge (see chapter 1 Fig. 1.2) [30]. This confirms the direct link between the superconducting state and the plasma edge. Another interesting point is that compared to the optimally doped sample, for the overdoped sample T$_c$ decreases to 29K but the plasma edge ν_{pl} increases to 100 cm^{-1} i.e. T$_c$ has decreased by 3K but the plasma frequency has doubled. Therefore there cannot be a direct relationship of proportionality between T$_c$ and ν_{pl}. The plasma edge frequency for the overdoped sample is at 100 cm^{-1} which is above the BCS gap value of 3.5kT$_c$ = 74 cm^{-1}. This is direct experimental evidence that the weak coupling value of 3.5 in the BCS relationship 3.5kT$_c$ = 2Δ is not valid for the c-axis of the overdoped compound $La_{1.8}Sr_{0.20}CuO_4$. For the optimally doped compound this cannot be said as the plasma edge occurs at 50 cm^{-1} and 2Δ = 82 cm^{-1}.

4.3.5 Microscopic Considerations

Here some theoretical considerations are given as to the origin of the strong damping along the c axis, which is responsible for the absence of the c-axis plasma edge in the normal state and for the reduction of the c-axis conductivity in the superconducting state. In the case of $La_{1.85}Sr_{0.15}CuO_4$, we can argue that the replacement of La^{3+} ions with Sr^{2+} ions in 15 % of the unit cells provides the necessary disorder. In principle it is possible to construct a potential landscape that is largely translation-invariant along the planes with the translational symmetry broken in the c direction, which leads to states localized in the c direction while remaining itinerant in the planar direction. Such a construction does not arise in a natural way from random substitution of La with Sr. Moreover the absence of a c-axis plasma edge above T_c and the reduction of the c-axis plasma frequency are also observed in fully doped $YBa_2Cu_3O_7$ [47] in which the Cu-O chains are presumably well ordered and the c-axis transport data shows T-linear temperature dependence of resistivity. Hence a broad and featureless $\sigma_1(\nu)$ in the c direction appears to be a *generic feature* of the high-T_c cuprate superconductors, which implies that this is a fundamental property of these materials.

Also our observation shows no signature of a large mass renormalization, which seems to contradict the notion of strongly renormalized Fermi-liquid behavior. On the other hand, the featureless line-shape of $\sigma_1(\nu)$ up to at least 0.5 eV demonstrates that there is no energy scale below which Fermi-liquid behavior sets in.

The aforementioned experimental observations can be explained within the framework of the theory of superconductivity based on the interlayer tunneling mechanism [48, 21, 2] by Anderson and co-workers. In this theory the single-particle tunneling between the planes is suppressed due to the formation of a Luttinger liquid state. As a result the dominant transport mechanism in the superconducting state is Josephson-type pair tunneling. Our observation that the dynamical conductivity at frequencies larger than the pair breaking energy of order $4k_BT_c$ remains basically unaffected by the superconducting phase transition, must then imply that the transition to the superconducting state only affects the dynamical properties of ground-state up to an energy scale of order $4k_BT_c$. The implication seems to be, that if the normal state is a Luttinger liquid, in the superconducting state dynamical properties of Fermi-liquid type are only restored up to frequencies of about $4k_BT_c$.

4.4 Conclusions

The absence of a c-axis plasmon in the normal state of $La_{1.85}Sr_{0.15}CuO_4$ results from an anomalously strong damping of the transport perpendicular to the CuO_2

planes. The decrease in the c-axis conductivity for $T < T_c$ can be fully accounted for by the opening of a gap, the presence of which is a necessary consequence of the f-sum rule. There is no indication for a sudden decrease of the optical scattering rate for $\vec{E}//\vec{c}$ when $T < T_c$. The electronic transport along the c-axis is incoherent and well below the Mott-Ioffe limit of conductivity for the optimally doped sample $La_{1.85}Sr_{0.15}CuO_4$. For the overdoped sample the conductivity remains below Mott-Ioffe limit but the normal state value of σ_1 (T = 40K) increases by a factor of five. The Mott-Ioffe limit is met for $La_{1.75}Sr_{0.25}CuO_4$, but for single crystal material it is no longer a superconductor. It appears that coherent c-axis transport and superconductivity are mutually exclusive.

References

[1] Y. Nakamura and S. Uchida, Phys. Rev. B. **47**, 8369 (1993).

[2] P. W. Anderson, Science **268**, 1154 (1995).

[3] K. Tamasaku, Y. Nakamura, and S. Uchida, Phys. Rev. Lett. **69**, 1455 (1992).

[4] M. Inui and S. Doniach, Phys. Rev. B **41**, 6668 (1990).

[5] T. M. Mishonov, Phys. Rev. B **44**, 12033 (1991).

[6] C. C. Homes, T. Timusk, R. Liang, D. A. Bonn, and W. N. Hardy, Phys. Rev. Lett. **71**, 1645 (1993).

[7] U. Walter, M. S. Sherwin, P. L. Richards, and A. Zettl, Phys. Rev. B **35**, 5327 (1987).

[8] P. E. Sulewski, A. J. Seevers, S. E. Russek, H. D. Hallen, D. K. Lathrop, and R. A. Buhrman, Phys. Rev. B **35**, 5330 (1987).

[9] Z. Schlesinger, R. L. Greene, J. G. Bednorz, and K. A. Müller, Phys. Rev. B **35**, 5334 (1987).

[10] D. A. Bonn, J. E. Greedan, C. V. Stager, T. Timusk, M. G. Doss, S. L. Herr, K. Kamarás, C. D. Porter, D. B. Tanner, J. M. Tarascon, W. R. McKinnon, and L. H. Greene, Phys. Rev. B **35**, 8843 (1987).

[11] Z. Schlesinger, R. T. Collins, M. W. Shafer, and E. M. Engler, Phys. Rev. B **36**, 5275 (1987).

[12] M. S. Sherwin, P. L. Richards, and A. Zettl, Phys. Rev. B **37**, 1587 (1988).

[13] S. Tajima, G. D. Gu, S. Miyamoto, A. Odagawa, and N. Koshizuka, Phys. Rev. B **48**, 16164 (1993).

[14] O. K. Tsui, N. P. Ong, and J. B. Petersen, Phys. Rev. Lett. **76**, 819 (1996).

[15] M. Bauer, Ph.D. thesis, University of Tübingen, 1990.

[16] D. N. Basov, T. Timusk, B. Dabrowski, and J. D. Jorgensen, Phys. Rev. B **50**, 3511 (1994).

[17] T. Shibauchi, H. Kitano, K. Uchinokura, A. Maeda, T. Kimura, and K. Kishio, Phys. Rev. Lett **72**, 2263 (1994).

[18] P. W. Anderson, Science **235**, 1196 (1987).

[19] F. C. Zhang and T. M. Rice, Phys. Rev. B **37**, 3759 (1988).

[20] M. J. Rice and Y. R. Wang, Phys. Rev. B **48**, 12921 (1993).

[21] D. G. Clarke, S. P. Strong, and P. W. Anderson, Phys. Rev. Lett. **72**, 3218 (1994).

[22] S. Chakravarty and P. W. Anderson, Phys. Rev. Lett **72**, 3859 (1994).

[23] M. J. Graf, D. Rainer, and J. A. Sauls, Phys. Rev. B **47**, 12098 (1993).

[24] A. G. Rojo and K. Levin, Phys. Rev. B **48**, 16861 (1993).

[25] V. H. M. Duijn, N. T. Hien, A. A. Menovsky, and J. J. M. Franse, Physica C **235**, 559 (1994).

[26] D. van der Marel, M. Bauer, E. H. Brandt, H.-U. Habermeier, D. Heitmann, W. König, and A. Wittlin, Phys. Rev. B **43**, 8606 (1991).

[27] Lawrence and Doniach, 12 Intl. Conf. on Low Temp. Physics ed. E. Kanda 361 (1971).

[28] N. E. Hussey, J. R. Cooper, R. A. Doyle, C. T. Lin, W. Y. Liang, and D. C. Sinclair, Phys. Rev. B **53**, 6752 (1996).

[29] S. L. Cooper and K. E. Gray, *Physical Properties of High Temperature Superconductors Volume 4 ed D. Ginsberg* (World Scientific, Singapore, 1994).

[30] S. Uchida, K. Tamasaku, and S. Tajima, Phys. Rev. B **53**, 14558 (1996).

[31] M. Czyzyk (unpublished).

[32] A. Fetter, Ann. Phys. **81**, 367 (1973).

[33] J. H. Kim, I. Bozovic, J. S. H. Jr., W. Y. Lee, C. B. Eom, T. H. Geballe, and E. S. Hellman, Physica C **185-189**, 1019 (1991).

[34] B. Romero, C. D. Porter, D. B. Tanner, L. Forro, D. Mandrus, L. Mihaly, G. L. Carr, and G. P. Williams, Phys. Rev. Lett **68**, 1590 (1992).

[35] M. C. Nuss, P. M. Mankiewich, M. L. O'Malley, E. H. Westerwick, and P. B. Littlewood, Phys. Rev. Lett. **66**, 3305 (1991).

[36] D. A. Bonn, R. Liang, T. M. Riseman, D. J. Baar, D. C. Morgan, K. Zhang, P. Dosanjh, T. L. Duty, A. MacFarlane, G. D. Morris, and Brewer, Phys. Rev. B **47**, 11314 (1993).

[37] D. C. Mattis and J. Bardeen, Phys. Rev. **117**, 912 (1958).

[38] H. Won and K. Maki, Phys. Rev. B **49**, 1397 (1994).

[39] E. Mason, G. Aeppli, and H. Mook, Phys. Rev. Lett **68**, 1414 (1993).

[40] V. Ambegaokar and A. Baratoff, Phys. Rev. Lett. **10**, 486 (1963).

[41] V. Ambegaokar and A. Baratoff, Phys. Rev. Lett. **11**, 104 (1963).

[42] S. Uchida, T. Ido, H.Takagi, T. Arima, Y. Tokura, and S. Tajima, Phys. Rev. B **43**, 7942 (1991).

[43] Y. Fukuzumi, K. Mizuhashi, K. Takenaka, and S. Uchida, Phys. Rev. Lett. **76**, 684 (1996).

[44] T. Ito, H. Takagi, S. Ishibashi, T.Ido, and S. Uchida, Nature **350**, 596 (1991).

[45] E. V. Kose, *Superconducting Quantum Electronics* (Springer-Verlag, Berlin, 1989).

[46] T. W. Noh, S. G. Kaplan, and A. J. Sievers, Phys. Rev. B. **41**, 307 (1990).

[47] J. Schützmann, S. Tajima, S. Miyamoto, and S. Tanaka, Phys. Rev. Lett. **73**, 174 (1994).

[48] S. Chakravarty, A. Sudbø, P. W. Anderson, and S. Strong, Nature **261**, 337 (1993).

5 Excitation of c-Axis LO Modes in Single Layer HTSC's

Of the several theories of HTSC's, the Anderson Interlayer Tunnelling (ILT) model suggests there exists a direct relationship between the c-axis Josephson plasma frequency ω_J *and the critical transition temperature* T_c*. This prediction was tested for various single layer HTSC compounds. We use single layer compounds in order to avoid the complicating effects of intracell coupling. Three compounds were tested for which* T_c *varied between 12K and 85K. For all three compounds only ab in-plane crystals were available, with the c-axis thickness being between 50* μm *and 100* μm*. Yet it is the c-axis plasmon that needs to be probed, consequently the PARIS technique was employed. Reflectivity measurements show that the ILT predicted values of* ω_J *do not agree with measurements for* $Tl_2Ba_2CuO_6$, $Nd_{1.85}Ce_{0.15}CuO_4$ *and* $Bi_2Sr_2CuO_6$*. For these three compounds an upper limit of 100* cm^{-1} *for the unscreened Josephson c-axis plasma frequency can be set or a penetration depth of* $\lambda_L > 15$ μm*. This conclusion has been confirmed by recent SQUID measurements on* $Tl_2Ba_2CuO_6$*.* [1]

5.1 Introduction

No consensus has been reached about the pairing mechanism causing superconductivity in the cuprates. One reason why the mechanism responsible for HTSC

---

[1] Part of this chapter has been published : D. van der Marel, J. Schützmann, H. S. Somal, J. van der Eb Proceedings of 10 th Anniversary of the Discovery of HTSC's, Houston,USA March 1996. J. Schützmann, H. S. Somal, A. A. Tvetkov, D. van der Marel, G. Koops, N. Koleshnikov, Z. F. Ren, J. H. Wang, E. Bruck and A. A. Menovsky. Phy. Rev. B 55, 11118 (1997).

remains unknown is that almost all of the theories put forward contain one or more fitting parameters which allows the model predictions to agree with measurements. In contrast the ILT model proposes a direct relationship between T$_c$ and the interplane pair hopping rate which are quantities which can be measured directly as we shall see in this chapter.

The Chakravarty-Anderson [1] ILT model proposes that in the normal state there is a spin - charge separation in the CuO$_2$ planes, therefore the conductivity in the c-direction is close to zero. In the superconducting state the successive CuO$_2$ planes form a stack of coupled Josephson junctions, so that the Cooper pairs are able to tunnel in the c direction. The ILT model suggests that the reduction in the kinetic energy of the system is equal to the total Josephson energy i.e.

$$E_{cond} = E_J \tag{5.1}$$

Put another way, in the superconducting state there is reduction in energy of the condensate due to delocalization. Shown below are the relevant basic equations. In equilibrium the Josephson coupling energy is given by:

$$E_J = \frac{\hbar J_J}{2e} \tag{5.2}$$

where J$_J$ is the Josephson critical current. The Josephson plasma frequency is given by:

$$(\hbar\omega_J)^2 = \frac{8\pi e\hbar d J_J}{a^2\epsilon^c} \tag{5.3}$$

where a is the in-plane lattice parameter, d is the distance between the CuO$_2$ planes and ϵ^c is the dielectric function in the c direction. E$_{cond}$ for the ILT model is also given by

$$E_{cond} = \frac{1}{2}N(0)\Delta^2 \tag{5.4}$$

where N(0) is the Density of States at the Fermi surface. Re-arranging these equations, eliminating J$_J$, we obtain:

$$(\hbar\omega_J)^2 = \frac{8\pi e^2 d}{a^2\epsilon^c}N(0)\Delta^2 \tag{5.5}$$

Using the BCS relation $2\Delta = 3.5\ k_B T_c$, we obtain [2, 3]:

$$\hbar\omega_J = 2.9 k_B T_c \sqrt{\frac{N(0)}{d\ \epsilon^c}}\frac{1}{a} \tag{5.6}$$

All the parameters on the right hand side of the above equation are known, so that ω_J can be calculated. In chapter 4 the appearance of a plasma edge in the superconducting state was discussed. A direct measurement of ω_J is obtained, assuming this to be the Josephson plasma frequency. It is by comparing the measured value of ω_J with the predicted value, that we can test the ILT model [4]. Implicit in this model is that along the c-direction the material is considered to be a stack of weakly coupled Josephson junctions. This model does not propose a mechanism whereby there is an attractive potential between two electrons i.e. a mechanism for pairing. The proposition is that below T$_c$, the ground state energy is reduced due to delocalization of Cooper pairs. Table 5.1 lists the predicted value of the Josephson plasma frequency ω_J for various single layer HTSC compounds.

Compound	T$_c$(K)	a($\mathring{A}$)	d($\mathring{A}$)	$\hbar\omega_J$(meV)	λ_c(μm)
$Bi_2Sr_2Cu_2O_6$	12	3.86	11.57	30	6.6
$Nd_{1.85}Ce_{0.15}CuO_4$	23	3.95	6.035	43	4.3
$La_{1.85}Sr_{0.15}CuO_4$	32	3.79	6.64	63	3.1
$Tl_2Ba_2CuO_6$	85	3.86	11.57	216	0.91
$Hg_2Ba_2CuO_5$	98	3.86	9.51	225	0.88

Table 5.1 Predictions of ω_J based upon the ILT model.

Of particular interest is $Tl_2Ba_2CuO_6$ which has a critical temperature 2.6 times and an interlayer distance twice that of $La_{1.85}Sr_{0.15}CuO_4$. For all of the above compounds except $La_{1.85}Sr_{0.15}CuO_4$ there are no known measurements of the c-axis optical properties. It is possible to re-write Eqn. 5.3 in a slightly different form:

$$\hbar^2\omega_J^2 = \beta E_{cond}\frac{16\pi d e^2}{a^2\ \epsilon^c} \tag{5.7}$$

where β is the fraction of the condensation energy supplied by the ILT mechanism. From specific heat measurements E$_{cond}$ =80 μeV for $Tl_2Ba_2CuO_6$ (T$_c$=85K) and E$_{cond}$ =13 μeV for slightly underdoped $La_{2-x}Sr_xCuO_4$ (T$_c$=32K) [5]. It is also possible to calculate the Josephson plasma frequency ω_J using the Mattis-Bardeen theory for a superconductor in the dirty limit and the Ferrel-Glover-Tinkham (FGT) sum rule [6]. The result is:

$$\hbar^2\omega_J^2 = \frac{4\pi^2\hbar\sigma_n\Delta(0)}{a^2\ \epsilon^c} \tag{5.8}$$

where σ_n is the normal state conductivity in the c direction and $\Delta(0)$ is the BCS gap value at zero Kelvin. Table 5.2 shows the value of ω_J calculated using the

ILT model and FGT sum rule

Compound	T_c	ω_J(cm $^{-1}$) ILT	ω_J(cm $^{-1}$) FGT
$Tl_2Ba_2CuO_6$	85	1728	200
$La_{1.85}Sr_{0.15}CuO_4$	32	504	230

Table 5.2: Comparison of predicted values of ω_J using the ILT model and the FGT sum rule.

There is a considerable difference in the value of ω_J predicted by the two models. The listed values of ω_J are the unscreened values, whilst the actual zero crossing of ϵ_1 from measurements will be at the screened value $\omega_J/\sqrt{\epsilon_s}$. The value of ϵ_s will depend upon the atomic polarizability and the phonon contribution in this frequency range which is given by the following equation:

$$\epsilon(\omega) = \epsilon_\infty - \frac{\omega_J^2}{\omega^2} + \frac{4\pi\sigma^e}{\omega} + \sum_{i=1}^{n} \frac{S_i\omega_i^2}{\omega_i^2 - \omega^2 - i\omega\gamma} \tag{5.9}$$

where σ^e is the electronic contribution of the complex conductivity and ω_i is the TO frequency of the phonon.

5.2 Experimental Technique

Single crystal samples of $Tl_2Ba_2CuO_6$ (optimally doped T_c=85K), $Tl_2Ba_2CuO_{6+\delta}$ (overdoped T_c=30K), $Bi_2Sr_2Cu_2O_6$ (T_c=12K), $Nd_{1.85}Ce_{0.15}CuO_4$ (T_c=23K) and $La_{1.85}Sr_{0.15}CuO_4$ (T_c=32K) were measured using the PARIS technique (Ref. chapter 3). All the samples were too thin along the c-direction to permit direct access to σ_c using normal incidence reflection. In addition a film of $Tl_2Ba_2CuO_{6+\delta}$ (optimally doped T_c=85K) which had been grown on a $SrTiO_3$ substrate was also measured. The film had a large surface area with dimensions of 4 x 7 mm. The $Tl_2Ba_2CuO_6$ crystals consisted of small platelets of approximately 2 x 2 mm which were glued together with indium to produce a mosaic of sufficient surface area for PARIS measurements. Both the $Nd_{1.85}Ce_{0.15}CuO_4$ and the $La_{1.85}Sr_{0.15}CuO_4$ were single crystals with approximate dimensions of 4 x 4 mm. By using the PARIS technique and having only samples with ab crystal surfaces, reflectivity measurements will probe not just the ab plane properties but also the longitudinal optical (LO) modes of the c-axis which also includes ω_J. Defining the absorptivity A_p = 1 - R_p where R_p is the measured reflectivity using p-polarized light, we can rearrange the Fresnel equations to obtain an expression for the pseudo loss function whose resonances are the LO modes of the c-axis. This is given by the following expression :

$$\frac{A_p\,|n_{ab}|\cos\theta}{2(2-A_p)} \approx Im\left(e^{i\eta}\sqrt{1-\frac{\sin^2\theta}{\epsilon_c}}\right) \tag{5.10}$$

where n_{ab} is the complex refractive index of the ab plane, θ is the angle of incidence and $\eta = \frac{\pi}{2} - Arg(n_{ab})$.

In the normal state the LO modes will appear as peaks in the pseudo loss function. In the superconducting state, if there is a plasmon mode, this will appear as an additional peak. This will be evident if $\omega_J < E^*$ where E^* is the energy gap. It is worth noting that this method does not require a Kramers-Kronig transformation. The samples were mounted on top of a copper cone and measured using the PARIS technique outlined in chapter 3. The samples were Au coated in-situ and the absolute reflectivity obtained. DC resistivity measurements were performed on the $Tl_2Ba_2CuO_6$ (optimally doped) sample by evaporating gold contacts onto the surface and bonding these to external wires. Field cooled and zero field cooled DC magnetic susceptibility measurements were also performed on the same sample (see Fig. 5.1).

5.3 Results

Fig. 5.1 shows the DC resistivity ρ^{ab} (ab-plane) and ρ^c (c-axis) as a function of temperature. The inset shows the DC magnetic susceptibility measured with H $\|$ ab in a field of 10 Oe for the $Tl_2Ba_2CuO_6$ optimally doped sample. From the field cooled and zero field cooled measurements we can determine the superconducting volume of the sample. This is an indirect check of the quality of the sample and ensures that the penetration depth is representative of the bulk. The results show a sharp transition and superconducting volume above 95 %.

$Tl_2Ba_2CuO_6$ has two possible crystallographic forms, tetragonal which is superconducting and orthorhombic which is not. The forms can be distinguished by their ab-plane unit cell dimensions. For the tetragonal structure a = b = 3.9 $\mathring{A}$, c = 23.2 $\mathring{A}$ and for the orthorhombic a $\approx$ b $\approx$ 5.5 $\mathring{A}$, c = 23.2 $\mathring{A}$ [7]. Three small samples of the crystal were taken from three different place on the crystal. X-ray measurements revealed that the material was of the tetragonal phase. The DC resistivity measurements show a linear temperature dependence as reported by other groups [8, 9]. Fig. 5.2 shows R_p for the optimally doped sample of $Tl_2Ba_2CuO_6$ (T_c = 85K), the general magnitude and form is what we would expect for the ab plane properties of a HTSC. The general shape is broken by the LO modes of the c-axis. As the temperature is decreased the reflectivity increases. There are two sharp resonances at 429 and 631 cm^{-1} with a weaker one at 151 cm^{-1}, these are 3 LO phonons associated with the c-axis. Lattice calculations by Kulkarni *et al* [10] predict four c-axis phonons at 143, 348, 451, 648 cm^{-1}. The one at 348 cm^{-1} which is an oxygen bending mode with a large oscillator strength, was not observed. Neither was it observed in the overdoped sample nor in the film measurements. Further, this mode was not observed in oblique angle measurements of $Tl_2Ba_2Ca_2Cu_3O_10$ [11] where it also should have been detected. The two strongly damped modes at 86 and 538 cm^{-1} are close to the ab in-plane modes at 84 and 560 cm^{-1}. They appear only weakly due to screening effects. This becomes apparent by comparing σ_1^{ab} for $La_{1.85}Sr_{0.15}CuO_4$ (ref chapter 3) where the phonons were clearly visible, and the above results at the frequency of 500 cm^{-1} . For $La_{1.85}Sr_{0.15}CuO_4$ σ_1^{ab}(500 cm^{-1}) = 1 kS/cm (T = 40K normal state) whilst for $Tl_2Ba_2CuO_6$ σ_1^{ab}(500 cm^{-1}) = 3.8 kS/cm (T = 100K normal state).

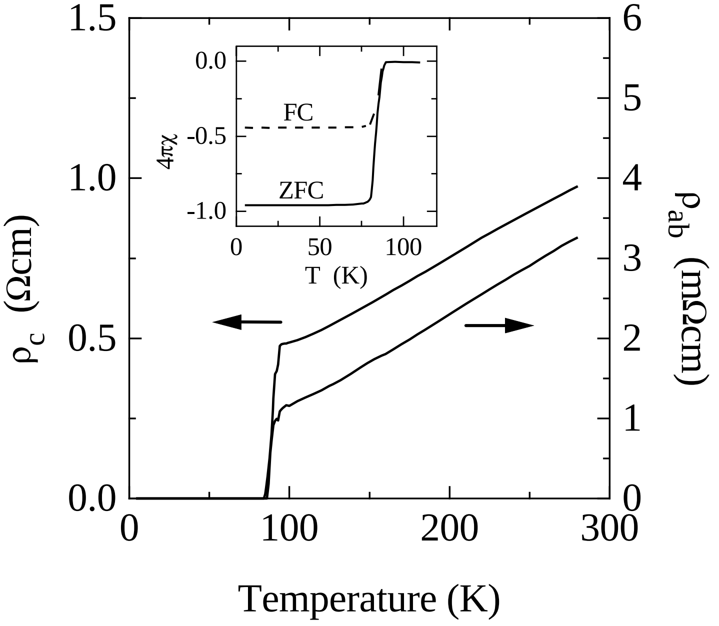

Figure 5.1: *DC resistivity versus temperature for $Tl_2Ba_2CuO_6$ (T_c = 85K). Inset DC magnetic susceptibility for field cooled(FC) and zero field cooled (ZFC)*

5.3.1 Calculation of n_{ab}

The half width of the LO phonons in the loss function Im(-1/ ϵ) is given by

$$\frac{1}{\tau} + \frac{4\pi\sigma_1^c S}{\epsilon_\infty(\epsilon_\infty + S)} \tag{5.11}$$

hence the width of these peaks can be used to determine σ_1^c, the real part of the electronic conductivity of the c-axis. After correcting for peak asymmetries of the pseudo loss function introduced through the phase shift η we obtain $\sigma_1^c = 0.7 \pm 0.3$ S/cm near 500 cm^{-1} at 4K. After having fitted the c-axis LO phonons, the ab-plane conductivity was fitted and so σ^{ab} (and n_{ab}) was determined. The value obtained was in reasonable agreement with Ref. [12]. In Fig. 5.2 there is no feature which resembles a collective mode in the superconducting state which disappears in the normal state. Measurements for the $Tl_2Ba_2CuO_6$ optimally doped sample were performed up to a frequency of 8000 cm^{-1} resulting in the same conclusion. The upper panel of Fig. 5.3 shows the reflectivity R_p for the $Tl_2Ba_2CuO_6$

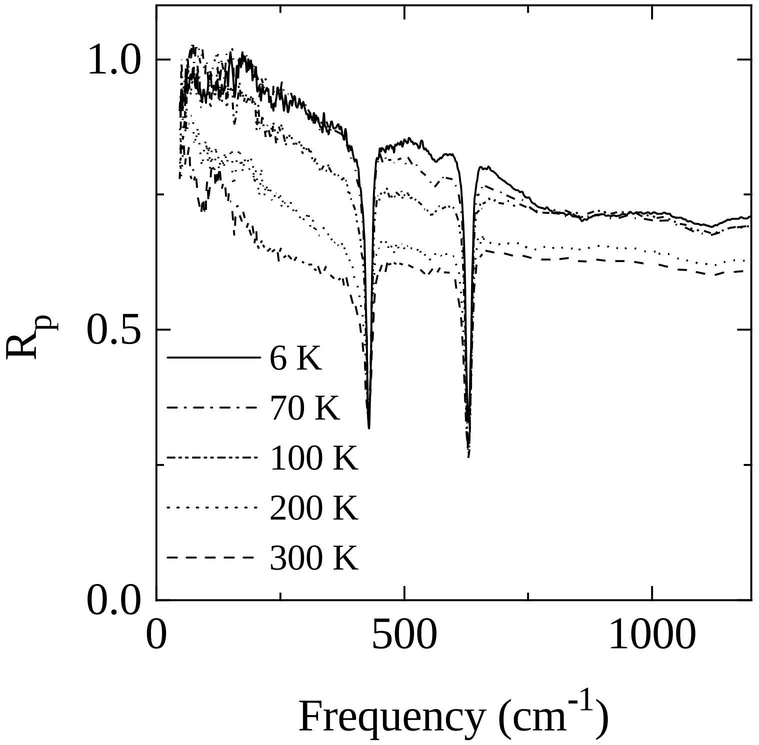

Figure 5.2: *Temperature dependent reflectivity* R_p *for* $Tl_2Ba_2CuO_6$ (T_c= *85K).*

film grown on a $SrTiO_3$ substrate. The film surface dimensions were much larger than the crystal mosaic, so the low frequency signal has a much improved signal to noise ratio. Again there is no evidence of a plasmon. The additional LO mode at 170 cm^{-1} belongs to the $SrTiO_3$ substrate.

In order to verify the technique a single crystal of $La_{1.85}Sr_{0.15}CuO_4$ (T_c = 32K) was measured and the resulting reflectivity R_p is shown in the lower panel of Fig. 5.3. The c-axis plasma edge is present at exactly the correct frequency of 50 cm^{-1} (reference chapter 4), the frequency decreases with increasing temperature and it is not present in the normal state. Figure 5.4, upper panel, shows R_p for the overdoped crystal of $Tl_2Ba_2CuO_{6+\delta}$ (T_c = 30K) at 4K and 300K. There is no feature resembling a plasmon. The reflectivity is flat and greater than 0.90, indicating that the material is becoming more like a metal when compared to the optimally doped sample. This is shown in Fig. 5.5 which shows both samples in the superconducting state (4K) and in the normal state i.e. just above T_c. The difference is quite stark, for the optimally doped crystal there is a clear decrease in reflectivity between 4K and 100K. In contrast for the overdoped crystal, there is no measureable difference between the superconducting and the normal state, this extends up to 6000 cm^{-1}. A similar trend was found for $La_{2-x}Sr_xCuO_4$ (chapter 3), although for the overdoped case there was still a measureable shift in spectral weight above and below T_c. The middle panel of Figure 5.4 shows R_p for the normal and superconducting state of $Nd_{1.85}Ce_{0.15}CuO_4$ (T_c = 23K) and the lower panel shows $Bi_2Sr_2CuO_6$, again there is no feature resembling a plasmon in either spectrum.

Using the technique of sphere resonance Noh *et al.* [13] found the plasma edge at 7.5 cm^{-1} for $Nd_{1.85}Ce_{0.15}CuO_4$. Noh*et al.* applied this technique to $La_{1.85}Sr_{.15}CuO_4$, the plasma edge was found at 50 cm^{-1} and for $La_{1.80}Sr_{0.20}CuO_4$ at 100 cm^{-1}, both of these values are correct(see chapter 4).

5.4 Discussion

Let us now compare the pseudo loss function obtained from measurements with that obtained from model calculations. All the plots shown in Figure 5.6 refer to the $Tl_2Ba_2CuO_6$, optimally doped crystal. Figure 5.6a shows the pseudo loss function based upon measurements at 4K and 100K. The spectrum is dominated by the two c-axis LO phonons at 429 and 631 cm^{-1}, with no sign of a plasmon. Fig. 5.6b shows the pseudo loss function based upon the ILT model and calculated using the values shown in Table 5.1. The Josephson screened plasma frequency ω_J is at 830 cm^{-1}. The LO phonon modes are shifted up in frequency due to the contribution from ϵ_1 for the plasmon. The LO modes are now superimposed upon a 'metallic' background which gives them a mixed character. Therefore the

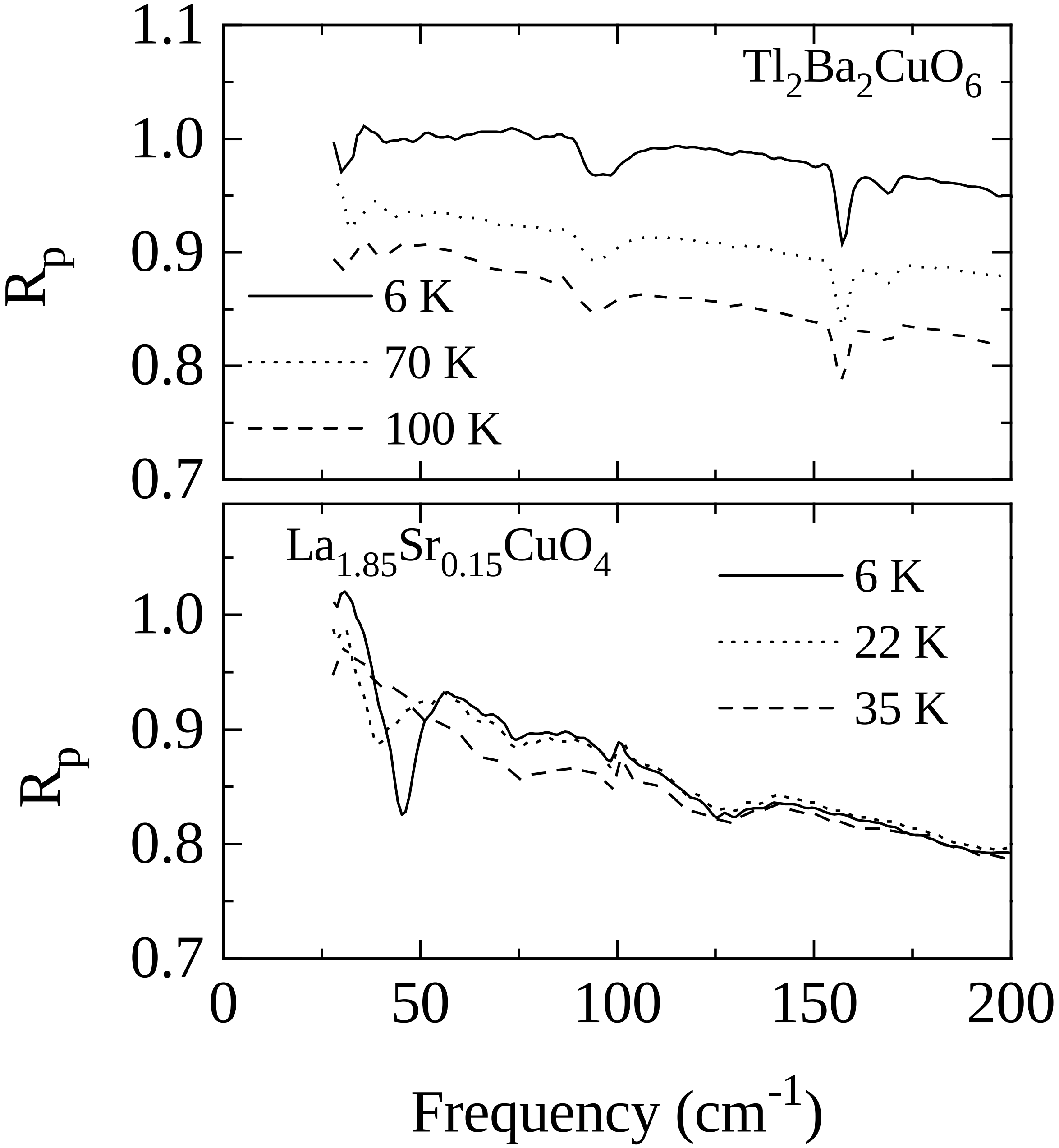

Figure 5.3: *Upper panel: Temperature dependent reflectivity* R_p *for the* $Tl_2Ba_2CuO_6$ *film. Lower panel:* R_p *for* $La_{1.85}Sr_{0.15}CuO_4$.

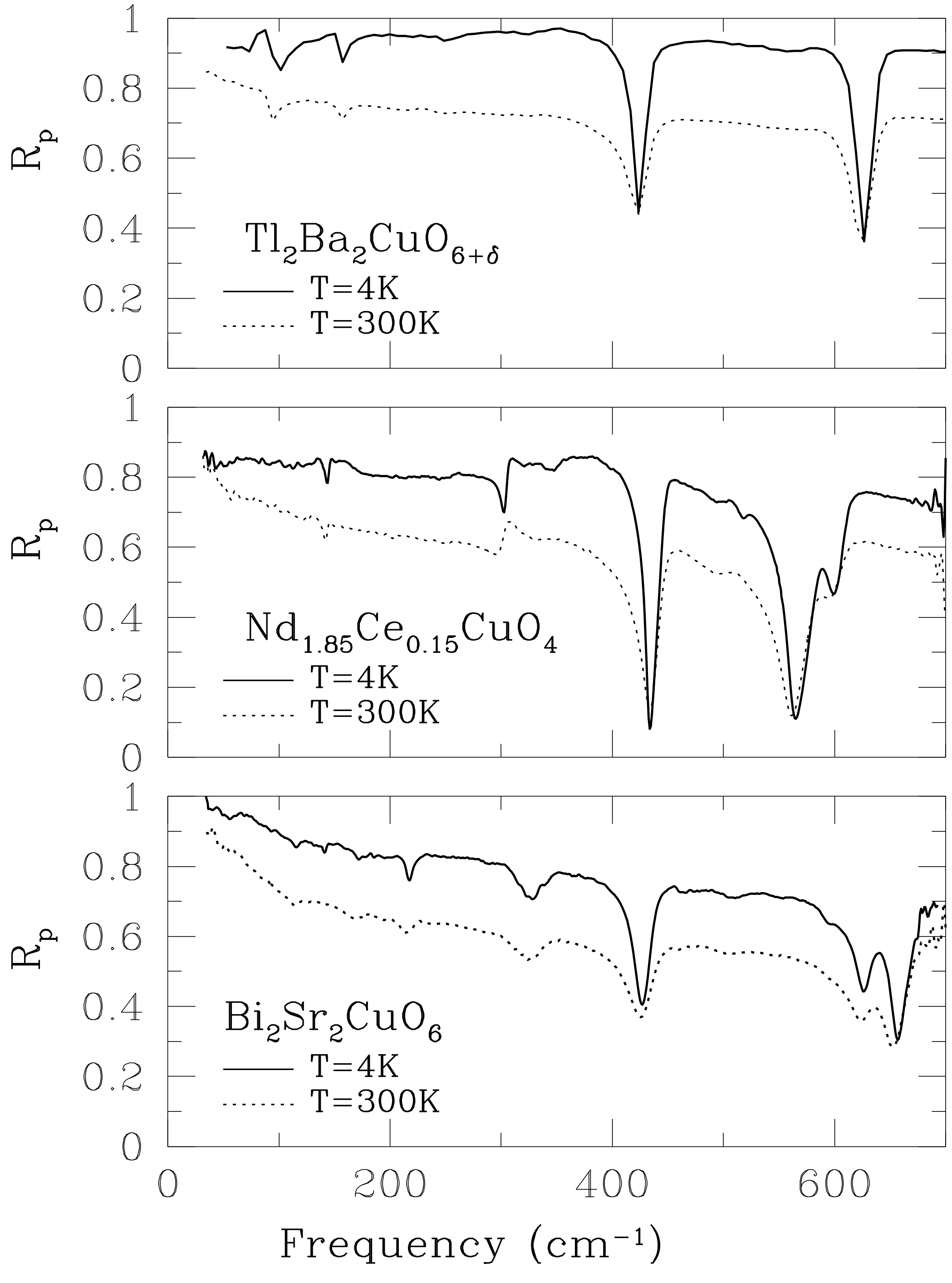

Figure 5.4: *R_p for the superconducting and normal state reflectivity. Upper panel: overdoped $Tl_2Ba_2CuO_{6+\delta}$. Middle panel: $Nd_{1.85}Ce_{0.15}CuO_4$. Lower panel: $Bi_2Sr_2CuO_6$.*

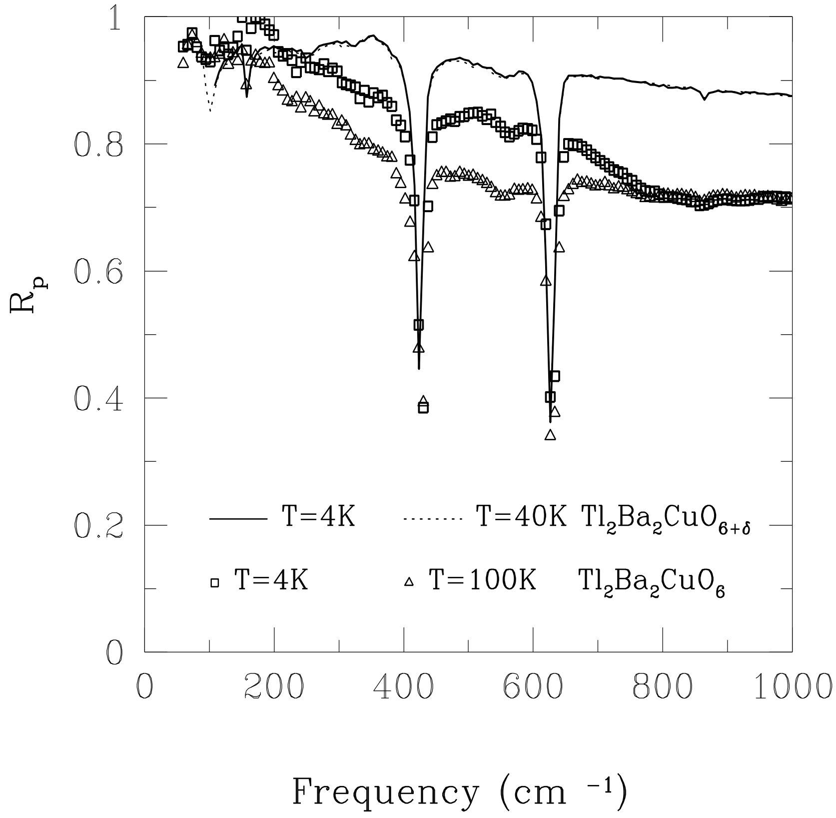

Figure 5.5: *Comparison of R_p for optimally and overdoped crystals of $Tl_2Ba_2CuO_{6+\delta}$.*

appearance of a plasmon would not only be detected from the R_p spectrum but also from the shift in the phonon frequencies.

Fig. 5.6c shows the pseudo loss function calculated using the Matthis-Bardeen dirty limit model and Eqn. 5.8. The screened plasma frequency appears at 50 cm^{-1} using $\epsilon_s = 22.5$. There is now no shift in the phonons as ω_J is below the lowest phonon frequency. Assuming a d-wave order parameter, the background c-axis electronic conductivity $\sigma_1^c(\omega)$ will increase. Such an increase is expected to have a smearing effect upon the plasmon. This is shown in Fig. 5.6d. If the background conductivity is increased to 3 $(\Omega\ \mathrm{cm})^{-1}$, the plasmon no longer has a distinct peak, but is much flatter and broader. Experimentally no Josephson plasmon was observed in $Tl_2Ba_2CuO_6$ (optimally doped) nor was there a shift

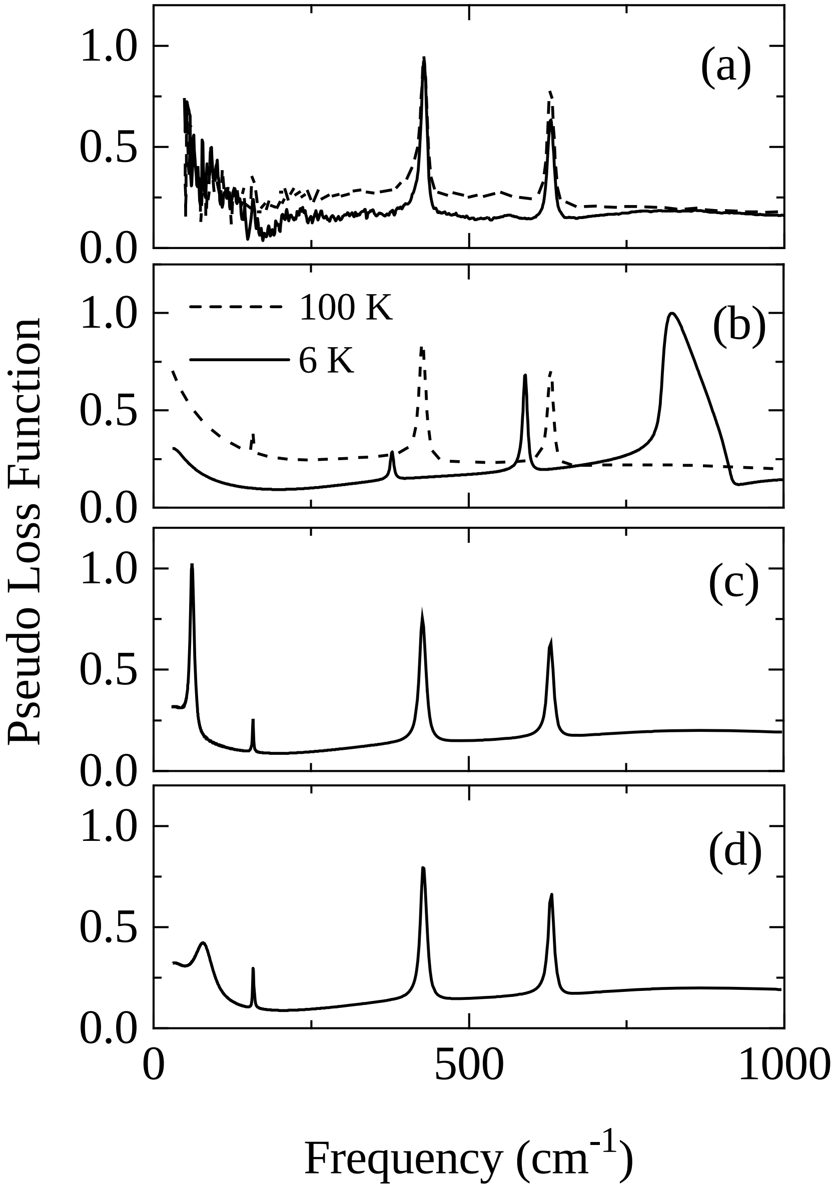

Figure 5.6: *All the figures show the pseudo loss function for* $Tl_2Ba_2CuO_6$ *for the following conditions. a : measurement. b: ILT model. c: using BCS model. d: as (c) but with* $\sigma^c = 3\ (\Omega cm)^{-1}$.

in the phonon spectrum in the superconducting state. One can therefore put an upper limit of 100 cm^{-1} on the unscreened value of ω_J, or in terms of the penetration depth, $\lambda_L > 15\mu$m.
The fraction of condensation energy contributed by the ILT mechanism $\eta = (\omega_J^{exp}/\omega_J^{ILT})^2 \approx 0.2$ for $La_{1.85}Sr_{0.15}CuO_4$ and $\eta \approx 0.005$ for $Tl_2Ba_2CuO_6$. These two compounds also differ considerably in their value of the c-axis conductivity just above T_c, $\sigma^c = 8$ $(\Omega$ cm$)^{-1}$ ($La_{1.85}Sr_{0.15}CuO_4$, T = 32K) and $\sigma^c < 2(\Omega$ cm$)^{-1}$ ($Tl_2Ba_2CuO_6$, T = 100K)
It is known that when a Josephson junction is placed in a magnetic field H, the critical current density J_c is reduced. In sufficiently strong fields, J_c is reduced to zero. As the Josephson plasma frequency is proportional to J_c , we would expect a shift in ω_J. However c-axis measurements of $La_{1.85}Sr_{0.15}CuO_4$ in fields up to 17.5T have shown no shift in ω_J [14]. This brings into question as to the type of coupling between the layers.
The aforementioned results were communicated to P. W. Anderson and S. Chakravarty. The explanation put forward by S. Chakravarty was that the initial prediction of ω_J did not take into account the highly anisotropic nature of the tunnelling matrix element and the gap. When this is taken into account the screened value of $\tilde{\omega}_J \approx 700$ cm^{-1} for $Tl_2Ba_2CuO_6$ and 80 cm^{-1} for $La_{1.85}Sr_{0.15}CuO_4$. The predicted values for ω_J are still not in agreement with the measurements for $Tl_2Ba_2CuO_6$ or $La_{1.85}Sr_{0.15}CuO_4$. Recent scanning SQUID (Superconducting Quantum Interference Device) measurements of $Tl_2Ba_2CuO_6$ by Kirtley *et al.* [15] give a penetration depth $\lambda_L = 15 \pm 1\mu$m. This corresponds to an unscreened value of the Josephson plasma frequency of 100 cm $^{-1}$. The screened value will be 50 cm^{-1} or lower and so confirms the measurements described in this chapter.

5.5 Conclusions

The c-axis LO modes of several single layer HTSC compounds were measured in the normal and superconducting state using the PARIS technique. Only for $La_{1.85}Sr_{0.15}CuO_4$ was a plasma edge measured in the superconducting state. From the results we are able to put an upper bound of 100 cm^{-1} on the vale of ω_J (unscreened) for $Tl_2Ba_2CuO_6$, $Bi_2Sr_2CuO_6$ and $Nd_{1.85}Ce_{0.15}CuO_4$. Recent SQUID measurements of $Tl_2Ba_2CuO_6$ put ω_J (unscreened) at 100 cm^{-1} and so confirm the measurements described in this chapter. Sphere resonance measurements of $Nd_{1.85}Ce_{0.15}CuO_4$ put the plasma edge at 7.5 cm^{-1} which confirms our measurements. The prediction of the ILT model is also incorrect for $La_{1.80}Sr_{0.20}CuO_4$ where T_c decreases but ω_J increases to 100 cm^{-1}, when compared to the optimal doped value(see chapter 4). The results indicate that the ILT model prediction of ω_J appears incorrect and requires further analysis.

References

[1] S. Chakravarty, A. Sudbo, P. W. Anderson, and S. Strong, Science **261**, 337 (1993).

[2] P. W. Anderson, Science **268**, 1154 (1995).

[3] D. van der Marel, J. Schützmann, H. Somal, and J. van der Eb, in *10th Anniversary HTS Workshop on Physics, Materials and Applications*, edited by B. Batlogg, C. W. Chu, W. K. Chu, D. U. Gubser, and K. A. Müller (World Scientific, Singapore, 1996), p. 000.

[4] A. J. Leggett, Science **274**, 587 (1996).

[5] J. Loram, private communication.

[6] M. Tinkham, *Introduction to Superconductivity* (McGraw-Hill, New York, 1996).

[7] R. Hazen, *Physical Properties of HTSC's, Volume 2 Ed. D. Ginsburg* (World Scientific, Singapore, 1990).

[8] H. M. Duan, Physica C **185**, 1283 (1990).

[9] T. Manako, Physica C **185**, 1327 (1990).

[10] A. D. Kulkarni, F. W. de Wette, J. U. Scroder, and W. Kress, Phys. Rev. B **41**, 6409 (1990).

[11] J. H. Kim, B. J. Feenstra, H. S. Somal, D. van der Marel, W. Y. Lee, A. M. Gerrits, and A. Wittlin, Phys. Rev. B **49**, 13065 (1994).

[12] A. V. Puchkov, T. Timusk, S. Doyle, and A. Herman, Phys. Rev. B **51**, 3312 (1995).

[13] T. W. Noh, S. G. Kaplan, and A. J. Sievers, Phys. Rev. B **41**, 307 (1990).

[14] A. Gerrits, Ph.D. thesis, University of Nijmegen, 1995.

[15] J. Kirtley, *The Gap.Symmetry and Fluctuations in HTSC's Eds. J. Bok, G. Deutscher and D. Pavuna* (NATO ASI series, Cargese 1-13 Sept, 1997 to be published., France, 1997).

Summary

Spectroscopic Probes

In order to investigate the properties of a material one must use an experimental probe, which will interact with the material. It is by examining the effect of this interaction that one is able to deduce or calculate a physical property of the material. There are two types of probe commonly used to investigate a material, transport and spectroscopic. A transport probe such as resistivity gives information about the density of electrons and the average time between electronic collisions as a function of temperature. A spectroscopic probe excites the material, and by varying the temperature one can investigate the superconducting and the normal state. Each different type of spectroscopic probe, probes a different aspect of the material, so that all of them together provide a complete picture. Some examples of spectroscopic probes are FIR (Far Infrared), Raman, Angle Resolved Photo Electron Spectroscopy (ARPES), Inelastic Neutron Scattering (INS), Muon Spin Resonance (μSR) and Nuclear Magnetic Resonance (NMR).

A spectroscopic probe can produce an electronic excitation, a collective excitation or a nuclear excitation. One can either measure the incoming and outcoming beam or the excitation produced. In Nuclear Magnetic Resonance (NMR) one excites the oxygen and copper nuclei, which before relaxing interact with the valence electrons. Inelastic Neutron Scattering (INS) provides information about the magnetic excitations such as magnons. In Inelastic Neutron Scattering a beam of monochromatic neutrons impinges upon the material and one measures the scattered beam. Having measured the energy and momentum (E,$\mathbf{k}$) of the incoming and outcoming neutrons one can calculate the dispersion relationship for the excitations. These may be phonons or magnons. In Photo Electron Spectroscopy (PES) the material is excited by a beam of photons but one measures the outcoming excited electrons. Here the exciting particle (photons) are not the same as the measured particle (electrons). Very often a model will be used to predict the outcome of an experiment. By comparing theory with experiment a better understanding of the material is obtained.

In Far Infrared Spectroscopy (FIR) we excite the material with photons (electromagnetic waves) of different energy and measure the rate of absorption. In this thesis we use reflectivity as a measure of the absorption. In order to obtain the absolute reflectivity, a perfectly reflecting mirror is used as a reference. Wherever the absolute reflectivity deviates from one, the material has absorbed or transmitted photons at this frequency. The conservation of energy holds so that R+T+A=1, where R is the absolute reflectivity, T is the transmisssion and A is the absorption.

The normal approach to determining whether a material is a metal, insulator or a semiconductor is to examine the frequency dependence of the reflectivity. A metal has a high reflectivity upto the plasma frequency, a semiconductor has a small and an insulator has a large energy gap with clear phonons.

For simplicity one often uses the independant particle approximation for the theoretical description of solids, even though electrons interact both directly (via Coulomb interaction) and indirectly (via electron-phonon interaction) with each other. This approach breaks down when the interaction energy of the particles is larger than the kinetic energy. This situation occurs in strongly correlated electron systems (SCES) and the HTSC's are considered to fall into this category. Single electron band calculations predict the parent compound La_2CuO_4 to be a metal whereas it is an insulator. Not only are the HTSC's strongly correlated, but also anisotropic which means their optical and transport properties depend upon which optical axis is being excited or along which axis the transport takes place. The cuprates are therefore complex materials for which the current solid state theory is inadequate.

Far infrared spectroscopy is the probe used in this thesis to investigate the HTSC's. The measurements were performed over a temperature range of 4K to 300K in a 113v Bruker Fourier Transform Infrared (FTIR) spectrometer. This spectrometer allows the material to be probed over a range of frequencies in one or two seconds. Repeating this measurement improves the noise statistics of the spectrum. For weak signals or small samples several hundred scans are normally performed. FIR spectroscopy measures the dressed electronic excitations (usually called quasiparticles), both in-phase (real part of σ) and out of phase (imaginary part of σ) values of the conductivity are obtained. The energy range of the spectrometer was 10 - 8000 cm^{-1}. The superconducting energy gap for all HTSC's falls well within this range. If one uses the BCS weak coupling relationship $2\Delta/kT_c$=3.5, then for $La_{1.85}Sr_{0.15}CuO_4$ ($T_c \approx$32K) the gap energy 2Δ is $\approx$ 82 cm^{-1} (10 meV). For HgBaCaO ($T_c \approx$ 132K) the gap is $\approx$ 340 cm^{-1} (41 meV). Even if we assume the case of extremely strong coupling eg. $2\Delta/kT_c$= 7, then the superconducting gap still falls within the measurement range of the spectrometer.

Symmetry of the Order Parameter

Near normal incidence, when the angle of incidence θ of the incoming beam is $\approx 5^\circ - 7^\circ$, FIR spectroscopy has a limitation when measuring the spectrum of materials which are highly reflecting i.e. R $\approx$ 1. The resulting optical conductivity then depends upon the noise level in the reflectivity measurements. Certainly

if small changes induced during the phase transition are of the order of the noise level they will be lost. Considering a BCS superconductor, if $\sigma_1(\omega) = 0$ then the reflectivity is one. However, if due to noise the measured value is R = 0.995, then the analysis will produce an artificially large value of $\sigma_1(\omega)$. The error of such a measurement would make the interpretation of σ_1 dubious. If the angle of incidence θ is now increased, the absorption and the sensitivity will be increased by $1/\cos\theta$. If θ is increased to 80° the sensitivity is increased by a factor of 6. Therefore small superconductivity induced changes are amplified by a factor of 6. This novel technique is the basis of this thesis and is referred to by the acronym PARIS (Polarized Angle Resolved Infrared Spectroscopy).
The shape of $\sigma_1(\omega)$ contains information about the symmetry of the order parameter. By modelling the conductivity based upon a s and a d-wave order parameter, one can compare the calculations with measurements and comment upon the symmetry of the order parameter for that particular material. PARIS measurements of $La_{1.85}Sr_{0.15}CuO_4$ (T_c = 32K) and for $La_{1.80}Sr_{0.20}CuO_4$ (T_c = 29K) show that no clear gap develops in the conductivity spectrum at 4K. This implies that the order parameter cannot be s-wave. Model calculations using a d-wave order parameter show a reasonable agreement. This does not affect the validity of the Ginzburg-Landau theory. It had long been asssumed that the effective number of charges continued to increase in going from the optimally doped case to the overdoped situation. But it was never understood why T_c decreased. High accuracy measurements of $La_{1.80}Sr_{0.20}CuO_4$ show in fact that the effective number of charge carriers decreases and so tracks T_c (see chapter 3).

The c Axis Electrodynamics

The HTSC's are characterized by a metallic ab-plane conductivity and a insulator like c-axis conductivity. Within a simple picture they may be viewed as two dimensional metallic sheets separated by insulating material. Near normal incidence FIR measurements of $La_{1.85}Sr_{0.15}CuO_4$ (optimally doped crystal) shows that the conductivity in the normal state is 8 $(\Omega\ \mathrm{cm})^{-1}$ at 40K which is below the Mott-Ioffe limit of 100 $(\Omega cm)^{-1}$ for a metal. There is no zero crossing of ϵ_1 which normally denotes the plasma frequency. Furthermore the scattering rate exceeds the theoretically calculated plasma frequency which is a very unusual situation. Below T_c a plasma edge appears at 50 cm $^{-1}$. This is unusual in that it's frequency is below the BCS gap value of 82 cm^{-1}, therefore it is a sub-gap collective excitation. Measurements on the overdoped crystal $La_{1.80}Sr_{0.20}CuO_4$ show a large increase in the conductivity σ_1 at 40K but the value is still below the Mott-Ioffe limit of 100 $(\Omega\mathrm{cm})^{-1}$. As the c-axis conductivity becomes more metallic, T_c decreases. For a change of 3K in the critical temperature, the plasma frequency doubles i.e. it becomes 100 cm^{-1} which is unexpected(see chapter 4).

Experimental Test of the Anderson Interlayer Tunnelling Model
P. W. Anderson and coworkers proposed that the frequency of the c-axis plasma edge was the Josephson plasma frequency ω_J. Furthermore that the critical temperature T_c was directly proportional to ω_J. This was a consequence of the Inter Layer Tunnelling (ILT) model. Due to the complicated coupling structure in a material with more than one copper-oxygen plane per unit cell, this model was applicable only to single layer compounds. The Josephson plasma frequency can be calculated, as it is based upon physical parameters. The calculated and measured value of ω_J for $La_{1.85}Sr_{0.15}CuO_4$ are in reasonable agreement with each other. The question remained as to whether it was valid for other single layer compounds. The concept had not been tested due to the lack of availability of crystals with sufficient c-axis dimensions to perform optical measurements. Crystals of $Tl_2Ba_2CuO_6$, $Nd_{1.85}Ce_{0.15}CuO_4$ and $Bi_2Sr_2CuO_6$ were available but only with c-axis dimensions of 50 - 100μm. However as the plasma edge is a longitudinal excitation it may be detected using the PARIS technique. The assumption was tested and verified on a crystal of $La_{1.85}Sr_{0.15}CuO_4$ where the plasma edge was correctly detected. Reflectivity measurements on $Tl_2Ba_2CuO_6$, $Nd_{1.85}Ce_{0.15}CuO_4$ and $Bi_2Sr_2CuO_6$ did not show a plasma edge near the predicted value. In fact no plasma edge was measured within the measurement range. The ILT model prediction for ω_J appears to be incorrect (see chapter 5).

Samenvatting

Spectroscopische Technieken

Als men de eigenschappen van een materiaal wil onderzoeken, is het noodzakelijk een probe te gebruiken die een interaktie heeft met het te onderzoeken materiaal. Door bestudering van het effect van de probe is het dan mogelijk de eigenschappen van het materiaal te bepalen of te berekenen. Twee soorten metingen worden gewoonlijk gebruikt om een materiaal te onderzoeken: transport en spectroscopie. Voorbeelden van transportmetingen zijn weerstandsmetingen en specifieke warmte, gebruikmakend van de temperatuur en de fase-overgang om de electronische eigenschappen te bepalen. Alle spectroscopische metingen exciteren het materiaal, en door de temperatuur te variëren kan men zowel de supergeleidende als de normale toestand onderzoeken. Iedere spectroscopie bekijkt een verschillend aspect van het materiaal, zodat ze tesamen een meer volledig beeld geven. Voorbeelden van spectroscopische metingen zijn FIR (ver infrarood spectroscopie), Raman, ARPES (hoekafhankelijke foto-elektron spectroscopie), INS (inelastische neutronenverstrooiing), μSR (muon spin resonantie), microgolf resonanties en NMR (nucleare magnetische resonantie).

Een spectroscopische probe maakt een elektronische excitatie, een collectieve excitatie of een nucleaire excitatie. Men kan de ingaande en uitgaande deeltjes meten ofwel de excitatie zelf. In NMR (nucleare magnetische resonantie) slaat de zuurstof en koperkernen aan, die een interaktie hebben met de valentieband voordat ze relaxeren. Inelastische neutronenverstrooiing geeft informatie over de magnetische excitaties zoals magnonen. In inelastische neutronenverstrooing (INS), wordt een bundel van monochromatische neutronen op het materiaal geschoten en meet men de verstrooide bundel. Als men de energie en de impuls (E,$\mathbf{k}$) van de ingaande en uitgaande neutronen meet, kan men de dispersie relatie van de excitaties berekenen. Deze excitaties kunnen zowel fononen als magnonen zijn. In Foto-Electron Spectroscopie (PES) wordt het materiaal geëxciteerd door een bundel fotonen en meet men de uitgaande elektronen. In dit geval zijn de ingaande deeltjes (fotonen) dus niet hetzelfde als de uitgaande deeltjes (elektronen). In de meeste gevallen zal een model worden gebruikt om het resultaat van het experiment te voorspellen door vergelijking van de theorie met het experiment, waardoor een betere kennis van het materiaal wordt verkregen.

In Ver Infrarood Spectroscopie (FIR) wordt het materiaal aangeslagen met fotonen (electromagnetische golven) van verschillende energieën en meet men de absorptie. Teneinde de absolute reflectiviteit te meten wordt een goud spiegel gebruikt als referentie. Wanneer de absolute reflectiviteit afwijkt van één, betekent dit dat het materiaal deze frequentie heeft geabsorbeerd of heeft doorgelaten. Behoud van energie impliceert dat R+T+A=1, met R = absolute reflectiviteit, T = transmissie en A = absorptie.

Men bepaalt of het materiaal een metaal, isolator of een halfgeleider is door de reflectiviteit te meten. Een metaal heeft een hoge reflectiviteit tot de plasma frequentie, een halfgeleider heeft een kleine en een isolator heeft een grote energiekloof met duidelijke waarneembare optische fononen in het spectrum.

Terwille van de eenvoud gebruikt men vaak de onafhankelijke deeljes benadering voor de theoretische beschrijving van vaste stoffen, ondanks het feit dat elektronen zowel rechtstreeks (via Coulomb wisseling) als indirekt (via elektron-phonon koppeling) met elkaar wisselwerken. Deze methode faalt voor een systeem waar de interactie energie (potentiële energie) groter is dan de kinetische energie. Deze situatie doet zich voor in sterk gecorreleerde elektron systemen (SCES) en de Hoge-Temperatuur Supergeleiders (HTSC's) kunnen beschouwd worden als behorende in deze categorie. Éendeeltjes bandenstructuurberekeningen voorspellen dat de moederverbinding La_2CuO_4 een metaal is, terwijl het een isolator is. Niet alleen zijn de HTSC's sterk gecorreleerd, ze zijn ook anisotroop, wat betekent dat de eigenschappen afhangen van de kristallografische orientatie. De HTSC's zijn daarom complexe materialen waarvoor de huidige theorie niet adekwaat is.

Ver Infrarood Spectroscopie (FIR) is de methode die in dit proefschrift is gebruikt om de HTSC's te onderzoeken. De metingen zijn verricht over een temperatuurgebied van 4K tot 300K in een 113v Bruker Fourier transformatie infrarood spectrometer. Deze spectrometer maakt het mogelijk het materiaal te meten over een groot frequentie breik in één of twee seconden. Door herhaling van de metingen kan de statistiek worden verbeterd. Voor zwakke signalen of kleine monsters zijn gewoonlijk enige honderden metingen uitgevoerd. FIR spectroscopie meet de aangeklede elektronische excitaties (gewoonlijk aangeduid met quasi-deeltjes), en zowel in fase (het reëele deel van σ) als uit fase (het imaginaire deel van σ) waarden van de geleidbaarheid worden verkregen. Het energiebereik van de spectrometer is 10 - 8000 cm^{-1}. De supergeleidende energiekloof voor alle HTSC's valt ruim binnen dit energiegebied. Als men de BCS zwakke koppelingslimietrelatie $2\Delta/kT_c$=3.5 gebruikt, dan is de energiekloof voor voor $La_{1.85}Sr_{0.15}CuO_4$ ($T_c \approx$32K) gelijk aan 2Δ ofwel $\approx$ 82 cm^{-1} (10 meV). Voor HgBaCaO ($T_c \approx$ 132K) is de energiekloof $\approx$ 340 cm^{-1} (41 meV). In het geval van extreem sterke koppeling, d.w.z. $2\Delta/kT_c$= 7, valt de supergeleidende energiekloof nog steeds binnen het bereik van de spectrometer.

De Symmetrie van de Ordeparameter

Bijna loodrechte inval (waarbij de hoek van inval θ gelijk is aan $\approx 5^\circ - 7^\circ$) FIR spectroscopy heeft een beperking als een materiaal sterk reflecterend is, d.w.z. als R $\approx$ 1. De resulterende optische geleidbaarheid hangt dan af van het ruisniveau in de reflectiviteitsmeting. Als kleine veranderingen (van de orde van grootte van de ruis) worden geinduceerd tijdens de fase-overgang, zullen ze niet zichtbaar zijn. Neem een BCS supergeleider met R=1, dan $\sigma_1(\omega) = 0$ maar als door de ruis de gemeten waarde van R gelijk is aan 0.995, dan wordt $\sigma_1(\omega)$ groot. De foutenmarge van deze meting, maakt de interpretatie van de metingen moeilijk en dubieus. Als de hoek van inval θ wordt vergroot, zullen de absorptie en dus de gevoeligheid worden vergroot met $1/\cos\theta$. Dus als θ wordt vergroot tot 80°, wordt de gevoeligheid vergroot met een factor van 6. Deze nieuwe techniek is de basis van dit proefschrift en zal worden aangeduid met het acroniem PARIS (Polarized Angle Resolved Infrared Spectroscopy).

De vorm van $\sigma_1(\omega)$ bevat informatie over de symmetrie van de ordeparameter. Door het modelleren van de geleidbaarheid gebaseerd op een s en d golf ordeparameter, kan men de berekeningen vergelijken met de metingen, en informatie verkrijgen over de symmetrie van de ordeparameter voor het bekeken materiaal. PARIS metingen aan $La_{1.85}Sr_{0.15}CuO_4$ (optimaal gedoteerd, T_c = 32K) en voor $La_{1.80}Sr_{0.20}CuO_4$ (overgedoteerd T_c = 29K) laten zien dat zich geen duidelijke energiekloof ontwikkelt in het geleidbaarheidsspectrum bij 4K. Dit betekent dat de ordeparameter niet beschreven kan worden met een s golf. Modelberekeningen gebruikmakend van een d golf ordeparameter geven een redelijke overeenkomst.

Dit heeft geen consequenties voor de toepassing van de Ginzburg-Landau theorie. Normaal gesproken werd aangenomen dat het effectieve aantal van ladingen blijft toenemen als men van de optimaal gedoteerde situatie naar de overgedoteerde situatie gaat, waarbij nooit echt werd begrepen waarom T_c afneemt. Hoge precisie metingen aan $La_{1.80}Sr_{0.20}CuO_4$ laten zien dat het effectieve aantal van ladingsdragers afneemt en evenredig is met T_c (zie hoofdstuk 3) .

De c-as electrodynamica

De HTSC's worden gekarakteriseerd door een metallisch ab vlak en zijn isolerend in de c richting. Binnen een eenvoudig model kan dit worden gezien als tweedimensionale metallische lagen gescheiden door een isolerend materiaal. Bijna loodrecht invallende FIR metingen aan $La_{1.85}Sr_{0.15}CuO_4$ (optimaal gedoteerd) laten zien dat de geleidbaarheid in de normale toestand gelijk is aan 10 $(\Omega\text{cm})^{-1}$ bij 40K, wat lager is dan de Mott-Ioffe limiet van 100 $(\Omega\text{cm})^{-1}$ voor een metaal. Er is geen nuldoorgang ϵ_1 die normaal gesproken de plasmafrequentie aangeeft. Bovendien is de gevonden verstrooiings- intensiteit hoger dan de theoretische plasma-frequentie, wat een zeer ongebruikelijke situatie is. Onder T_C wordt een plasma-grens zichtbaar bij 50 cm $^{-1}$. Dit is ongebruikelijk omdat deze waarde lager is dan de BCS energiekloof van 82 cm^{-1}, c.q. het is een 'sub-gap' collectieve excitatie. Metingen aan het overgedoteerde kristal $La_{1.80}Sr_{0.20}CuO_4$ laten een sterke toename zien in de geleidbaarheid σ_1 bij 40K, maar de waarde is nog steeds onder de Mott-Ioffe limiet van 100 $(\Omega\,\mathrm{cm})^{-1}$. Omdat de c-as geleidbaarheid meer metaalachtig wordt, neemt T_c af. Voor en reductie van 3K in T_c, is er een verdubbeling in de plasma-grens tot 100 cm^{-1}, wat onverwacht is(zie hoofdstuk 4) .

Experimentele Test van het Anderson Tussenlaag Tunnelling Model

P. W. Anderson et al. hebben voorgesteld dat de frequentie van de c-as plasmagrens gelijk is aan de Josephson plasma frequentie ω_J. Bovendien zou de kritische temperatuur T_c direct evenredig zijn met ω_J. Dit wordt aangeduurd als het Inter Layer Tunnelling (ILT) model. Door de gecompliceerde koppelingsstruktuur in een materiaal met meer dan één koper-zuurstof laag per eenheidscel, is dit model alleen toepasbaar op éénlaags verbindingen. De Josephson plasma frequentie kan worden berekend. De met elkaar van de berekende ω_J en de metingen voor $La_{1.85}Sr_{0.15}CuO_4$ zijn redelijk in overeenkomst. De vraag blijft of dit model ook geldig is voor andere éénlaags verbindingen. Het concept is niet getest door gebrek aan kristallen met een voldoende c-as dimensie om optische metingen te doen. $Tl_2Ba_2CuO_6$ en $Nd_{1.85}Ce_{0.15}CuO_4$ kristallen waren beschikbaar maar alleen met de c-as dimensies van 50 - 100 μm. Maar omdat de plasma-grens een longitudinale excitatie is, kan het worden gedetecteerd met gebruikmaking van de PARIS techniek. De aanname is getest en geverifieerd met een $La_{1.85}Sr_{0.15}CuO_4$ kristal, waarvan de plasma-frequentie correct kon worden gedetecteerd. Reflectiviteitsmetingen aan $Tl_2Ba_2CuO_6$ en $Nd_{1.85}Ce_{0.15}CuO_4$ gaven geen plasma-frequentie te zien bij de voorspelde waarde binnen de meetgrenzen van de spectrometer. De voorspelde waarde voor ω_J van de ILT model blijkt niet te kloppen met het experiment (zie hoofdstuk 5).

Acknowledgements

I am indebted to Dick van der Marel for his help and guidance in completing this thesis. Unlike many people he did not upon asking my age say ”good luck and goodbye”; it is unfortunate that age discrimination is so widespread. Special thanks go to Cor Bos who helped get the various pieces of equipment running and who was always available to solve problems. During the course of the last five years I have benefitted from discussions with Robert Eder, Frank de Groot, Ronald Hesper and Jurgen Schützmann. Thanks go to Jeroen van der Eb for using his *in-situ* evaporator which originally was designed for cerium but did just as good a job with gold. A ’thank you’ is extended to the reading commission members Profs. L. F. Feiner, T. T. M. Palstra and G. A. Sawatzky for their comments.

List of Publications

J. H. Kim, B. J. Feenstra, H. S. Somal, D. van der Marel, W. Y. Lee, A. M. Gerrits and A. Wittlin
c Axis Infrared Response of $Tl_2Ba_2CuO_6$ Studied by Oblique -Incidence Polarized Reflectivity Measurements
Phy Rev B 49, 13065(1994)

D. van der Marel, J. H. Kim, H. S. Somal, B. J. Feenstra, A. Wittlin, V. H. M. Duijn, A. A. Menovsky and W. Y. Lee
Damping Mechanism of the Strongly Renormalized c Axis Plasma Frequency in HTSC's
Physica C, 235-240, 1145 (1994)

J. H. Kim, B. J. Feenstra, H. S. Somal, D. van der Marel, A. Wittlin, V. H. M. Duijn, A. A. Menovsky and W. Y. Lee,
Infrared Anisotropy and Plasmon's in HTSC's
Synthetic Metals 71, 1577 (1995)

J. H. Kim, H. S. Somal, M. T. Czyzyk, D. van der Marel, A. Wittlin, A. M. Gerrits, V. H. M. Duijn, N. T. Hien and A. A. Menovsky
Strong Damping of the c Axis Plasmon in HTSC's
Physica C, 247, 297 (1995)

H. S. Somal, B. J. Feenstra, J. Schützmann, J. H. Kim, Z. H. Barber, V. H. M. Duijn, N. T. Hien, A. A. Menovsky, M. Palumbo and D. van der Marel.
Grazing Incidence Reflectivity of $La_{1.85}Sr_{0.15}CuO_4$ and NbN
Phys Rev Lett 76, 1525(1996)

D. van der Marel, J. Schützmann, H. S. Somal, J. van der Eb
Electrodynamical Properties of HTSC's Studied by Polarized Angle Resolved Infrared Spectroscopy
Proceedings of 10th Anniversary of the Discovery of HTSC's, Houston,USA March 1996.

J. Schützmann, H. S. Somal, A. A. Tvetkov, D. van der Marel, G. Koops,

N. Koleshnikov, Z. F. Ren, J. H. Wang, E Brück and A. A. Menovsky
c Axis Excitations in HTSC's Detected by Grazing Incidence Reflectivity Measurements
Proceedings of Low Temperature Physics LT21, Prague, August 1996.

J. Schützmann, H. S. Somal, A. A. Tvetkov, D. van der Marel, G. Koops, N .Koleshnikov, Z. F. Ren, J. H. Wang, E. Brück and A. A. Menovsky.
Experimental Test of Interlayer Pairing Models of HTSC's Using Grazing Incidence Infrared Reflectometry
Phy. Rev. B 55, 11118 (1997).

B. P. Gorshunov, A. V. Pronin, A. A. Volkov, H. S. Somal, D. Van der Marel, B. J. Feenstra, Y. Jaccard and J-P. Locquet
Dynamical Conductivity of an MBE Grown $La_{1.85}Sr_{0.15}CuO_4$ thin film at Frequencies from 5 to 36 cm^{-1}
Accepted for publication in Physica B